BOSTON UNIVERSITY
GRADUATE SCHOOL OF ARTS AND SCIENCES

Dissertation

LIQUID-LIQUID PHASE TRANSITIONS AND WATER-LIKE ANOMALIES IN LIQUIDS

by

ERIK LASCARIS

M.A., Twente University, 2006

Submitted in partial fulfillment of the
requirements for the degree of
Doctor of Philosophy
2014

Approved by

First Reader

H. Eugene Stanley, Ph.D.
University Professor and Professor of Physics

Second Reader

William J. Skocpol, Ph.D.
Professor of Physics Emeritus

Third Reader

Karl F. Ludwig, Ph.D.
Professor of Physics

In memory of my friends Alvaro and Kelly, and my father René.

ACKNOWLEDGMENTS

Firstmost, I must thank my advisor Professor Gene Stanley, for without him this work would have never been possible. Apart from providing me with projects to work on and to learn from, he has created a unique environment that allows a person to grow from a student into a scientist.

I am also grateful to Gene for introducing me to Sergey Buldyrev, from who I have probably learned the most over the last few years. I like to thank Sergey for the many pleasant and insightful discussions I have had with him, and I am looking forward to having many more of these in the future. In the same breath I wish to thank Austen Angell, who has helped me tremendously during the final part of my PhD. Working together with him has been an honor, a pleasure, and an inspirational experience. Austen is a role model for me, and I hope that my future in science will one day be comparable to his.

Although I consider things like quantum mechanics and multivariate calculus as fun and exciting, duties such as filling in registration forms and other administrative tasks have often felt nearly impossible to me. Fortunately I could always rely on my graduate advisor and guardian angel, Mirtha Cabello, for which I am extremely grateful. She has always ensured that I was properly registered, that I received all my payments on time, and that I did not get into any trouble.

While working on my research I have had the unique opportunity to learn more about the Linux operating system, which is a incredibly valuable skill for someone in the field of computational physics and chemistry. For this I thank Guoan Hu who has been like a teacher to me.

I also like to thank both Bob Tomposki and Jerry Morrow for making my life easier by assisting me with the scheduling of meetings, the ordering of equipment,

bringing cookies, checking my spelling, and helping me with my grammar.

A special thanks to my girlfriend Karol Guzman, for her loving support and for giving me the time and space I needed to finish my dissertation and do the work this manuscript is based on. I am very, very happy with her love and patience, and consider myself a very lucky guy for having her in my life.

And last but not least, I thank all my friends here at Boston University that have helped me through the years, in particular Plamen Ichanov, Elena Strekalova, Jiayuan Luo, Dario Corradini, João Ricardo Santos, Will Morrison, Henio Aragão, Carlos Calero, Ronny Bartsch, Nima Dehmamy, Tiago Souza, and Joel Tenenbaum.

LIQUID-LIQUID PHASE TRANSITIONS
AND WATER-LIKE ANOMALIES IN LIQUIDS

ERIK LASCARIS

Boston University Graduate School of Arts and Sciences, 2014

Major Professor: H. Eugene Stanley, University Professor and Professor of Physics

ABSTRACT

In this thesis we employ computer simulations and statistical physics to understand the origin of liquid-liquid phase transitions and their relationship with anomalies typical of liquid water.

Compared with other liquids, water has many anomalies. For example the density anomaly: when water is cooled below 4 °C the density decreases rather than increases. This and other anomalies have also been found to occur in a few other one-component liquids, sometimes in conjunction with the existence of a liquid-liquid phase transition (LLPT) between a low-density liquid (LDL) and a high-density liquid (HDL). Using simple models we explain how these anomalies arise from the presence of two competing length scales. As a specific example we investigate the cut ramp potential, where we show the importance of "competition" in this context, and how one length scale can sometimes be zero. When there is a clear energetic preference for either LDL or HDL for all pressures and temperatures, then there is insufficient competition between the two liquid structures and no anomalies occur.

From the simple models it also follows that anomalies can occur without the presence of a LLPT and vice versa. It remains therefore unclear if water has a LLPT that ends in a liquid-liquid critical point (LLCP), a hypothesis that was first proposed based on simulations of the ST2 water model. We confirm the existence

of a LLCP in this model using finite size scaling and the Challa-Landau-Binder parameter, and show that the LLPT is not a liquid-crystal transition, as has recently been suggested.

Previous research has indicated the possible existence of a LLCP in liquid silica. We perform a detailed analysis of two different silica models (WAC and BKS) at temperatures much lower than was previously simulated. Within the accessible temperature range we find no LLCP in either model, although in the case of WAC potential it is closely approached. We compare our results with those obtained for other tetrahedral liquids and conclude that insufficient "stiffness" in the Si-O-Si bond angle might be responsible for the absence of a LLCP.

TABLE OF CONTENTS

LIST OF TABLES

LIST OF FIGURES

LIST OF ABBREVIATIONS

HDA . . . . . High-Density Amorphous ice

HDL . . . . . High-Density Liquid

LDA . . . . . Low-Density Amorphous ice

LDL . . . . . Low-Density Liquid

LLCP . . . . . Liquid-Liquid Critical Point

LLPT . . . . . Liquid-Liquid Phase Transition

RDF . . . . . Radial Distribution Function

TMD . . . . . Temperature of Maximum Density

TmD . . . . . Temperature of minimum Density

CHAPTER 1: Introduction

> *Some people say, "How can you live without knowing?" I do not know what they mean. I always live without knowing. That is easy. How you get to know is what I want to know.*
>
> – Richard. P. Feynman, in *The Meaning of It All*

1.1 The liquid phase and critical points

Of the three classical states of matter, the liquid state seems to be the most challenging phase to characterize. It lacks the long-range order of crystals, but neither does it have the complete disorder of a gas. Being the state between gas and solid, it should come as no surprise that the physics of liquids is a field rich in interesting phenomena.

At first glance, it might be obvious what constitutes as a liquid, but this is not always trivial. Consider, for example, the standard phase diagram in Fig. 1.1 with the three phases: solid, liquid, and vapor (gas). Between the solid and liquid there is the melting line, and between the solid and vapor the sublimation line. The liquid and gas phases are separated by the liquid-gas phase transition line, which usually ends in a critical point. Near the critical point all differences between the gas and liquid disappear, and above the critical temperature and critical pressure there is no difference at all between the two phases. In this thesis, however, we shall only consider temperatures far below the liquid-gas critical point, so it will always be clear whether the fluid is a liquid or a gas.

An obvious question to ask here, is whether there exists such a thing as a crystal-liquid critical point. The answer to that question is, in fact, negative. As we travel

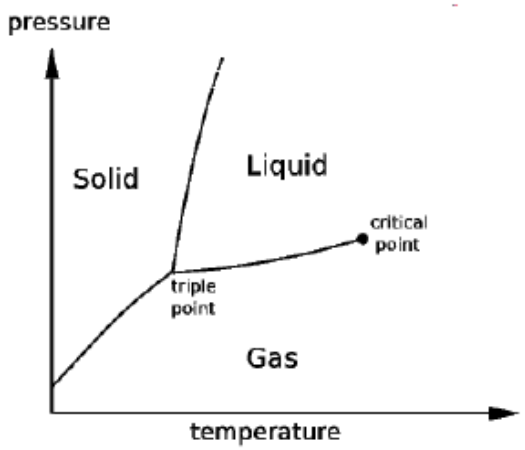

Figure 1.1: Standard phase diagram with the three stable phases as a function of temperature and pressure. Near the critical point the difference between liquid and gas (vapor) disappears.

along a phase transition line, approaching a critical point, we find that the distinction between the two phases slowly disappears. A crystal is defined as a solid that displays a long-range order, which can be represented by a unit-cell that is repeated in all directions, and which is therefore highly symmetric. The liquid, however, has no such long-range symmetry, and therefore the phase boundary between crystal and liquid will always be discontinuous – one cannot smoothly transform a crystal into a liquid, and so there is no critical point.

Note that it is still possible to have a solid-liquid critical point if the solid has no long-range symmetry. These solids are not crystals, but are called *amorphous solids*. One of the most famous examples of an amorphous solid is silica (SiO_2), which is ordinary window glass. Possibly for this reason amorphous solids are also known as *glasses*, and we shall use these two names interchangeably.

1.1.1 Amorphous solids

An amorphous solid can be considered to be a liquid whose molecules have practically stopped moving; its self-diffusion is so low, that the material behaves as a solid. In most cases the self-diffusion D is related to the viscosity η via the Stokes-Einstein equation

$$D = \frac{k_B T}{6\pi\eta r} \tag{1.1}$$

where r is the effective radius of the particle. From this relation it is clear that a glass is like a liquid with an enormously large viscosity, and that a liquid becomes more glassy when the temperature is lowered. In fact, one definition of what constitutes as a glass (as opposed to a normal liquid) is that a glass has a shear viscosity of $\eta \geq \eta_g \equiv 10^{12}$ Pa·s (10^{13} Poise) [46]. The glass transition temperature T_g is then the temperature at which the viscosity has reached η_g. To put this number into perspective, we have listed several familiar liquids in Table 1.1 and sorted them according to their viscosity.

To create an amorphous solid in experiment one often starts with a liquid and then rapidly cools it down[1]. As is indicated in Fig. 1.1, the solid state melts into the liquid when it is heated to above the melting temperature. On the other hand, for the liquid to crystallize, it needs a cluster of atoms that forms a tiny crystal from which the rest of the crystal can grow. Without such a *crystal nucleus* the liquid remains a fluid, even at low temperatures. Small disturbances (such as a speck of dust) can act as a nucleus, but if done carefully it is possible to cool the liquid down to below the melting temperature and obtain a metastable state known as a

[1]There are alternative methods for creating glasses, such as spraying vapor onto a very cold plate, applying large pressures onto a crystal, or exposing a crystal to nuclear radiation [11]

Fluid	Viscosity in 10^{-3} Pa·s	Reference
Helium (liquid) at 4 K	0.003319	Ref. [69]
Air (gas) at 300 K, 1 bar	0.0185	Ref. [69]
Liquid silica at 1800 K, 1 bar	0.541	Ref. [69]
Water	1.002	Ref. [69]
Mercury at 25 °C	1.526	Ref. [69]
Blood at 37 °C	4	Ref. [204]
60 wt% *D*-glucose solution in water	37.445	Ref. [69]
Vegetable oil	70	Ref. [204]
Motor oil SAE-30	200	Ref. [204]
Glycerol	1,460	Ref. [69]
Maple syrup	2,000	Ref. [204]
Honey	10,000	Ref. [204]
Ketchup	50,000	Ref. [204]
Peanut butter	200,000	Ref. [204]
Lard	1,000,000	Ref. [204]
Tar	30,000,000	Ref. [204]

Table 1.1: Several fluids and their viscosity (all at 20 °C and 1 bar, unless noted otherwise). Values from [204] are approximate values.

supercooled liquid.

As the supercooled liquid is cooled to lower and lower temperatures, the molecules move slower and slower. During this process, several things can happen, depending on the type of liquid in question. In some cases the liquid displays *homogeneous nucleation* and the molecules spontaneously crystallize no matter how carefully you cool the liquid. In other cases an amorphous solid is produced, and the molecules move too slow to be able to form the crystal (within the time window of the experiment).

How fast the transition from liquid to glass is, depends on the type of liquid (see Fig. 1.2). For the so-called "strong" liquids (such as SiO_2) the viscosity increase is approximately Arrhenius, i.e., it can be described well by $\eta(T) = A \exp(E/k_B T)$ where A and E are independent of temperature [46]. On the other hand, the increase in viscosity (as a function of inverse temperature) is much steeper for the "fragile"

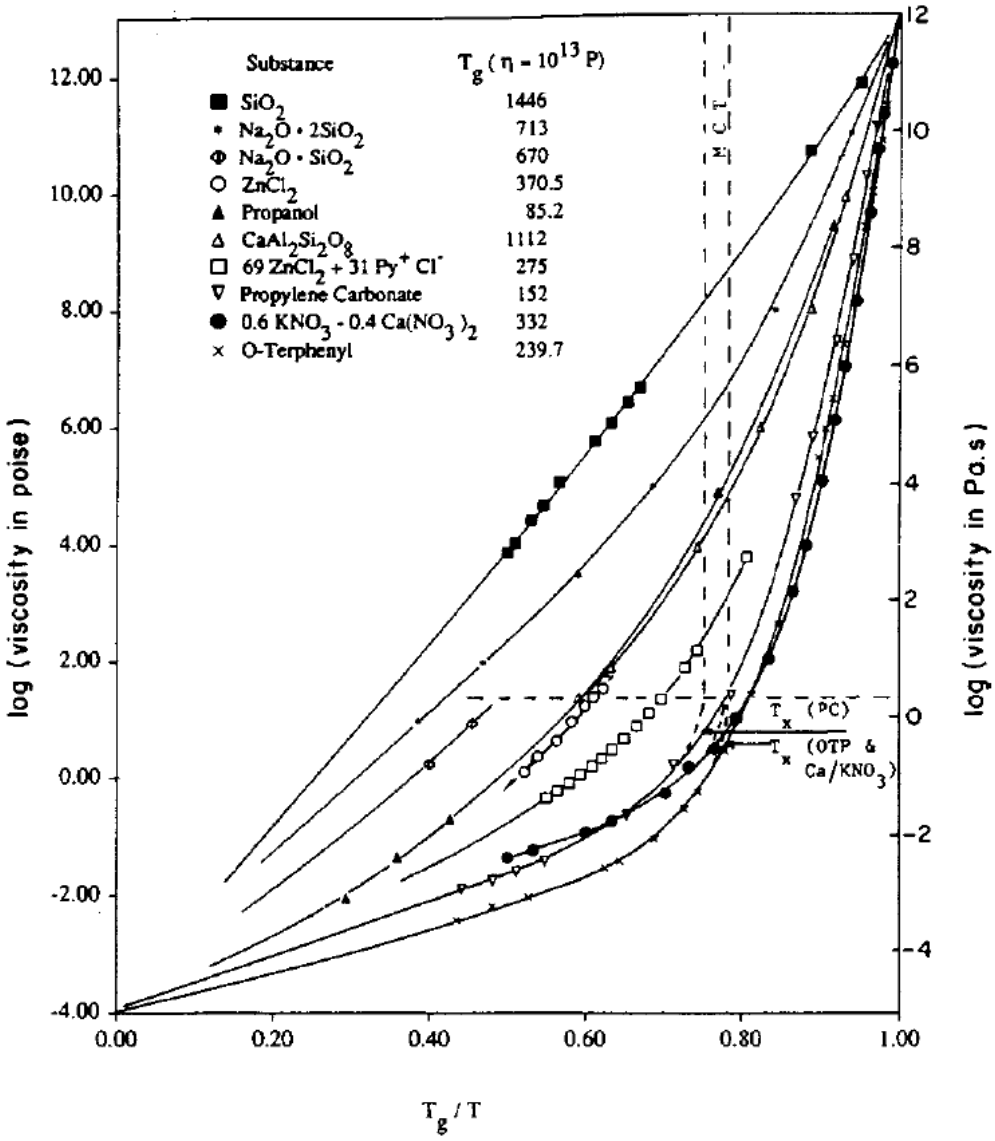

Figure 1.2: The "fragility" of several glass-forming liquids [11]. The viscosity of these liquids rapidly increases upon lowering the temperature, until at $T = T_g$ they reach the glass transition at $\eta = \eta_g = 10^{12}$ Pa.s, and are considered an amorphous solid. The horizontal axis indicates the inverse temperature T_g/T, normalized by the glass transition temperature T_g, which is different for each liquid. In this so-called Angell plot, liquids are classified as "strong" liquids if they lie near the straight line of slope $\sim$16 (such as SiO_2), which means they approach the glass transition relatively slowly, and follow the Arrhenius law $\eta(T) = A \exp(E/k_B T)$ (see text). Liquids with $\eta(T)$ far away from this straight line are called "fragile" liquids.

liquids (such as toluene, ortho-terphenyl, and salol [165]). The difference between the two types of liquids is particularly clear on an Angell plot (such as Fig. 1.2), where the strong liquids lie close to a straight line while the fragile liquids display a large curvature.

The field of glass-formers is a very active one, and there are many questions that are still waiting for a good answer [7, 11]. In fact, the nature of the glass transition is considered to be one of the major unsolved problems in physics and chemistry today [5].

1.1.2 Liquid-liquid phase transitions

Apart from a liquid-gas critical point or a liquid-glass critical point, it is also theoretically possible [73, 193, 86] to have a liquid-liquid critical point (LLCP). Experimentally, however, it is very difficult to measure such a critical point, and the first liquid-liquid phase transitions (LLPTs) have only been discovered quite recently.

One can easily imagine a phase separation within a binary mixture of liquids (such as water and oil), but it might be hard to see how a one-component liquid can separate into two distinct liquids. The important thing we need to realize here, is that liquids have structure.

Unlike the case of an ideal gas, where the particles have no interaction with each other, in a liquid the interaction is such that particles typically like to be at a certain distance of each other. The result is that they roughly order themselves in spherical "shells" around one another, as in Fig. 1.3a. The average number of nearest neighbors (those within the first shell) is known as the *coordination number* and depends on the liquid. For simple liquids, such as liquid argon for example, the coordination number is roughly 12. The molecules in water, on the other hand, form a tetrahedral network of hydrogen bonds which means the coordination number is

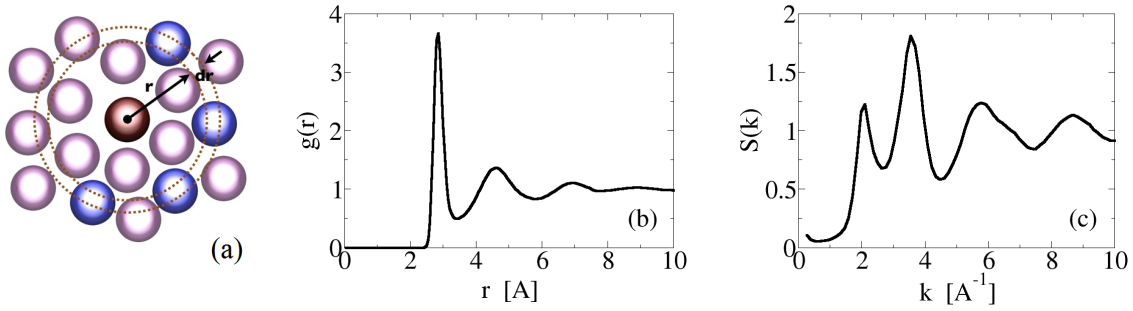

Figure 1.3: The structure of liquids. (a) Liquids are not completely disordered, but show short-range order and form "shells" around one another. This is particularly clear from the radial distribution function $g(r)$ that represents the probability of finding a neighbor at a distance between r and $r + dr$. (b) Radial distribution function $g(r)$ of the oxygen atoms in ST2 water at $P = 210$ MPa and $T = 245$ K. The location of the first peak indicates that the nearest oxygen neighbor of each oxygen atom is at an average distance of about 3 Å. (c) The structure factor $S(k)$ for the same system as in panel (b).

about 4.

The most common method to quantify the structure of a liquid, is by calculating the *radial distribution function* (RDF), as in Fig. 1.3b. The radial distribution function $g(r)$ is defined as the average particle density at a distance r from any given particle, normalized to that of an ideal gas (i.e., such that $g(\infty) = 1$). Hence, for an ideal gas we simply have $g(r) = 1$ for all r. The RDF of a perfect crystal consists of a set of sharp peaks, because all particles are at discrete distances from each other. In experiments such as neutron scattering one cannot measure $g(r)$ directly, but instead the *structure factor* $S(k)$ is obtained, with k the wave number (see Fig. 1.3c). The structure factor is related to the RDF via the Fourier transform, and one can therefore easily convert $S(k)$ to $g(r)$ and vice versa. For isotropic liquids,

the relation is given by

$$\begin{aligned} S(k) &= 1 + \rho \int [g(r) - 1] \exp\left(-i\mathbf{k} \cdot \mathbf{r}\right) \, \mathrm{d}^3\mathbf{r} \\ &= 1 + 4\pi\rho \int_0^\infty [g(r) - 1] \, \frac{\sin(kr)}{kr} r^2 \, \mathrm{d}r \end{aligned} \tag{1.2}$$

with $\rho = N/V$ the number density.

Because liquids have a distinct and quantifiable structure, it is in some cases possible to have a phase separation between two liquids of different structure that are made up of the same molecule. This can then lead to having a liquid-liquid phase transition between those two liquids. Liquid phosphorus probably provides the best example; it has a LLPT that was theoretically predicted [75] and subsequently observed in experiment [94, 92, 93]. In the case of phosphorus the LLPT is associated with the transformation from a molecular liquid of P_4 molecules into a polymeric liquid consisting of P atoms attached into chains and rings of various sizes (see Fig. 1.4).

There is now a growing body of evidence, both experimental and computational, that LLPTs may exist at high temperatures and pressures in group-IV elements like silicon [166, 134, 123, 124] and germanium [153, 132, 19, 131], in certain molecular compounds such as silica (SiO_2) [125, 150, 159], in ionic salts such as BeF_2 [71], and also in molten Al_2O_3-Y_2O_3 [1] and in triphenyl phosphite [203, 103]. While some systems are characterized by weakly directional interactions [116, 217], in triphenyl phosphite the dominating interaction is expected to be non-directional, since the substance consists of a simple organic molecule with a small dipole moment and has no tendency to form hydrogen bonds [174]. Hence it is possible that LLPTs may also occur in materials characterized by non-directional interactions. This possibility is supported by a recent observation of a transition between two amorphous solid states

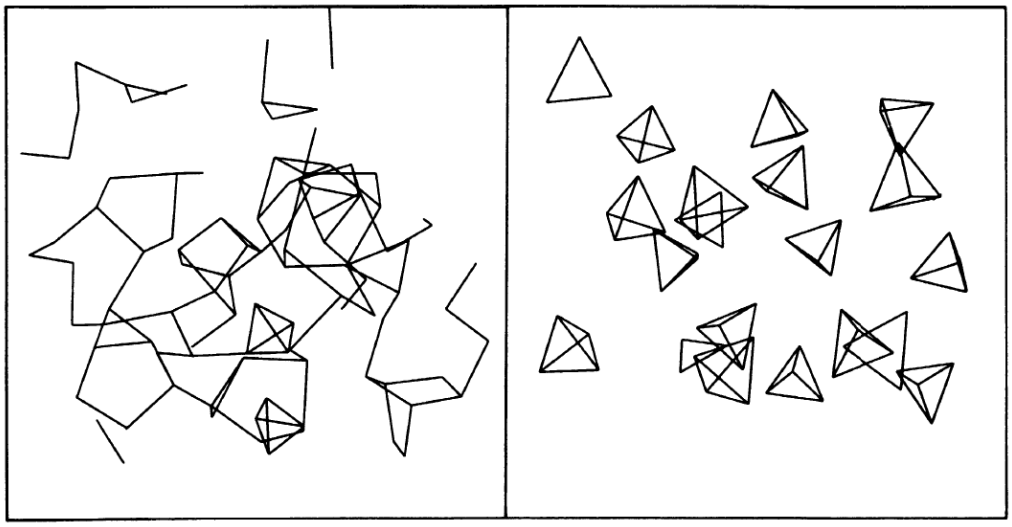

Figure 1.4: Experiments of liquid phosphorus provide a clear example of liquid-liquid phase transitions in one-component liquids. *Ab initio* simulations have confirmed that the transition is between a polymeric liquid (left panel) and a molecular liquid of P_4 molecules (right panel). Adapted from [75].

of $Ce_{55}Al_{45}$ (a metallic glass with non-directional bonds), in which the transition is caused by pressure-induced f-electron delocalization [177].

There is indirect experimental evidence for a LLPT in sulfur [26, 206, 15], selenium [91], and some molecular liquids [104, 171, 215], and several *ab initio* computer simulations suggest that LLPTs may exist in liquid hydrogen [146, 168, 23] and liquid nitrogen [22] at high pressures and temperatures.

1.1.3 LLCP hypothesis of liquid water

A liquid-liquid phase transition ending in a liquid-liquid critical point might also be present in supercooled water. Experiments on supercooled liquid water, done by Angell and Speedy in the 1970s, indicate a huge increase in the heat capacity (Fig. 1.5a) and the compressibility (Fig. 1.5b) upon lowering the temperature [13, 183, 14, 182]. The steep increase in both response functions seems to imply some

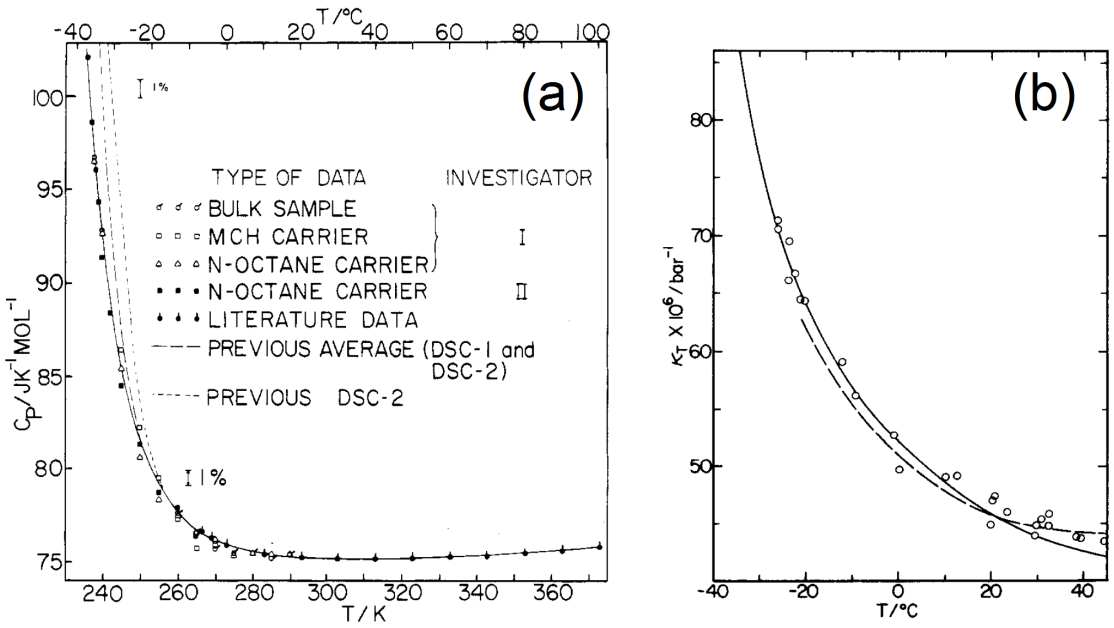

Figure 1.5: Behavior of (a) heat capacity C_P [14] and (b) compressibility K_T [183] in supercooled liquid water, at atmospheric pressure. The steep increase of both response functions upon cooling might indicate the presence of a critical point below 233 K (−40 °C).

kind of critical phenomenon in supercooled liquid water at very low temperatures. Unfortunately, homogeneous nucleation limits the experiments to $T > T_H$ (with $T_H \approx 233$ K at 1 bar) as spontaneous crystallization rapidly occurs below this temperature. Note that the homogeneous nucleation line is a *kinetic* boundary, and not a thermodynamic boundary such as the melting line. This means that the exact value of T_H depends on the speed of the experiment – the faster you do the measurement, the lower T_H is – and that, in principle, the liquid can be cooled to much lower temperatures.

Instead of carefully cooling liquid water, it is also possible to quickly quench water to much lower temperatures, and produce a glassy state of water. Creation of such a glass can be accomplished in several ways [31, 27, 127]. For example, compressing hexagonal ice at 77 K to a pressure above 10 kbar creates a *high-*

density amorphous ice (HDA) that has a density of about 1.17 g/cm^3 at 1 atm (0.1 MPa) and 1.31 g/cm^3 at 1.0 GPa [128]. A glassy state called *amorphous solid water* (ASW) is formed by slowly depositing water vapor onto a very cold metal surface below 120 K [140]. The latter is very similar to another glassy water state called *low-density amorphous ice* (LDA), which has a density of about 0.94 g/cm^3. It has been shown by Mishima *et al.* that LDA and HDA are separated by a reversible abrupt change in density that resembles a first-order phase transition[2] [128, 126, 129, 130].

Increasing the temperature of LDA or HDA does not turn the glass into a liquid, but leads once again to crystallization. This happens around a temperature of T_X, which lies below the homogeneous nucleation temperature T_H. Just like T_H, the glass-crystal transition temperature T_X represents a kinetic boundary that has no fundamental value but merely depends on the time-scale of the measurement.

Experiments done so far have only been able to probe liquid water at $T > T_H \approx 233\ K$ (1 bar) and glassy water at $T < T_X \approx 150\ K$, which means that there is a region in between T_H and T_X that is currently inaccessible to experiments, known as the "no-man's land" of liquid water [118] (see Fig. 1.6). Fortunately, computer simulations can probe much shorter time-scales than is possible in experiments. In fact, Poole *et al.* performed simulations [152] with a water model called ST2, and discovered a liquid-liquid critical point (also indicated in Fig. 1.6). This result has been reproduced with several other water models, such as TIP5P [224] and TIP4P-Ew [144], but not with others, such as mW [78]. In addition, there has even been some debate about the existence of the LLCP in ST2 [110, 111], but subsequent studies have confirmed its existence [173, 112, 96, 149].

[2]Technically, a first-order phase transition can only occur between two stable phases. Since LDA and HDA are metastable, the transition is sometimes referred to as a first-order-*like* phase transition.

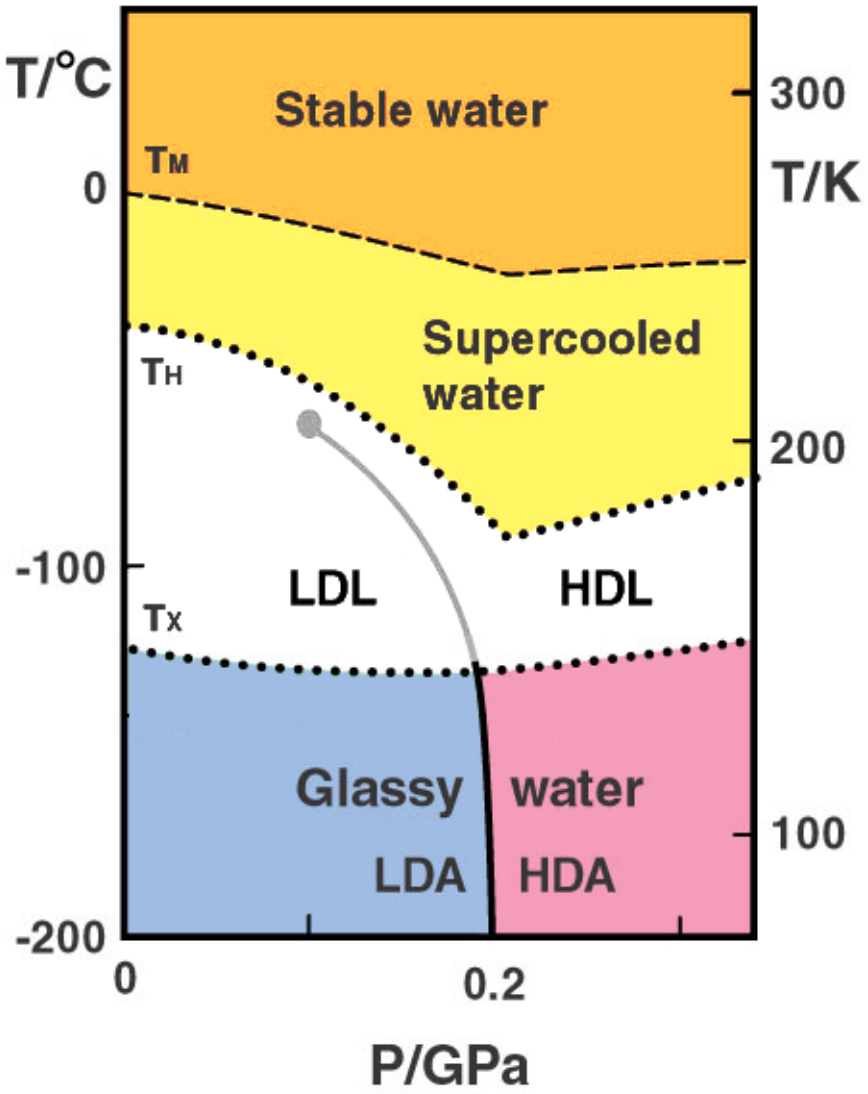

Figure 1.6: The liquid-liquid critical point hypothesis of water (courtesy of Dr. O. Mishima). Liquid water (orange) can be cooled to below the melting temperature T_M, producing supercooled liquid water (yellow). As of yet, experiments have failed to measure the liquid below T_H, as homogeneous crystallization occurs too quickly. It is possible, however, to quench the liquid into a glassy state. Heating glassy water does not produce a liquid, but leads once again to crystallization above T_X. There are two main types of glassy water, low-density amorphous (LDA, in blue) and high-density amorphous (HDA, in pink), which are separated by a first-order transition around 0.2 GPa (thick black line). According to the LLCP hypothesis, this transition continues deep into the "no-man's land" (white), where it becomes a phase transition line between two liquids – low-density liquid (LDL) and high-density liquid (HDL) – and finally ends in a liquid-liquid critical point.

The LLCP hypothesis would nicely explain the diverging behavior of C_P and K_T (Fig. 1.5), as well as the phase transition between LDA and HDA. The liquid-liquid phase transition would separate two distinct metastable liquids: the low-density liquid (LDL) and the high-density liquid (HDL). Upon lowering the temperature, LDL would vitrify into the amorphous ice LDA, and similarly HDL would turn into HDA (Fig. 1.6).

There are several alternative theories that predict what happens in the "no man's land", some examples being the singularity-free scenario [167] and the retracing spinodal scenario [182, 181]. Even though the LLCP scenario seems to have gained the most attention in recent years, it is ultimately up to the experimental community to provide a definite answer.

1.2 Water and its anomalies

Clearly, water is a particularly interesting liquid to study. It is the most common liquid on Earth; not only does it cover 70% of the Earths surface, it also makes up over 50% of the human body. It is of major importance to all living things and many important chemical and biological processes occur within an aquatic environment. But water is not only the most abundant liquid; compared with other liquids it is also one of the most unusual. Although H_2O seems to be a very simple molecule, its liquid state displays very anomalous behavior. An example of such an anomaly is the phenomenon that ice floats on liquid water, while for most materials the solid state has a higher density than its liquid state. Another example is the unusually high boiling point of H_2O compared to similar molecules such as H_2S, H_2Se, and H_2Te; see Fig. 1.7. In this section we shall enumerate several anomalies which will be further explored in this thesis.

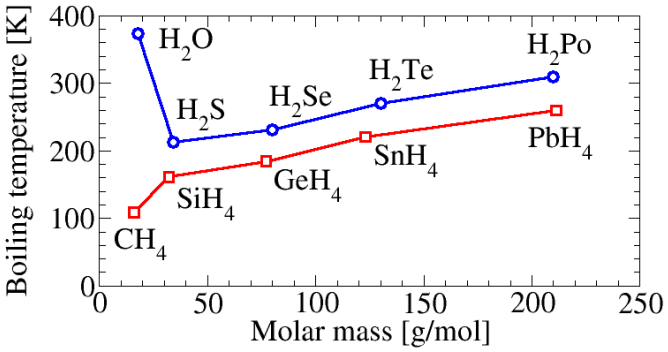

Figure 1.7: Boiling points of the hydrides of Groups IV and VII. Hydrogen bonds are responsible for the anomalously high boiling point of water, as in comparison to the other hydrides.

1.2.1 Density anomaly

A very important anomaly of water is the density anomaly. If we measure the density as a function of temperature, while keeping the pressure fixed, one finds that the density has a maximum at the so-called "temperature of maximum density" (TMD). The existence of the TMD has been known for centuries, and its value is well known: 3.98 °C at 1 bar.

In terms of thermodynamics, the TMD can be defined as the temperature for which the coefficient of thermal expansion is zero:

$$\alpha_P \equiv \frac{1}{V}\left(\frac{\partial V}{\partial T}\right)_P = 0 \tag{1.3}$$

The density anomaly is then the range of temperatures for which $\alpha_P < 0$. On a pressure-temperature plot (the PT-plane) the TMD can be traced as a curve that encloses the density anomaly region. If the TMD line is not interrupted by a phase transition line, then it curves back at low pressures, indicating a temperature of *minimum* density (TmD). Thermodynamically, both the TMD and TmD are equivalent, as $\alpha_P = 0$ for both.

Note that the density anomaly we are considering here is not the same anomaly as ice floating on water, although both anomalies are related. In this thesis we define the density anomaly as *a range of temperatures, where an decrease in temperature leads to an decrease of the density of the liquid*, i.e. where $\alpha_P < 0$. Hence, this definition only concerns the liquid and does not involve the density of ice.

The density anomaly of liquid water has profound consequences for life on earth. Water at a temperature of 4 °C will always sink to the bottom of a lake, regardless of the temperature of the air above it. Apart from providing a constant temperature environment, this also means that the bottom of a lake is unlikely to freeze during winter, thus protecting fish and other aquatic life from the icy temperatures above the lake's surface.

Most liquids do not exhibit a density anomaly. Usually, as the temperature goes up, molecules in the liquid move faster, and basically push each other away. Therefore, as T goes up, the volume increases and the density goes down. The reason why this does not happen for water below 4 °C, is mainly because of hydrogen bonds. Hydrogen bonds are much stronger than the regular van der Waals forces between molecules[3], and because the H-O-H angle of a water molecule (104.5 °) is close to the ideal tetrahedral bond angle of $\arccos(-1/3) \approx 109.5\,°$, the molecules prefer to form an open hexagonal lattice such as that of hexagonal ice (Fig. 1.8). This crystal structure has exactly four nearest neighbors, while liquid water has slightly more than four, on average. Below 4 °C, as the liquid is cooled, the number of nearest neighbors is reduced (getting closer to four), and this leads to the decrease in density [147].

[3]Hydrogen bonds in water have a length of 1.97 Å(compared to a water molecule with an approximate diameter of 2.75 Å) and an energy of about 21 kJ/mol (8.5 kT at room temperature).

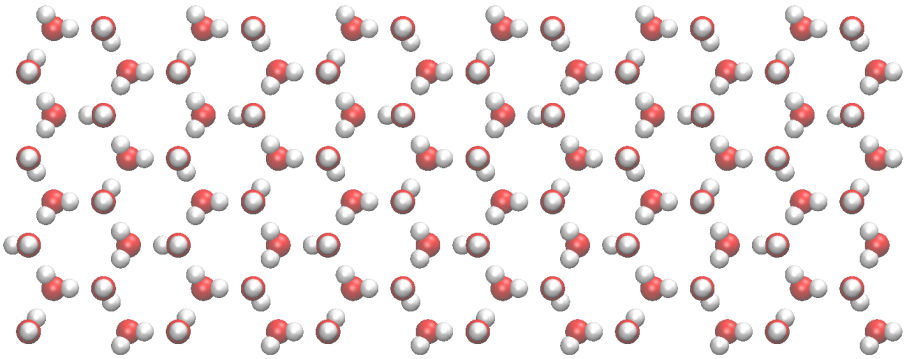

Figure 1.8: Snapshot of one layer of hexagonal ice (Ih).

1.2.2 Diffusion anomaly

The molecules inside a liquid are constantly in motion. At very short time scales (on the order of femtoseconds and below), the molecules move according to

$$r_{\text{rms}} \approx v_{\text{rms}} t \tag{1.4}$$

with $r_{\text{rms}} \equiv \sqrt{\langle r(t)^2 \rangle}$ the root-mean-square displacement after a time t, and $v_{\text{rms}} = \sqrt{3k_B T/m}$ the root-mean-square speed. This is known as the "ballistic regime" of the diffusion, because in the limit $t \to 0$ the molecule follows a simple ballistic trajectory.

In glassy systems, the ballistic regime is followed by a plateau where $\langle r(t)^2 \rangle$ is virtually independent of time. The slow movements of the molecules lead to an effect where each molecule is essentially trapped by its nearest neighbors. It takes a lot of time for a molecule to escape this "cage" of neighboring molecules, and therefore the mean squared displacement $\langle r^2 \rangle$ is nearly constant and equal to the size of the cage. For obvious reasons, this regime is often called the "cage regime".

At large timescales, the diffusion of a molecule is governed by Brownian dynamics. Collisions with other molecules lead to a random walk trajectory, with the mean

squared displacement given by

$$r_{\mathrm{rms}} \equiv \sqrt{\langle r(t)^2 \rangle} = \sqrt{6Dt} \tag{1.5}$$

Here D is the diffusion coefficient. At these timescales the motion is truly diffusive, and we have reached the "diffusive regime". The diffusion coefficient for a water molecule inside water (i.e. the self-diffusion) is about 10^{-5} cm^2/s.

For most liquids, increasing the pressure leads to molecules being closer together, which makes it harder for one molecule to pass its neighbor. Hence, increasing the pressure usually causes the diffusion coefficient to go down. Water, however, has a diffusion anomaly: within a certain range of temperatures the diffusion goes *up* when you increase the pressure (see Fig. 1.9).

In addition to the density anomaly, also the diffusion anomaly of water can be explained with hydrogen bonds and the tetrahedral liquid structure that they

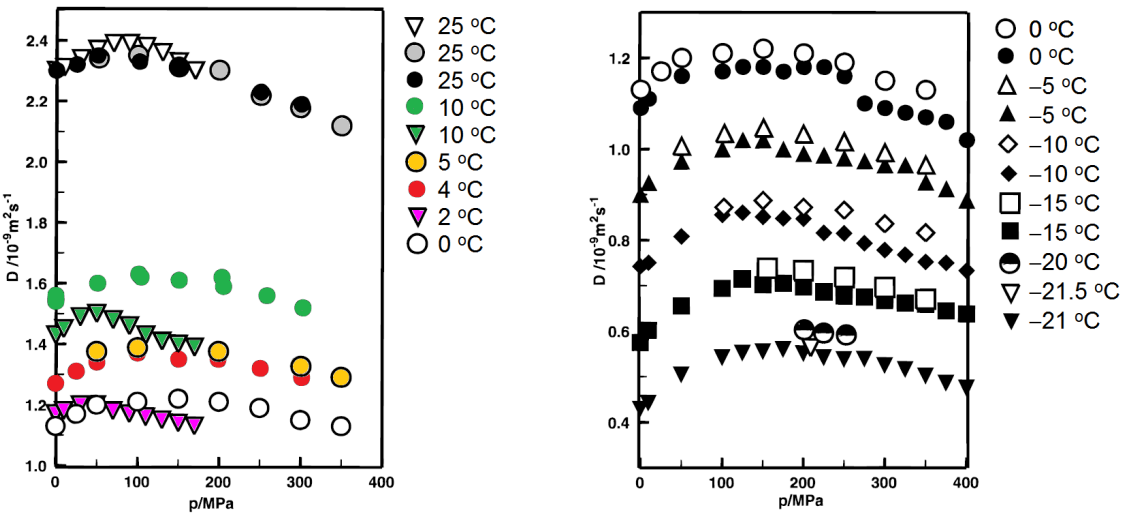

Figure 1.9: The diffusion anomaly of liquid water: at low temperatures (and below 100–200 MPa) the diffusion increases upon increasing the pressure (adapted from [68]). Left panel: diffusion above the melting line. Right panel: diffusion of supercooled water.

produce. Applying pressure to the tetrahedral hydrogen bond network causes bonds to break or bend. This makes it easier for water molecules to move around, and thus an increase in pressure leads to an increase in diffusion.

1.2.3 Compressibility anomaly

The isothermal compressibility K_T indicates how much the volume of a liquid changes when pressure is applied while the temperature is kept constant:

$$K_T \equiv -\frac{1}{V}\left(\frac{\partial V}{\partial P}\right)_T \tag{1.6}$$

The compressibility is always positive, because it is impossible for any material to have an increase in volume while pressure is increased. This fact is made explicit in the definition through the minus sign; an increase in P leads to a decrease in V, so $\frac{\partial V}{\partial P} < 0$ such that $K_T > 0$.

The derivative of K_T, however, is not restricted by thermodynamics. Nonetheless, for most liquids K_T increases as the temperature is increased or the pressure reduced. Increasing the temperature causes the molecules to move more, making it easier for the liquid to be compressed – and K_T goes up. On the other hand, applying pressure forces the molecules closer together, which makes the liquid more compact and therefore harder to compress further (thus K_T goes down). Liquid water is anomalous in this aspect, because at low temperatures the liquid becomes more stiff (K_T goes down) upon heating (see e.g. Fig. 1.5b).

The compressibility anomaly is closely related to the density anomaly. In fact, it has been shown by Sastry *et al.* [167] that if a liquid has a density anomaly (i.e. expands upon cooling) that thermodynamics demands that the compressibility increases upon lowering the temperature as well. Furthermore, the locus of K_T

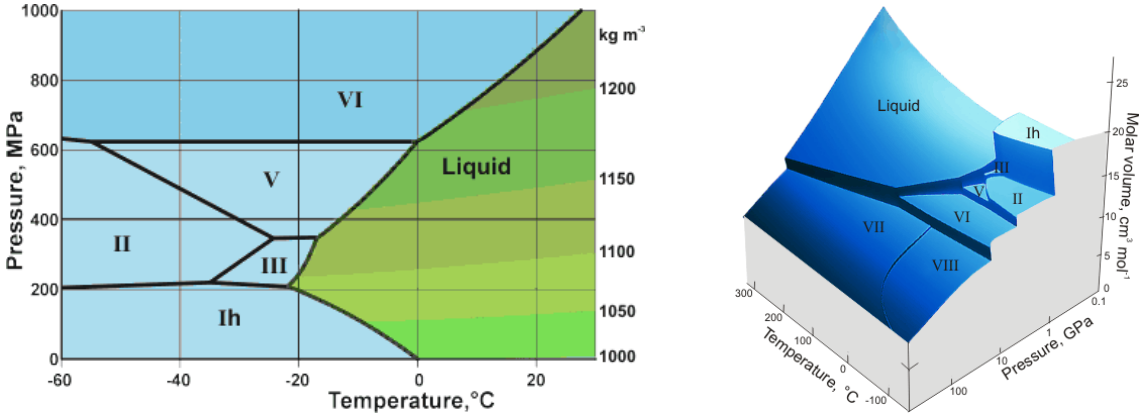

Figure 1.10: Part of the phase diagram of H_2O (both figures from [213]). In the left figure it is particularly clear that the melting line between ice-Ih and the liquid has a negative slope, meaning that it is possible to melt the crystal by applying pressure.

maxima always crosses the TMD curve exactly where its slope is infinite in the PT-diagram, i.e., where $\left(\frac{\partial P}{\partial T}\right)_{\alpha_P=0} = \infty$ [167]. It is possible, however, to have a compressibility anomaly without a density anomaly. One such example is the cut-ramp potential with parameter $\lambda > 0.28$, which is discussed in Sec 2.4.

1.2.4 Negatively-sloped melting line

One unique thing about water is that it has a rich polymorphism; there exist many different crystal structures of ice. As of 2014, there are sixteen different crystalline phases of H_2O known: hexagonal ice (Ih), cubic ice (Ic), and the ices II, III, ..., XV. Most of these are stable crystalline phases, with the exception of ice-four (IV), ice-nine (IX), and ice-twelve (XII) which are metastable. A few of these ices are shown in Fig. 1.10.

Fig. 1.10 also shows that the melting line between ice-Ih and the liquid has a negative slope. It is therefore possible to start with hexagonal ice-Ih and pressurize it into a liquid. Normal liquids do not display this behavior, and always have a melting line with a positive slope. Upon increasing the pressure, the liquid becomes

more compact, the movement of the molecules becomes more constrained, and this allows crystal nuclei to grow into full crystals[4].

With respect to the crystal, melting leads to a gain in entropy caused by the spatial randomization of the molecules: $\Delta S = S_{\text{liquid}} - S_{\text{crystal}} > 0$. At the same time, melting also leads to a gain in enthalpy, $\Delta H = H_{\text{liquid}} - H_{\text{crystal}} = \Delta E_{\text{tot}} + P\Delta V > 0$, mainly because the liquid occupies a larger volume than the crystal (for normal liquids $\Delta V > 0$). Melting occurs when the change from crystal to liquid lowers the Gibbs energy:

$$\Delta G = E_{\text{liquid}} - E_{\text{crystal}} + P(V_{\text{liquid}} - V_{\text{crystal}}) - T(S_{\text{liquid}} - S_{\text{crystal}}) < 0 \qquad (1.7)$$

We see that, when $\Delta V > 0$, a decrease in P or an increase in T makes this inequality easier to be satisfied, and thus promotes melting.

On the other hand, ice-Ih has a lower density than liquid water (see Fig. 1.10) which means that $\Delta V < 0$ and therefore an *increase* of pressure actually promotes melting. All of this is nicely summarized by the Clapeyron relation, which relates the slope dP/dT of a phase transition line to the change in entropy and volume:

$$\frac{dP}{dT} = \frac{\Delta S}{\Delta V} \qquad (1.8)$$

It should be noted that this relationship is valid for any phase transition line, including liquid-liquid phase transitions.

It is commonly believed that the negative slope of the ice-Ih melting line is the reason why we can skate on ice—the weight of a person on ice skates exerts a large pressure on the ice, which causes the ice to melt slightly, and this layer of water

[4]Crystal nuclei always form within a liquid, but when T is too high or P too low, the nuclei remain small and cannot survive long enough to start crystal growth (see also Chapter 3).

reduces the friction between the skates and the ice. However, this explanation is only partially true [145]. The reduced friction is indeed caused by a very thin layer of water, but pressure is not the main reason why that layer is there. A simple calculation of the pressures involved shows that the pressure of a skate is only sufficient to cause melting when the ice is very close to its melting point. Instead, simple frictional heating plays the most important role, possibly together with the existence of an ultra-thin surface layer of disorganized and weakly held frozen water that naturally occurs [213, 145].

For some liquids the melting line has a positive slope at very low and very high pressures, as well as a region at medium pressures where the melting line has a negative slope. A consequence of this S-shaped melting line is that it is possible to pressurize the liquid into a crystal, and then pressurize it further until it hits the melting line a second time, turning the crystal back into a liquid. This phenomenon is called "re-entrant melting". Increasing the pressure even further would finally lead to second crystallization event, possibly with a different crystal structure.

1.3 Conclusion

Even though many of the anomalies of water can be explained by the hydrogen bonds and the formation of a tetrahedral network of bonds, there exist liquids that display some or all of these phenomena without having any hydrogen bonds. It is important to understand the origin of these anomalies and their relation with a possible liquid-liquid critical point. Not only is the question "What is the cause of these anomalies?" an interesting question from a purely scientific point of view, it also is likely that the answer will be useful to experiments involving liquids, chemical engineers, and industry. It might be even possible to engineer a liquid such that it

has one of these anomalies.

Take for example the diffusion anomaly. If increasing the pressure on a particular liquid leads to a higher diffusion coefficient (and reduced viscosity), then this might be extremely useful regarding the transport of the liquid. Other applications might benefit from the density anomaly, which can lead to a constant-temperature region at the bottom of a tank (similar to the 4 °C water at the bottom of a lake in the winter).

In Chapter 2 we start this research by considering several simple models. Although they cannot provide any quantitative results, they are the best method to obtain a good understanding of the physics involved. We then continue in Chapter 3 with a more realistic model: the ST2 model for water. It is the same model that was used by Poole *et al.* to predict the LLCP in water, and is still considered the best model when investigating the LLCP in liquid water. In Chapter 4 we consider two models of liquid silica, and investigate the possibility of having a LLCP in that liquid. We end this thesis with a short discussion and outlook in Chapter 5.

CHAPTER 2: Phase transitions and anomalies in simple models

> *If, in some cataclysm, all scientific knowledge were to be destroyed, and only one sentence passed on to the next generation of creatures, what statement would contain the most information in the fewest words? I believe it is the atomic hypothesis (or atomic fact, or whatever you wish to call it) that all things are made of atoms—little particles that move around in perpetual motion, attracting each other when they are a little distance apart, but repelling upon being squeezed into one another.*
>
> – Richard. P. Feynman, in *Lectures on Physics*

2.1 Introduction

Simple models are possibly the most valuable tool to a theorist. Although one cannot expect to obtain any quantitative results from them, they are incredibly useful to obtain an understanding of the mechanisms and processes involved that lead to the behavior one is interested in.

One of the simplest models for liquids is the popular Lennard-Jones potential, $U_{LJ}(r) = 4\epsilon[(\sigma/r)^{12} - (\sigma/r)^6]$, where ϵ indicates the energy scale and σ the length scale (see Fig. 2.1). The interaction is spherically symmetric and only depends on the distance r between two atoms. The force between two atoms simply follows from $F = -dU/dr$, and the movements of the atoms obey simple Newtonian classical mechanics.

This model captures one of the most fundamental properties of atoms: at very short distances the atoms repel, but at larger distances the attract each other. The $1/r^6$ term represents the long-range van der Waals (dipole) attraction, while the

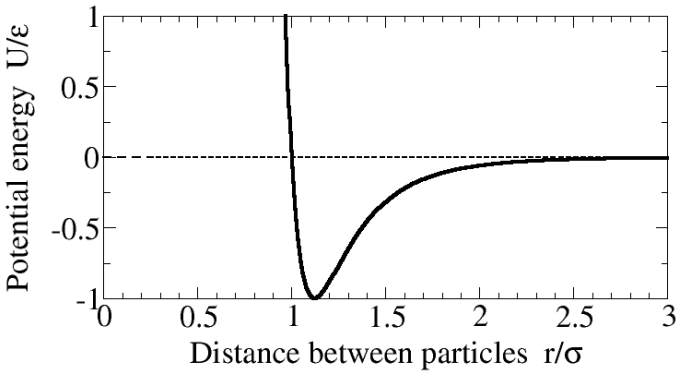

Figure 2.1: The Lennard-Jones potential captures the most important aspect of atomic interactions: short-range repulsion at $r < \sigma$, together with a long-range attraction at $r > \sigma$.

$1/r^{12}$ term describes the short-range Pauli repulsion that is caused by overlapping electron orbitals (the exchange interaction). The 12th power is mainly chosen for computational efficiency, as it is exactly the square of the $1/r^6$ term. In other models the attractive $1/r^6$ term is combined with a different repulsive term, such as an exponential in the case of the Buckingham potential.

The LJ potential works remarkably well for "simple liquids" such as liquid argon. However, it fails to accurately describe more complex liquids such as those that have directional bonds, or ionic liquids where the electrostatic interaction plays an important role. The potential also fails for very small atoms such as liquid hydrogen or helium, where quantum mechanics has a considerable effect.

It should therefore come as no surprise that the LJ potential shows no sign of water-like anomalies, as water is a very complex liquid. Surprisingly, however, there are simple spherically symmetric potentials such as the Jagla potential (or "spherical water") that are actually able to reproduce several of the anomalies that are present in water [87, 222, 219]. Evidently, these models might provide some insight into what is causing these anomalies.

2.2 Anomalies: two competing length scales

As is the case with the Lennard-Jones potential, a liquid consisting of hard spheres ("billiard balls") does not produce any water-like anomalies, although hard spheres can be used to simulate crystal-liquid phase transitions [79]. However, when adding a "soft core" to the hard sphere potential it is possible to introduce anomalies.

Soft core potentials have a long history of being used to model isostructural critical points in crystals [73, 193, 229, 209], polymorphism of crystal phases [85, 86, 33, 34], liquid-liquid phase transitions (LLPTs) [45, 44, 157, 86, 87, 56, 29, 30, 65], polymorphism in glasses [88, 98, 222, 220], and anomalous thermal expansion of liquids at low temperatures [44, 41, 42, 195, 157, 86, 158, 216, 98, 226, 135, 225, 227, 142]. All these phenomena can be associated with the existence of two competing local structures: an expanded structure characterized by large open spaces between particles, and a collapsed structure in which particles are spaced more closely. The expanded structure is the result of interactions between the particles, which differ depending on the material.

In water, for example, the expanded structure is caused by the hydrogen bonds that favor a tetrahedral network of water molecules such that each molecule has only four nearest neighbors (the extreme case being the crystal structure of hexagonal ice). In other words, the first coordination shell of liquid water consists of only four molecules [24, 172, 35, 170, 180, 25, 29, 224, 162, 143, 151, 198, 117, 228, 223]. This is in comparison with simple liquids, such as argon, where the first coordination shell consists of approximately twelve particles arranged in a closely-packed configuration. Accordingly, water has much more empty space between molecules than argon and its density can be significantly increased by increasing the pressure which distorts the hydrogen bond structure and increases the number of particles in the

first coordination shell [42]. This distortion is associated with an increase in entropy, which leads to a density anomaly (via a Maxwell relation):

$$\alpha_P \equiv \frac{1}{V}\left(\frac{\partial V}{\partial T}\right)_P = -\frac{1}{V}\left(\frac{\partial S}{\partial P}\right)_T < 0, \tag{2.1}$$

where α_P is the thermal expansion coefficient (see also Eq. 1.3).

Probably one of the easiest examples of a soft core potential is the addition of a linear ramp to the hard sphere potential [73, 193, 85]:

$$U(r) = \begin{cases} \infty & \text{for } r \leq \sigma_0, \\ (1 - r/\sigma_1)U_1 & \text{for } \sigma_0 < r < \sigma_1, \\ 0 & \text{for } r \geq \sigma_1. \end{cases} \tag{2.2}$$

It has been shown that this hard-core plus linear ramp (HCLR) potential can display water-like anomalies, provided that the ratio $\Lambda \equiv \sigma_0/\sigma_1$ between the hard core radius σ_0 and the total interaction range σ_1 is not too large [225]. We consider here $\Lambda = 4/7$ (for which anomalous behavior was reported in [98]) and analyze the relationship among the melting line, the anomalous behavior, and the structural properties.

As shown in Fig. 2.2, the melting line displays a positive dP/dT slope at small pressures, consistent with the idea that particles cannot "climb up" the soft core at low densities. As the pressure increases, the soft repulsive ramp becomes less and less effective and the melting line passes through a maximum in temperature, followed by a region where re-entrant melting occurs (into a different crystal lattice). At higher pressures, where the soft repulsion becomes ineffective, the HCLR potential is characterized by the hard core repulsion, and the melting line accordingly recovers a positive slope. Ultimately the liquid crystallizes into a rhombohedral lattice [98]. The density and diffusion anomalies occur in the same pressure range where the

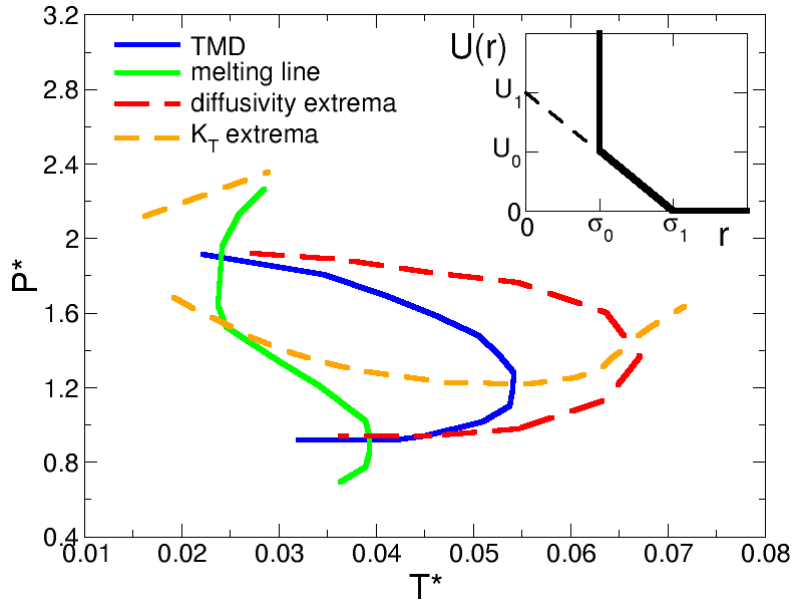

Figure 2.2: Phase diagram of the hard core plus linear ramp (HCLR) potential. Solid green line indicates the melting line. The blue solid line and red dashed lines are the temperature at maximum/minimum density (TMD) and the diffusion extrema (DM) lines, respectively. The orange dashed lines represents the loci of compressibility extrema. Axes are in reduced units: $P^* = P\,\sigma_1^3/U_1$ and $T^* = k_B\,T/U_1$. Inset: The hard core plus linear ramp potential $U(r)$ as a function of the interparticle distance r.

HCLR system undergoes re-entrant melting, while both anomalies are found to disappear at the higher pressures where the melting line recovers a positive slope.

The two repulsive length scales are quite explicit in the HCLR model: the soft core at σ_1 (effective at low P, T) and the hard core at σ_0 (effective at high P, T). The competition between these two length scales can be made evident with the structure factor (see Fig. 2.3). At very low pressures, the first peak of $S(k)$ is much larger than the second peak. This first peak is associated with the larger soft radius σ_1 (remember that k has units of inverse distance), which means that at low P most particles are located near $r = \sigma_1$ rather than $r = \sigma_0$. In that case the liquid behaves as a hard sphere liquid with particle diameter σ_1. At very high pressures the first peak disappears, indicating that the effect of the soft core completely disappears,

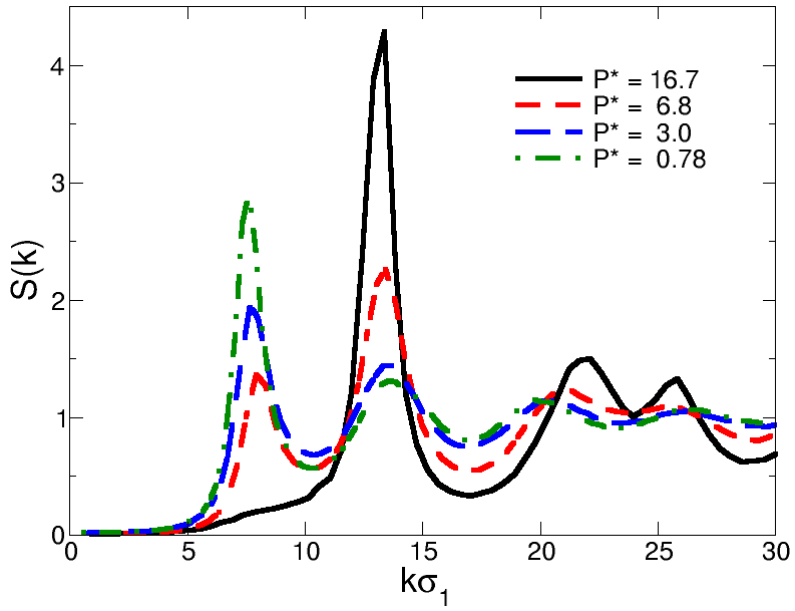

Figure 2.3: Structure factor $S(k)$ of the hard core plus linear ramp potential at constant temperature ($T^* = 0.036$) for several pressures. The first peak of $S(k)$ decreases with increasing pressure, while the second peak grows. At pressures below $P^* \approx 4$ the first peak of $S(k)$ is the largest, while the second peak is the largest above $P^* \approx 4$. At very high pressures the first peak disappears completely.

and the liquid behaves like a hard sphere potential with particle diameter σ_0.

The notion of two competing length scales can provide an intuitive explanation for all anomalies considered here. Outside the anomalous region, only one of the two length scales dominates, and the liquid behaves like a simple hard sphere liquid. Within the anomalous region (approximately between $P^* \equiv P\,\sigma_1^3/U_1 = 1$ and $P^* = 2$), the particles can temporarily jump onto the soft core if they have gained sufficient energy. This increase of particle energy can be obtained either by increasing the temperature or applying a higher pressure (i.e. by applying work).

From these considerations it is clear that increasing the temperature leads to an increase of density (the density anomaly). Increasing the pressure means the particles suddenly have *more* freedom to move, leading to an increase in diffusion (the diffusion anomaly). For the same reason, the crystal can become unstable when

we increase P, and thus applying pressure turns the crystal into a liquid (re-entrant melting). Also, near the anomalous region the liquid becomes easier to compress upon increasing pressure, which constitutes to the compressibility anomaly bounded by the compressibility maxima.

2.3 Anomalies and the liquid-liquid critical point

When an interaction potential introduces two separate length scales, it is possible for the liquid to locally exhibit two different liquid structures: a low-density liquid (LDL) and a high-density liquid (HDL). However, the hard core plus linear ramp (HCLR) model of the previous section shows no sign of a liquid-liquid phase transition. The reason for this is simple; the potential is repulsive everywhere and has no attractive part. Therefore the two different liquid phases cannot coalesce, i.e., there is no phase segregation, and thus no phase transition between the liquids.

Adding an attractive tail to the HCLR potential indeed introduces a liquid-liquid phase transition (LLPT) line. The one-dimensional version of this model was studied by Hemmer and Stell in 1970 [73], but it was not until 1999 that E. A. Jagla did computer simulations of the model in three dimensions [86] and pointed out that the model displays water-like anomalies as well as a liquid-liquid critical point (LLCP). Depending on the parameters, the model can produce the LLCP in the supercooled region or in the stable region of the phase diagram, i.e., above the melting line.

In 2001 Jagla introduced a similar model [87] consisting of a hard core and two

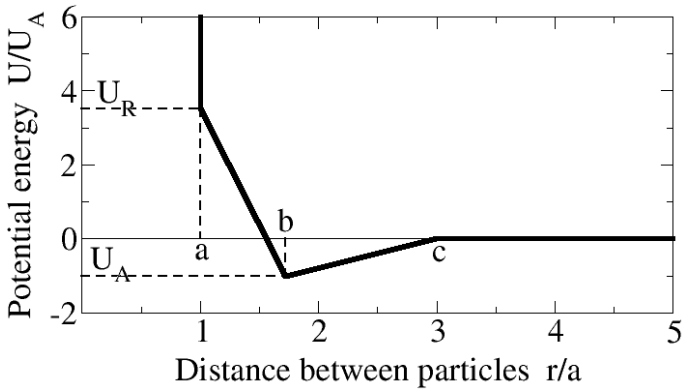

Figure 2.4: The Jagla potential consists of a hard-core at $r = a$, a soft repulsive ramp at $a < r < b$, and an attractive tail at $b < r < c$.

linear ramps, nowadays known as the Jagla model or spherical water model,

$$U_{\text{Jagla}}(r) \equiv \begin{cases} \infty & r < a \\ U_A + (U_R - U_A)(b - r)/(b - a) & a \leq r < b \\ U_A(c - r)/(c - b) & b \leq r < c \\ 0 & c \leq r \end{cases} \tag{2.3}$$

Here $b = 1.72a$, $c = 3a$, and $U_R = 3.5U_A$ are most commonly used [222, 219] (see Fig. 2.4). With these values for the parameters, the model has a liquid-liquid phase transition ending in a liquid-liquid critical point (LLCP) that lies above the melting line, within the stable region of the liquid. The critical point is therefore easy to access, and for that reason this model has been extensively studied [222, 219], in particular in relation to the liquid-liquid critical point hypothesis of water.

Even though the Jagla model displays several of the anomalies of water (see Fig. 2.5), there are some distinct differences between the phase diagram of the Jagla model and the phase diagram of water according to the LLCP hypothesis. Apart from the critical point being in the stable region—which is obviously not the case for water—the Jagla model also displays a phase transition line with a positive slope,

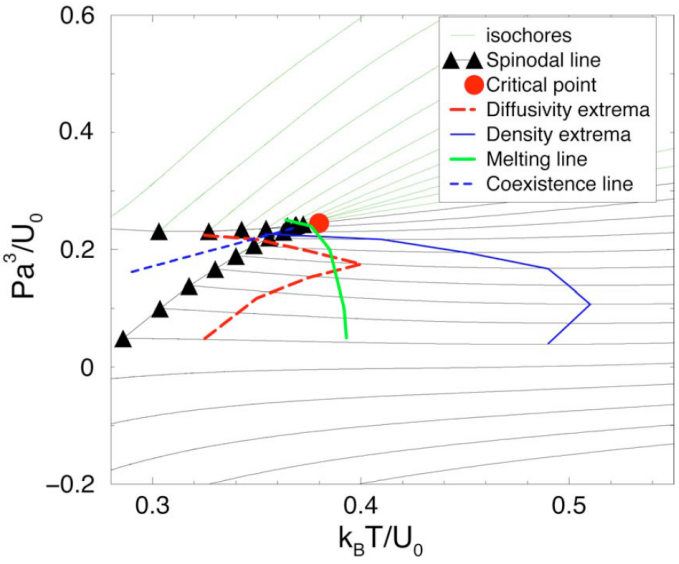

Figure 2.5: Phase diagram of the Jagla model (from [219]). In the PT-plane, the isochores (gray lines) cross at the critical point (red dot) and within the LDL-HDL coexistence region. The coexistence region is bounded by the LDL- and HDL-spinodals (indicated by the black triangles), which separates the region where LDL/HDL is metastable from the region where LDL/HDL is unstable. It is clear that the critical point lies above the melting line (green curve), and thus within the region where the liquid is stable. The density anomaly (bound by the TMD, indicated by the blue curve) and the diffusion anomaly (dashed red curve) are also shown.

while the phase transition line of water would have to be negative.

Recent studies [65] have indicated that these two discrepancies are in fact related to each other. By adjusting the parameters such that the Jagla potential becomes more and more like the Lennard-Jones potential, one finds that the critical point crosses the melting line, moves deeper and deeper into the supercooled region, until at some point the critical point crosses the homogeneous nucleation line and can no longer be observed because of spontaneous crystallization. At the same time the positive slope of the phase transition line becomes smaller and smaller, until it becomes almost negative. The transition of the slope from positive to negative occurs exactly when the critical point is close to the homogeneous nucleation line (Fig. 2.6).

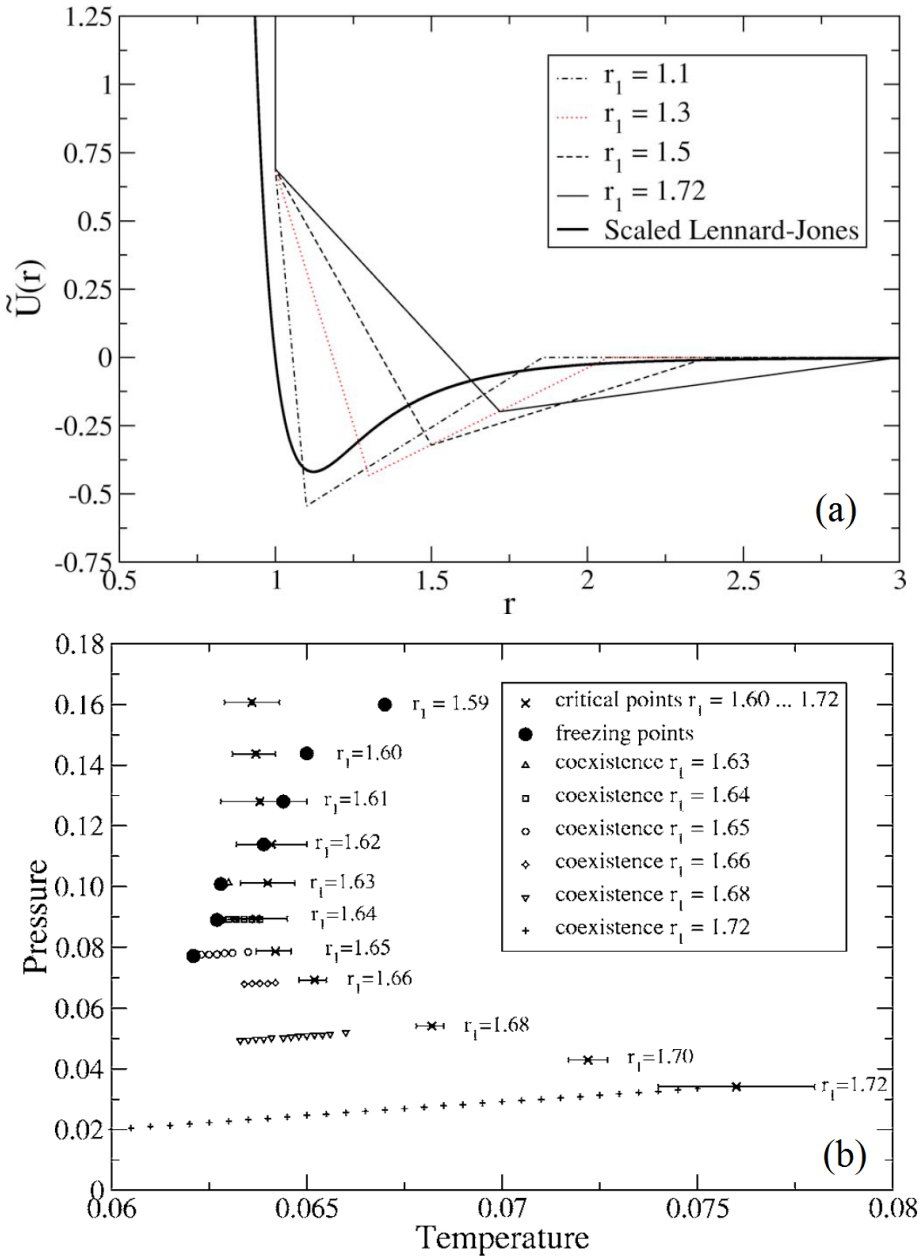

Figure 2.6: Changing the parameters of the Jagla model can make the LLCP disappear. (a) It is possible to change the value of $r_1 \equiv b/a$ such that the standard Jagla model ($r_1 = 1.72$) starts to looks more like the Lennard-Jones potential (at $r_1 \approx 1.1$). (b) The effect of this is that the location of the LLCP (crosses) moves to lower temperatures while the freezing temperature (black dots) rises. This means that the critical point moves from the stable region into the metastable supercooled region, until at $r_1 < 1.59$ the critical point can no longer be measured (figures adapted from [65]).

2.4 Soft core bounded repulsive interaction potentials

In the previous sections we have seen that several water-like anomalies can be explained by the principle of having an interaction potential that has two competing length scales. To obtain a better appreciation of the details of this principle, we shall investigate in this section a model [107] that at first glance appears to defy what we have just learned. The "uncut linear ramp model" has only *one* length scale, but still shows the usual set of anomalies. We can introduce a second length scale by cutting the potential at a certain height, but this actually *removes* the anomalies even though there are now two length scales.

The family of interactions we consider here is called the "cut ramp potential" and is obtained by cutting a repulsive linear ramp at different heights (see also Fig. 2.7):

$$U_{\rm cr}(r) \equiv \begin{cases} (1-\lambda)U_1 & \text{for } r \le \sigma_{\rm cut}, \\ (1-r/\sigma_1)U_1 & \text{for } \sigma_{\rm cut} < r < \sigma_1, \\ 0 & \text{for } r \ge \sigma_1, \end{cases} \tag{2.4}$$

where $\lambda \equiv \sigma_{\rm cut}/\sigma_1$. For $\lambda = 0$ the potential in Eq. (2.4) corresponds to the uncut repulsive linear ramp, whereas for $\lambda > 0$ it possesses a flat region where the repulsive force vanishes for $r \le \sigma_{\rm cut}$. As λ increases, the flat top gets larger and larger, until in the limit $\lambda \to 1$ the potential approaches that of the "penetrable sphere model" [109].

The unique thing about these potentials is that they do not diverge to infinity as $r \to 0$, and they are therefore known as bounded potentials. Of course, in the context of microscopic interactions of atomic systems, bounded potentials are unphysical—the strong repulsion at short distances (the Pauli repulsion) always prevents full particle overlap in a true microscopic interaction. However, if one

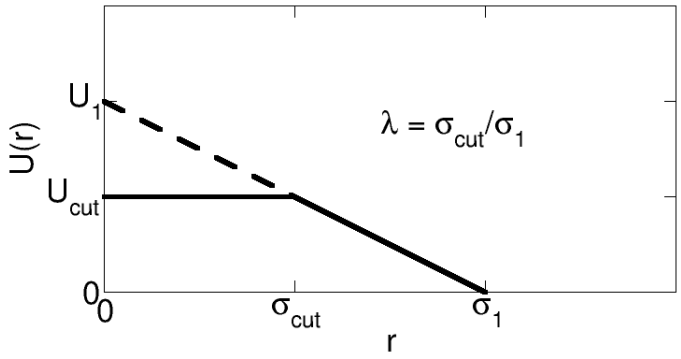

Figure 2.7: The cut ramp potential. For $\lambda \equiv \sigma_{\rm cut}/\sigma_1 = 0$ the potential $U(r)$ corresponds to the uncut ramp potential, while for $\lambda \to 1$ it becomes equivalent to the penetrable sphere model [109]. Shown here is $\lambda \approx 0.5$.

considers interactions among macromolecules such as long polymers, then *effective* interactions may result in a bounded repulsion that actually allows the particles to "sit on top of each other", imposing only a finite energy cost for a full overlap [108, 189, 81, 82]. For this reason bounded repulsive potentials have been proposed to model effective interactions in polymers, dendrimers, and microgels [108].

2.4.1 Clustering

We may expect that the overlap of particles (also called *clustering*) will have a significant effect on the behavior of the liquid. Depending on the pressure the amount of overlap can be significant, as is evident from the radial distribution function $g(r)$ of the uncut ramp potential, shown in Fig. 2.8. At low pressures the $g(r)$ looks just like any other liquid, with a large first maximum at $r = \sigma_1$ and smaller oscillations for $r > \sigma_1$. However, from the inset of Fig. 2.8 we see that when the pressure is increased above $P^* \approx 1$ a "zeroth" peak starts to grow around $r \approx 0$. This zeroth maximum never occurs in any real liquids and is an effect caused by the clustering.

In order to fully understand the behavior of this model, it is necessary to have

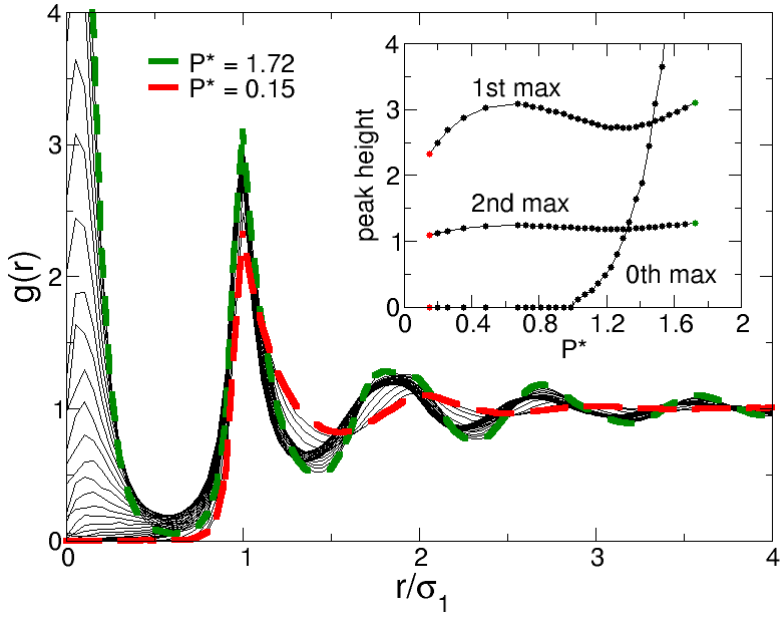

Figure 2.8: Radial distribution function of the uncut ramp potential ($\lambda = 0$) at constant temperature ($T^* = 0.040$) for several pressures, in steps of $\Delta P^* = 0.0416$. The red dashed line represents $g(r)$ for the smallest pressure ($P^* = 0.15$), and the green dashed line represents $g(r)$ for the largest pressure ($P^* = 1.72$). The apparent thick black line located between the red and green lines results from the overlap of many thin black lines in the range of pressures where $g(r)$ changes very little with pressure. Inset: Plot of the peak heights of $g(r)$ versus pressure, for the first and second maximum, as well as the "zeroth" maximum which is the peak at $r < \sigma_1$.

some kind of measure to quantify the amount of clustering. To achieve this, we adopt the average number $N_{\rm cl}$ of neighbors of a particle that lies within a distance smaller than the first minimum r_0 (with $r_0 \leq \sigma_1$) of the radial distribution function (see Fig. 2.9):

$$N_{\rm cl} \equiv \int_0^{r_0} 4\pi r^2 \rho g(r)\, dr, \tag{2.5}$$

where $\rho \equiv N/V$ is the particle density [107].

At low pressures the amount of clustering $N_{\rm cl}$ should be near zero, as the ramp starting at $r = \sigma_1$ prevents the particles from overlapping. Upon increasing the

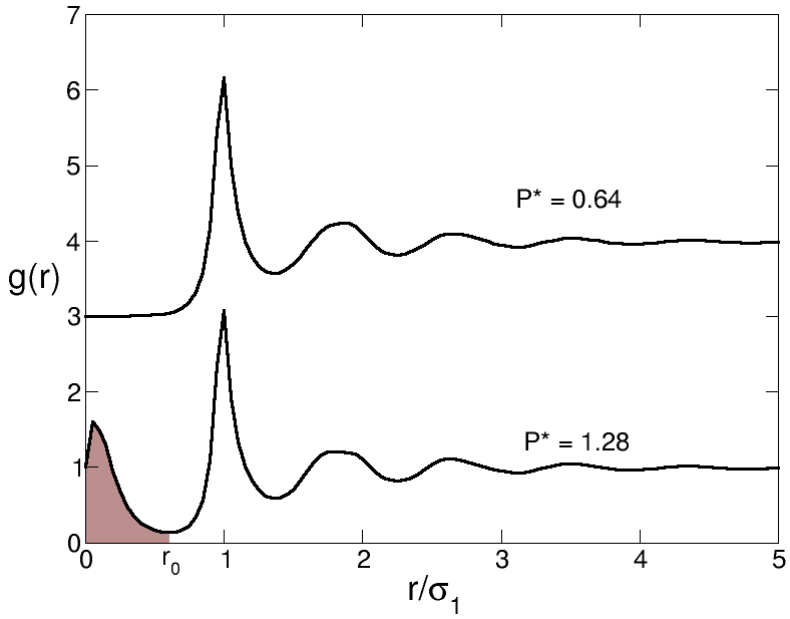

Figure 2.9: Explanation of how we determine the amount of clustering. Shown here is the radial distribution function $g(r)$ for the uncut ramp potential ($\lambda \equiv \sigma_{\rm cut}/\sigma_1 = 0$). Both graphs refer to the liquid state at $T^* = 0.035$. To quantify the amount of clustering, we calculate the average number of neighbors $N_{\rm cl}$ between $r = 0$ and r_0, where r_0 is the location of the first minimum of $g(r)$. In other words, $N_{\rm cl} \equiv \int_0^{r_0} 4\pi r^2 \rho g(r)\, dr$, with $r_0 \leq \sigma_1$. The corresponding region is indicated by the shaded area.

pressure, particles will slowly start to overlap, and $N_{\rm cl}$ attains a value between zero and one. When the pressure becomes high enough, $N_{\rm cl} \approx 1$ and most particles will completely overlap with another, effectively forming a liquid of dimers. At even higher pressures, it should be expected that multiple particles can overlap simultaneously, such that $N_{\rm cl} > 1$.

2.4.2 Calculation of the melting temperature

The standard method for locating the melting line via molecular dynamics is by doing a constant pressure/constant temperature (NPT) simulation of an elongated box that starts with one half being liquid and the other half being in the solid state. An example of such a system for the uncut ramp potential is shown in Fig. 2.10.

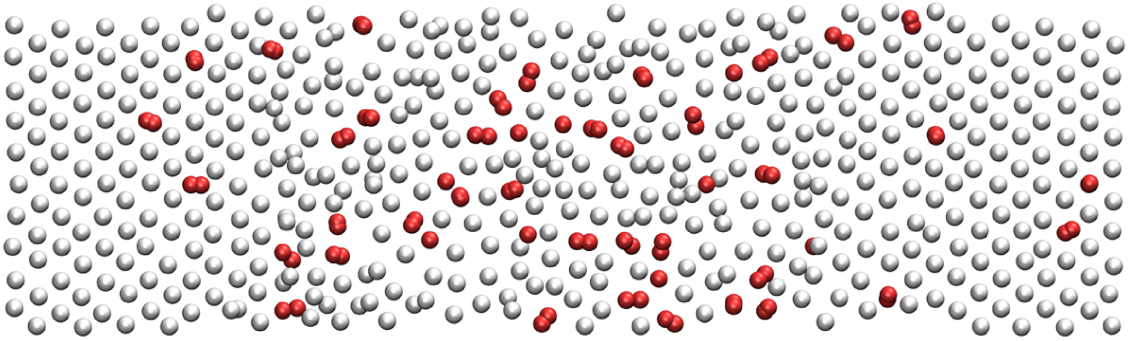

Figure 2.10: Snapshot of the liquid/crystal system for the uncut ramp potential ($\lambda = 0$) at pressure $P^* = 1.2$ and temperature $T^* = 0.035$ (on the melting line). The complete system has a size of approximately $10\,\sigma_1 \times 10\,\sigma_1 \times 36\,\sigma_1$, but shown here is a thin slice of about one σ_1 thick. The FCC structure of the crystal is clearly visible at the ends, with the liquid phase in the center. The distance between two neighboring particles in the crystal is approximately one σ_1. Shown in red are the "clustered" particles (those that lie within a distance of $0.5\,\sigma_1$ of one other). This particular state point lies well within the anomalous region where the clustering $N_{\rm cl}$ inside the liquid is much higher than in the crystal (see also Figure 2.15).

The box is chosen to be twice as long in the z-direction, as this forces the liquid-crystal boundaries to form parallel to the xy-plane (which minimizes the surface area of the liquid and is therefore energetically favored). If at a given pressure P the crystal grows, then the temperature T lies below the melting temperature $T_{\rm melt}$. However, if the liquid is found to grow, then T must lie above $T_{\rm melt}$. Fig. 2.11 shows the variations of the potential energy as a function of time. If the potential energy increases, the liquid grows, so $T > T_{\rm melt}$. By extrapolating $U_{\rm pot}(t)$ for different temperatures and looking at the slope of those curves, one can estimate the value of $T_{\rm melt}$ for a given pressure.

This procedure is a little more complicated for bounded potentials, as the particles can overlap. To prepare the initial state of half liquid/half solid, one first prepares an FCC crystal[1] in the shape of an elongated box, containing a fixed num-

[1]For the cut ramp potential with the values of λ, T, and P considered here, the crystal lattice is always FCC.

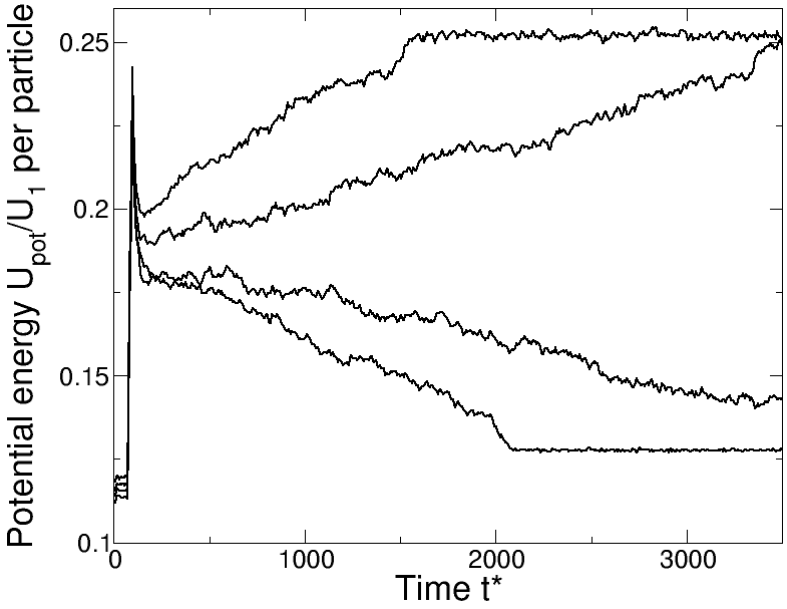

Figure 2.11: Plot of potential energy vs. time, to help determine the melting temperature $T^*_{\rm melt}$ for the $\lambda = 0$ cut at pressure $P^* = 1.12$. Shown here is the potential energy $U_{\rm pot}(t)$ for temperatures $T^* = 0.0360$, 0.0365, 0.0370, 0.0375 (from bottom to top) for a box with 5600 particles, which started as a FCC crystal. After a short equilibration period, at $t^* = 70$ half the crystal is melted by temporarily lowering the interaction potential for the particles in the center of the box. At $t^* = 100$ the interaction potential is fully restored and the simulation is allowed to run till $t^* = 3500$. By considering the slope of $U_{\rm pot}(t)$ one can determine if either the liquid or the crystal is growing. The lowest temperature (bottom curve) crystallizes completely before the simulation ends; the nearly constant potential energy indicates the system has reached an equilibrium. Similarly, the system at the highest temperature is seen to liquefy completely near $t^* = 1500$. The melting temperature at this pressure is estimated to be $T^*_{\rm melt} = 0.0367$.

ber of particles with none of them overlapping. Since cluster formation is strongly related to the density, and thus the pressure, it is important to ensure that the FCC crystal has the number of clusters corresponding to the particular pressure P at which we are trying to find the melting temperature. This can be accomplished by first melting half of the crystal at this pressure, and then making it recrystallize. Subsequently, the other half is melted and recrystallized. Additional local melting and recrystallization can be used to prevent grain boundaries from forming, to

obtain a homogeneous crystal with the correct amount of clustering.

Different methods can be used to locally melt the crystal. One such method is to temporarily replace the interaction potential by a weaker potential within a certain region of the box [107]. Once the crystal has melted in this region, the original potential is restored. To ensure recrystallization, the initial state of half liquid/half solid must be prepared at a temperature slightly below T_{melt}.

2.4.3 Effect of clustering on the anomalies

The phase diagram of the uncut ramp potential is shown in Fig. 2.12. It is remarkably similar to that of the HCLR model (Fig. 2.2); there is the density anomaly, the diffusion anomaly, the compressibility anomaly, and the melting line has a region where it has a negative slope (re-entrant melting). Furthermore, just as with the HCLR model, all anomalies occur approximately within the same region (between $P^* = 0.8$ and 1.4).

That both models show the same behavior at low P is no surprise. Equations 2.2 and 2.4 indicate that the models are identical when $r > \sigma_{\mathrm{cut}}, \sigma_0$, and at low P the particles cannot reach the hard core or the cut, but only feel the effects of the linear ramp. As indicated before, this causes the liquid to change from a normal liquid to an anomalous liquid as the pressure is increased.

However, the reason why the anomalies disappear at high P is different for each model. In the HCLR model the soft core ramp becomes ineffective at high pressures, and the particles start to behave like a liquid of simple hard spheres. This is not the case for the uncut ramp potential. As clustering sets in, more and more particles are being replaced by dimers. The interaction between the dimers and single particles has the same shape as the original particle-particle interaction (an uncut ramp), except that now the ramp is twice as steep. The result is that

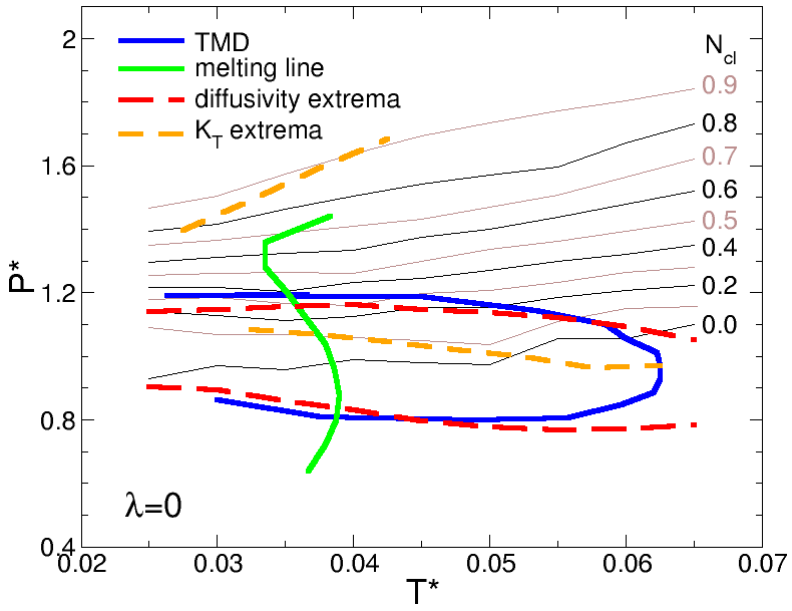

Figure 2.12: Phase diagram of the (uncut) ramp potential ($\lambda = 0$). The isoclustering lines shown refer to the liquid phase (simulated deep into the supercooled liquid region), and run from $N_{\rm cl} = 0.9$ at the top to $N_{\rm cl} = 0.0$ at the bottom in steps of 0.1 (thin black/brown lines). The green solid line is the melting line, which displays re-entrant melting where the slope dP/dT is negative. The blue solid line is the TMD, and the red dashed lines indicate the extrema in diffusivity. The loci of isothermal compressibility extrema are represented by the orange dashed lines. Axes are in reduced units: $P^* = P\,\sigma_1^3/U_1$ and $T^* = k_B\,T/U_1$.

the increase of clustering makes it harder for particles to climb up the ramp, and thus the anomalies disappear. When the pressure has been increased so much that $N_{\rm cl} \approx 1.0$, we are left with only dimers, and the anomalies are completely gone (see Fig. 2.12).

How do we resolve this with the principle of two competing length scales? For simple liquids, each particle has a preferred distance to its nearest neighbor. Within the anomalous region of the HCLR model, the nearest neighbor can be at one of two distances: $r \approx \sigma_1$ (at the foot of the ramp) or $r \approx \sigma_0$ (tightly against the hard core). We see that for the uncut ramp, the nearest neighbor can be either at $r \approx \sigma_1$ (at the foot of the ramp) or $r \approx 0$ (full overlap). In other words, also in the uncut

ramp model there are two competing length scales, namely $r \approx \sigma_1$ and $r \approx 0$.

Fig. 2.13 shows what happens when we cut the ramp at lower and lower heights. When $\lambda = 0.25$ the liquid still has all its anomalies, but the density anomaly region and the diffusion anomaly region have been considerably reduced in size. The same is true for the region with the compressibility anomaly. In addition to all of that, the part of the melting line that has a negative slope becomes more and more steep, and when $\lambda = 0.25$ the slope is nearly everywhere positive. When λ reaches a value of approximately $\lambda_c \approx 0.28$ the density anomaly has been reduced to a point in the phase diagram [107]. At very low cuts (such as $\lambda = 0.5$ in Fig. 2.13) all the anomalies, except for the compressibility anomaly, have disappeared.

It might seem strange that the cut ramp potential with $\lambda = 0.5$ has no anomalies apart from the compressibility. Clearly this potential has two length scales (the foot of the ramp at $r = \sigma_1$, and the location of the cut at r_{cut}), yet its phase diagram shows no density anomaly, no diffusion anomaly, and its melting line has a positive slope for all pressures.

Clearly, at low pressures the cut ramp potential is the same as the HCLR model and the uncut ramp. In this regime the particles only feel the foot of the ramp at $r = \sigma_1$, and all potentials are identical. Upon increasing the pressure, the particles will start to climb up the ramp. In the case of both HCLR and the uncut ramp, neighboring particles can now choose to be either at the foot of the ramp (low E, but high V) or at the top of the ramp (high E, but low V). The preferred state of the liquid is the one with the lowest Gibbs energy $G = E + PV - TS$. Hence, for a certain range of pressures and temperatures, both configurations (both length scales) have approximately the same Gibbs energy, and one could say that the two length scales are "competing".

In the case of the cut ramp potential, however, particles at the top of the ramp

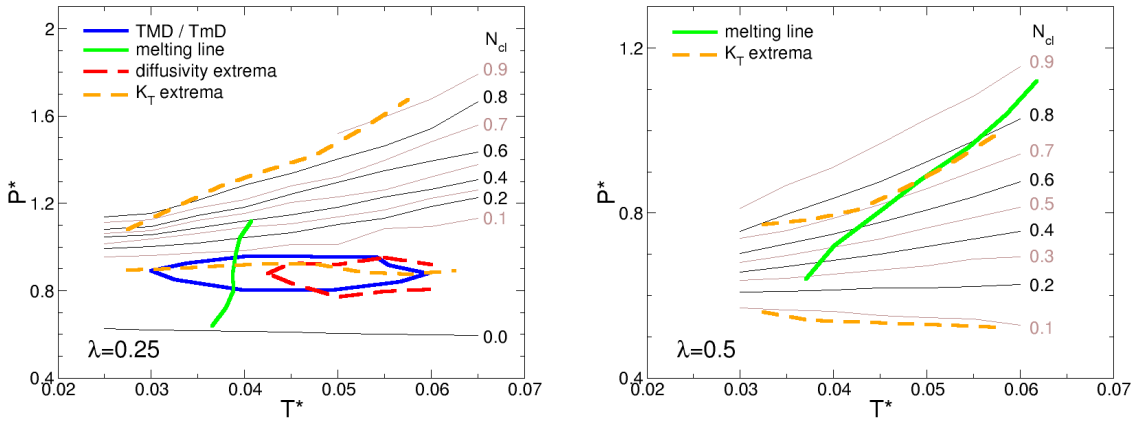

Figure 2.13: Phase diagram of the cut ramp potential for different cuts (left: $\lambda = 0.25$, right: $\lambda = 0.5$). The isoclustering lines shown refer to the liquid phase (simulated deep into the supercooled liquid region), and run from $N_{\rm cl} = 0.9$ at the top to $N_{\rm cl} = 0.0$ at the bottom in steps of 0.1 (thin black/brown lines). The line with $N_{\rm cl} = 0$ is omitted for $\lambda = 0.5$. The green solid line is the melting line, which displays re-entrant melting where the slope dP/dT is negative. The blue solid line is the TMD/TmD (enclosing the density anomaly), and the red dashed lines indicate the extrema in diffusivity. The loci of isothermal compressibility extrema are represented by the orange dashed lines. Axes are in reduced units: $P^* = P\,\sigma_1^3/U_1$ and $T^* = k_B\,T/U_1$. Note the difference in scale of the vertical axes. When $\lambda = 0.25$ (left panel) there is still a strong competition between the two length scales σ_1 and $\sigma_{\rm cut}$, and full overlap does not occur until the pressure goes above $P^* = 1.6$. This is similar to the uncut ramp of Fig. 2.12. When $\lambda = 0.5$ (right panel) the height of the top of the ramp is so low that there is no longer any competition, and moderate pressures already leads to full overlap (above the $N_{\rm cl} = 0.9$ line). All anomalies have disappeared, except the compressibility anomaly.

pay a small price in energy E, yet gain a large reduction in volume. This means that upon increasing the pressure of the liquid, particles immediately start to cluster, as full overlap has the lowest Gibbs energy and is the preferred state. This can also be seen in Fig. 2.13, where the isoclustering line of $N_{\rm cl} = 0.9$ (90% particle overlap) occurs already at much lower P for $\lambda = 0.5$ (right panel) than for $\lambda = 0.25$ (left panel).

In conclusion, the cut ramp potential does have two length scales, but if the height of the cut is too low there will be no competition between the two length

scales, and thus no anomalies. The compressibility anomaly does not seem to require this competition, however. The existence of a soft core (such as the ramp) is sufficient to allow for this anomaly to occur. This can also be seen in Figs. 2.12 and 2.13, where the compressibility anomaly region (bound by the K_T extrema) roughly coincides with the region where $0.1 \lesssim N_{\rm cl} \lesssim 0.9$ for all λ.

2.4.4 The clustering anomaly

The uncut ramp potential also displays two other anomalies, in addition to the density anomaly, diffusion anomaly, compressibility anomaly, and re-entrant melting. In Fig. 2.14 we present the density of the crystal compared to that of the liquid (both measured at the melting line). For $\lambda = 0.5$, and all pressures, we have the normal behavior that the crystal has a higher density than the liquid. The same is true for the uncut ramp potential ($\lambda = 0$), except within the range $P^* = 0.9$ to 1.3. This is the same common phenomenon as with water: the crystal floats on the liquid. We should note that this is not exactly the same anomaly as the density anomaly, because the density anomaly is purely a property of the liquid, and is unrelated to the solid state (see its definition in Sec. 1.2.1).

The range of pressures where the crystal has a lower density than the liquid, corresponds exactly to the range where the melting line of the uncut ramp potential has a negative slope (see Fig. 2.13). This should come as no surprise, since we have already seen in Sec. 1.2.4 that the Clapeyron relation (Eq. 1.8) dictates that the slope of the melting line dP/dT should be negative when $\Delta V = V_{\rm liquid} - V_{\rm crystal} < 0$, because the change in entropy $\Delta S = S_{\rm liquid} - S_{\rm crystal}$ is always positive (the liquid is always more disordered than the crystal).

In Fig. 2.15 we compare the amount of clustering $N_{\rm cl}$ in the liquid vs. the crystal. We see that in all cases the particles in the crystal have more overlap than those in

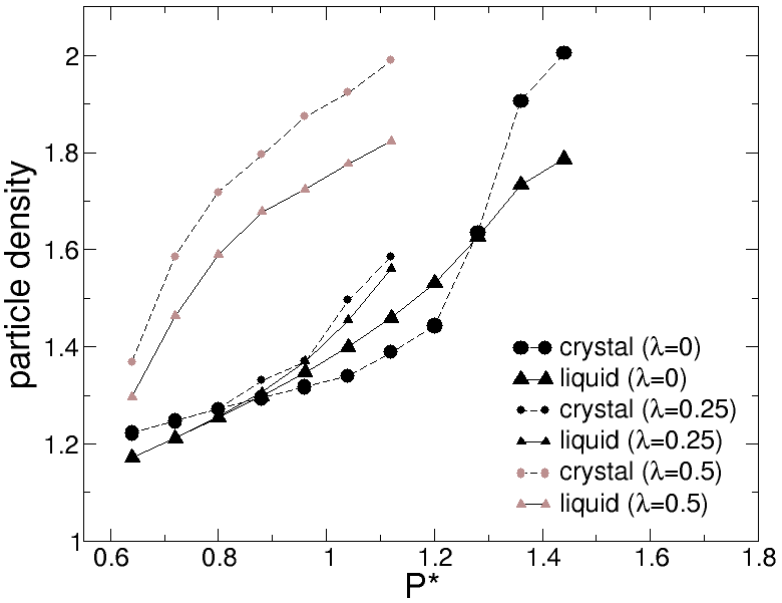

Figure 2.14: Particle density of the crystal and liquid on the melting line, for the cut ramp potential with $\lambda = 0$, 0.25, and 0.5. For P^* roughly between 0.9 and 1.3, and $\lambda = 0$, the liquid phase is more dense than the coexisting solid.

the liquid, except for $\lambda = 0$ where there is a region with a "clustering anomaly". This anomalous region corresponds roughly to the same pressure range as the anomaly in Fig. 2.14. Since an increase in clustering automatically leads to an increase in density, it is clear that for this potential the clustering anomaly is responsible for why the crystal floats on the liquid.

2.5 Conclusion

In this chapter we have considered a variety of simple models in an attempt to understand why certain liquids have water-like anomalies such as the density anomaly and the diffusion anomaly. We have seen that these anomalies can be caused by different effects. For water most anomalies can be explained with the hydrogen bonds, while for the simple models discussed in this chapter a soft repulsive core is the direct cause of the anomalies. Although different effects are causing these

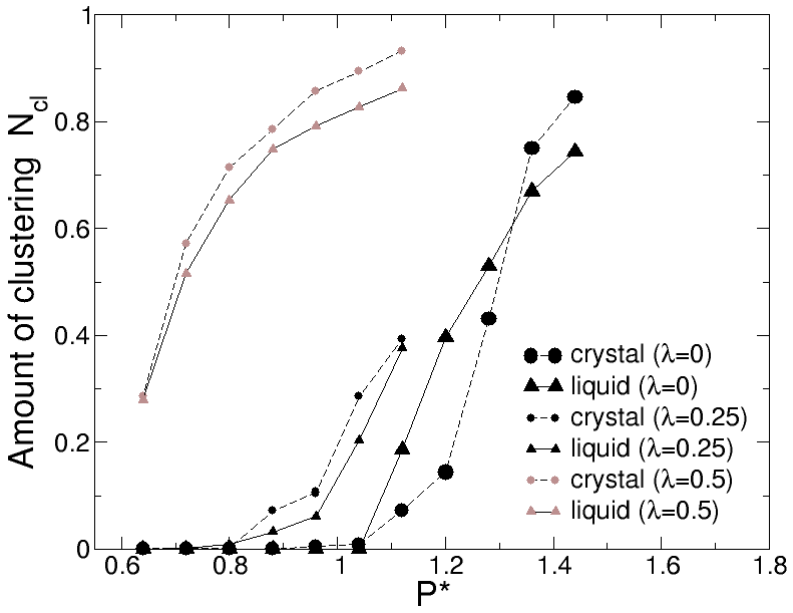

Figure 2.15: Average number of neighbors $N_{\rm cl}$ within a distance smaller than the first minimum of $g(r)$ (see Eq. (2.5)). Results are shown for temperatures on the melding line (both the liquid and solid state) for the cut ramp potential with $\lambda = 0$, 0.25, and 0.5. In most cases the clustering is higher for the solid state, except for $\lambda = 0$ in the pressure range corresponding to the anomalous region.

anomalies, all lead to the same general mechanism: the existence of two competing length scales.

Which two length scales are competing is not always immediately clear, even in simple models. In Sec. 2.4.3, for example, we found that it is possible to have one length scale being $r = 0$ (in the case of clustering with a bounded potential). Furthermore, it is important that the two length scales are actually *competing*, and that e.g. a small change in pressure does not immediately lead to a large change in structure (as in the case of the cut ramp potential with $\lambda = 0.5$ in Sec. 2.4.3).

The anomalies seem to be independent of the existence of a liquid-liquid phase transition (LLPT). Some models have the anomalies but no LLPT (such as the hard core linear ramp model in Sec. 2.2), while others models have both (e.g. the Jagla potential in Sec. 2.3).

Likewise, a LLPT can occur without anomalies, depending on the nature of the soft-core repulsion. For example, a simple model with a soft repulsion that consists of a square shoulder shows no anomalies but does have a LLPT for certain parameter values [56, 57, 16]. The possibility that a LLPT may occur disjointed from anomalies was recently supported by the experimental study of triphenyl phosphite, where in association with the LLPT the heat capacity shows no anomalous behavior [203] and a density increase is expected upon cooling.

It is often hard to establish if a liquid has a LLCP, even with computer simulations. In the next two chapters several techniques will be discussed, using liquid water and liquid silica as an example.

CHAPTER 3: Liquid-liquid critical point in ST2 water

We've learned from experience that the truth will come out. Other experimenters will repeat your experiment and find out whether you were wrong or right. Nature's phenomena will agree or they'll disagree with your theory. And, although you may gain some temporary fame and excitement, you will not gain a good reputation as a scientist if you haven't tried to be very careful in this kind of work.

– Richard. P. Feynman, in *Surely You're Joking, Mr. Feynman!*

3.1 Introduction

Simple models are an important tool to obtain a good understanding of the behavior of liquids, but if one wishes to make theoretical predictions of a real liquid, it is often necessary to use a model that describes that liquid as accurately as possible. On the other hand, a higher accuracy usually means a more demanding calculation, which leads to a slower or smaller simulation. To make matters worse, different models might be better at describing different phenomena. For example, model A might be able to reproduce the melting line very well, but might give the wrong boiling temperature. Model B might be exactly the opposite, and only reproduces the boiling temperature well. Clearly, an investigation of e.g. crystal nucleation would yield better results if model A was used to do the simulations. It is important to choose a model depending on the phenomena one is interested in, and to not forget the strengths and weaknesses of that particular model.

In this chapter we present an analysis of the liquid-liquid critical point in ST2. This is quite an old water model (and much "better" models are available nowadays),

but it is believed to have a liquid-liquid critical point (LLCP) that is not too hard to access with molecular dynamics. For this reason, it is the model of choice if one wants to study the liquid-liquid phase transition (LLPT).

The results of this chapter indicate that the ST2 water model indeed has a LLPT ending in a LLCP, which separates two metastable liquids of different densities. However, the fact that ST2 has such a critical point, does not necessarily mean that there is one in real water—that is a matter that can only be fully resolved by experiments. Fortunately, to echo the words of Richard Feynman, we may be confident that one day the truth will come out.

3.2 Overview of the LLCP in ST2 water

For many centuries, water and its anomalies have been of much interest to scientists. A particular rise of interest occurred in the late 1970s after experiments done by Angell and Speedy seemed to imply some kind of critical phenomenon in supercooled liquid water at very low temperatures [13, 183, 14, 182]. Even though liquid water experiments are limited by spontaneous crystallization below the homogeneous nucleation temperature ($T_H \approx 233$ K at 1 bar), it is possible to further explore the phase diagram by quenching water to far lower temperatures [31, 27, 127]. The result of these experiments is an amorphous solid, i.e. a glassy ice, corresponding to an out-of-equilibrium state that is very stable with respect to the equilibrium crystalline ice phase. The type of amorphous solid depends on the applied pressure: at low pressure, below ≈ 0.2 GPa, the low density amorphous ice (LDA) is formed, while at higher pressure the high density amorphous ice (HDA) is observed [115]. It has been shown by Mishima *et al.* that these two amorphous ices are separated by a reversible abrupt change in density that resembles in all its respects an equilibrium

first order phase transition [128, 126, 129, 130].

Raising the temperature of either LDA or HDA does not turn the sample into a liquid, but leads once again to spontaneous crystallization (around $T_X \approx 150$ K). In fact, between T_H and T_X, often called the "no man's land" of bulk water, crystallization occurs at a time scale that is too short for current experimental methods, although a new technique is possibly succeeding in the task of measuring the metastable liquid phase [136]. Computer simulations of water, however, involve time scales small enough to witness spontaneous crystallization and are therefore able to explore liquid water in the "no man's land". In 1992 Poole *et al.* [152] performed a series of molecular dynamics simulations using the ST2 water model [194], using the reaction field method for the long-range interactions (ST2-RF), and discovered a liquid-liquid phase transition ending in a critical point, separating a low density liquid (LDL) and a high density liquid (HDL). These two liquids can be considered to be the liquid counterparts of the LDA and HDA, respectively.

The existence of the critical point also allows one to understand X-ray spectroscopy results [205, 84, 137, 214], explains the increasing correlation length in bulk water upon cooling as found experimentally [83], the hysteresis effects [230], and the dynamic behavior of protein hydration water [120, 52, 21]. It would be consistent with a range of thermodynamical and dynamical anomalies [102, 172, 188, 101, 100, 59, 163, 164, 121] and experiments [49, 187, 185, 186].

Many more computer simulations investigating the phenomenology of the liquid-liquid critical point (LLCP) have been performed since then [67, 56, 58, 51, 81, 184, 141, 122, 55, 197, 43, 210, 211, 221, 62, 199, 200, 20]. Detailed studies using ST2-RF have been made by Poole *et al.* [151] using molecular dynamics, while Liu *et al.* simulated ST2 with Ewald summation (ST2-Ew) for the electrostatic long-range potential using Monte Carlo [113, 114]. Also in other water models the liquid-liquid

phase transition (LLPT) and its LLCP are believed to be found, for example by Yamada *et al.* in the TIP5P model [224], by Paschek *et al.* in the TIP4P-Ew model [144], and in TIP4P/2005 by Abascal and Vega [2, 3].

In 2011 Limmer and Chandler used Monte Carlo umbrella sampling to investigate the ST2-Ew model, but claimed to have found only one liquid metastable phase (HDL) rather than two [110, 111]. They therefore concluded that LDL does not exist because it is unstable with respect to either the crystal or the HDL phase. The emphasis in their work is about the difference between a metastable phase, i.e. separated from the stable phase by a finite free-energy barrier, and an unstable state, where the free-energy barrier is absent and the state does not belong to a different phase.

Shortly after, Poole *et al.* [148] and Kesselring *et al.* [96] presented results using standard molecular dynamics for ST2-RF showing the occurrence of the LLCP with both HDL and LDL phases metastable with respect to the crystal, and not unstable. This result was confirmed, using the same method as Limmer and Chandler, by Sciortino *et al.* [173] and Poole *et al.* [149] in ST2-RF water and by Liu *el al.* in ST2-Ew water [112].

In this chapter we investigate the possible existence of a liquid-liquid critical point in simulated water in the thermodynamic limit using finite-size scaling techniques, and confirm that LDL is a *bona fide* metastable liquid. We use the ST2-RF model because it has been well-studied in the supercooled region, making it easier to compare and verify our data. In the supercooled phase it has a relatively large self-diffusion compared to other water models, and therefore suffers less from the slowing down of the dynamics at extremely low temperatures. We explore a large region of the phase diagram of supercooled liquid ST2-RF water (Fig. 3.1) using molecular dynamics simulations with four different system sizes by keeping

constant the number N of molecules, the pressure P and the temperature T (NPT ensemble).

Within the explored region we find both LDL and HDL, separated at high pressures by a LLPT, ending in a LLCP estimated at $P_C \approx 208$ MPa and $T_C \approx 246$ K. This phase transition is particularly clear in Fig. 3.2 where one can see from the density how the system continuously flips between the two states. However, due to finite-size effects this phase flipping also occurs below the critical point along the Widom line (the locus of correlation length maxima) [222, 60]. For this reason it is necessary to apply finite-size scaling methods to establish the exact location of the critical point.

For six state points and for small system size $N \leq 343$ we observe, in only one over the (on average) seven simulations we performed for each state point, irreversible crystal growth, indicated as full red circles in Fig. 3.1. Each of these crystallization events occurred within the LDL (or LDL-like) region. Analysis of these crystals revealed them to have a diamond cubic crystal structure. As we will discuss later, because these events disappears for larger systems, we ascribe these crystallization to finite-size effects.

We start in Sec. 3.3 with a description of the model and the procedures that were used. In Sec. 3.4 we discuss the use of the intermediate scattering function to analyze the structure of the liquid, and in Sec. 3.5 its use in defining the correlation time. The analysis of the liquid structure is continued in Sec. 3.6 where we define and compare a selection of structural parameters. The parameter d_3 is found to be particularly well-suited to distinguish between the liquid and the crystal state, and this fact is subsequently used in Sec. 3.7 where we discuss the growth and melting of crystals within the LDL liquid. In Sec. 3.8, by defining the appropriate order parameter, we show that the LLCP in ST2-RF belongs to the same universality

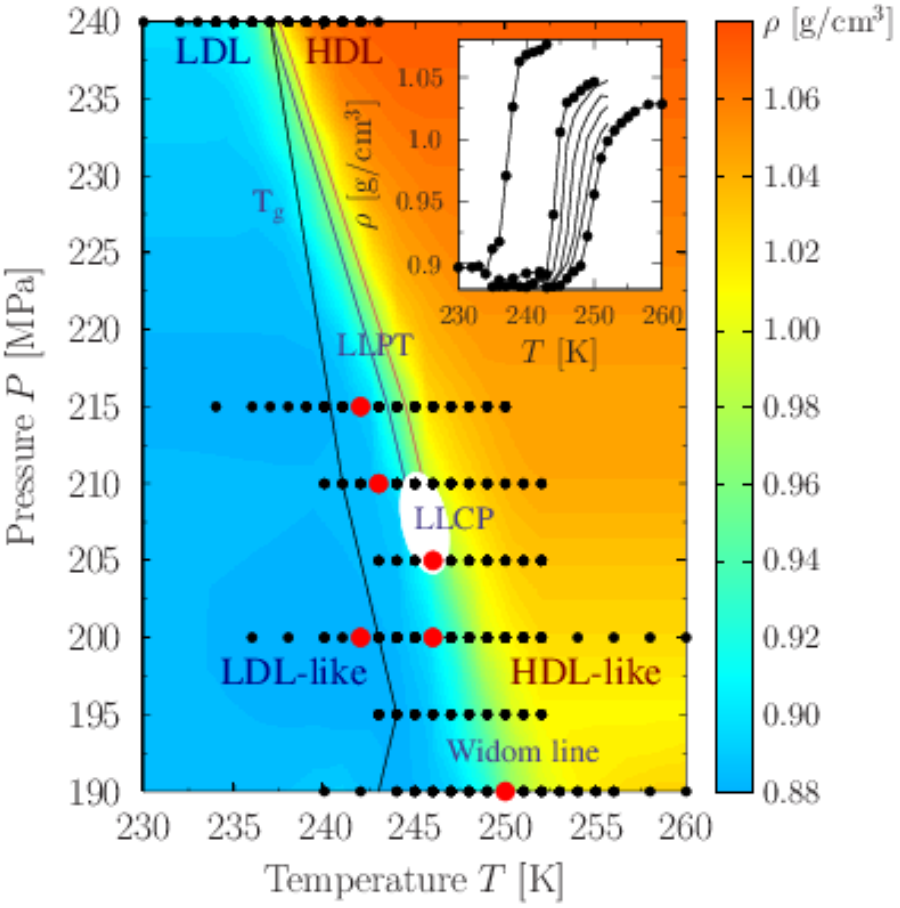

Figure 3.1: Overview of the state points at which simulations have been performed. Colors away from the simulated points (full black circles) are a linear interpolation of ρ for the sake of presentation. At high temperatures we observe a high-density liquid state (HDL, shaded in orange), while at lower temperatures we find a low-density liquid (LDL, in blue). These are separated by a region where the system is continuously flipping between the two states, as seen in Fig. 3.2. This transition region (in yellow/green) is identified as the liquid-liquid phase transition line (LLPT) at high pressures, and the Widom line at low pressures. These lines join at the liquid-liquid critical point (LLCP) estimated at $P_C = 208 \pm 3$ MPa and $T_C = 246 \pm 1$ K (see Sec. 3.8). At low temperatures the LDL (or LDL-like) region is bounded by the glass transition temperature T_g, below which we can no longer fully equilibrate the system within 100 ns, and consider the liquid to have become a glass (see Sec. 3.5). For small sizes ($N \leq 343$) we observe spontaneous crystallization within 1 ns-long simulations at six state points (indicated by the red circles), all of them within the LDL (or LDL-like) region. Inset: Average $\rho(T)$ for pressures $P = 240$ MPa (left-most), 215, 210, 205, 200, 195, and 190 (right-most). Here the average is taken over all N; excluding $N \leq 343$ shows a much sharper transition at 240 MPa.

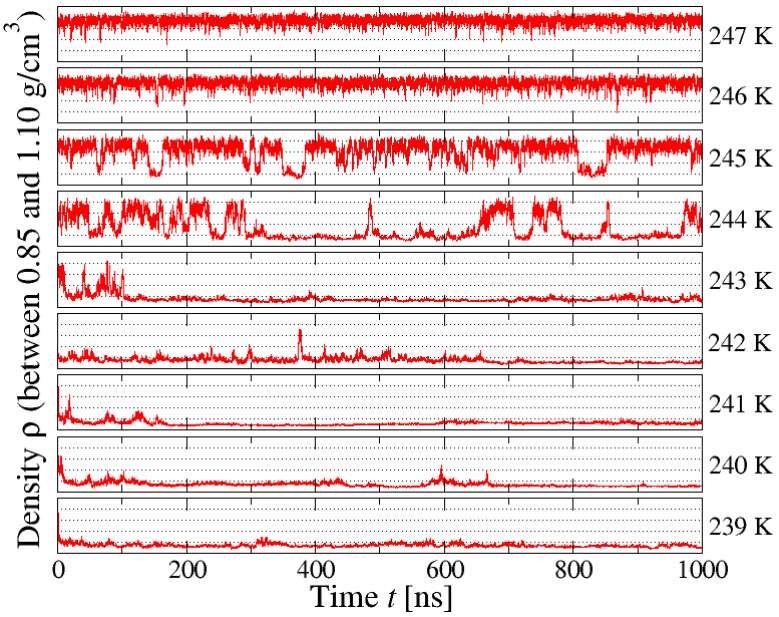

Figure 3.2: Phase flipping near the phase transition line ($P = 215$ MPa, with $N = 343$ molecules). At high T the system is in the HDL phase (with a density $\rho \simeq 1.03$ g/cm^3), while at low T the system is in the LDL phase (density $\rho \simeq 0.88$ g/cm^3). However, near the phase transition line (at $T \simeq 244.5$ K for this pressure) the system is flipping between the two phases.

class as the 3D Ising model. We accurately determine where the LLCP is located in the phase diagram in the thermodynamic limit by applying finite-size scaling on the Challa-Landau-Binder parameter. We discuss our results and present our conclusions in Sec. 3.9.

3.3 Simulation details

In the ST2 model [194] each water molecule is represented by a rigid tetrahedral structure of five particles. The central particle carries no charge and represents the oxygen atom of water. It interacts with all other oxygen atoms via a Lennard-Jones (LJ) potential, $U_{\rm LJ}(r_{ij}) \equiv 4\varepsilon\left[(\sigma/r_{ij})^{12} - (\sigma/r_{ij})^{6}\right]$ with $\varepsilon \equiv 0.31694$ kJ/mol and $\sigma \equiv 3.10$ Å. Two of the outer particles represent the hydrogen atoms. Each of them

carries a charge of +0.2357 e, and is located a distance 1 Å away from the central oxygen atom. The two remaining particles carry a negative charge of −0.2357 e, are positioned 0.8 Å from the oxygen, and represent the lone pairs of a water molecule.

The electrostatic potential in ST2 is treated in a special way. To prevent charges a and b from overlapping, the Coulomb potential is reduced to zero at small distances:

$$U_{\mathrm{el}}(r_{ab}) \equiv S(r_{ij}) \frac{1}{4\pi\epsilon_0} \frac{q_a q_b}{r_{ab}} \tag{3.1}$$

where $S(r_{ij})$ is a function that smoothly changes from one to zero as the distance between the molecules decreases,

$$S(r_{ij}) \equiv \begin{cases} 0 & (r_{ij} \leq R_L) \\ \frac{(r_{ij}-R_L)^2(3R_U-R_L-2r_{ij})}{(R_U-R_L)^3} & (R_L \leq r_{ij} \leq R_U) \\ 1 & (r_{ij} \geq R_U) \end{cases} \tag{3.2}$$

with $R_L \equiv 2.0160$ Å, $R_U \equiv 3.1287$ Å, and where r_{ij} is the distance between the oxygen atoms of the interacting molecules. In the original model a simple cutoff was used for the electrostatic interactions. In this thesis, however, we apply the reaction field method [192] which changes the ST2 Coulomb potential to

$$U_{\mathrm{el}}(r_{ab}) \equiv S(r_{ij}) T(r_{ij}) \frac{q_a q_b}{4\pi\epsilon_0} \left(\frac{1}{r_{ab}} + \frac{r_{ab}^2}{2R_c^3} \right) \tag{3.3}$$

where $T(r_{ij})$ is another smoothing function:

$$T(r_{ij}) \equiv \begin{cases} 1 & (r_{ij} \leq R_T) \\ 1 - \frac{(r_{ij}-R_T)^2(3R_c-R_T-2r_{ij})}{(R_c-R_T)^3} & (R_T \leq r_{ij} \leq R_c) \\ 0 & (r_{ij} \geq R_c). \end{cases} \tag{3.4}$$

We use a reaction field cutoff $R_c \equiv 7.8$ Å together with $R_T \equiv 0.95R_c$. These parameters define our ST2-RF water model and are the same that were used in previous ST2-RF simulations.

For the LJ interaction we use a simple cutoff at the same distance of 7.8 Å. We do not adjust the pressure to correct for the effects of the LJ cutoff [80, 4], since these adjustments come from mean field calculations which become increasingly unreliable as one approaches a critical point. In order to facilitate comparing results with and without this correction, we denote that for LDL ($\rho \approx 0.90$ g/cm^3) the correction is $P \approx -15$ MPa, and for HDL ($\rho \approx 1.05$ g/cm^3) the correction is $P \approx -20$ MPa.

We use the SHAKE algorithm [156] to keep the relative position of each particle within a ST2 molecule fixed. The temperature and pressure are held constant using a Nosé-Hoover thermostat [138, 4, 139] together with a Berendsen barostat [18]. In all simulations periodic boundary conditions are applied.

Our code is validated by simulating the same state points as those published by Poole *et al.*, see Fig. 1b in [151], where pressure corrections for the LJ cutoff were applied in the NVT (constant N, T and volume V) ensemble. Averaging at each state point over 10 simulations with different initial conditions allows us to estimate the error bars. In Fig. 3.3 we compare our results for $N = 216$ molecules and density 0.83 g/cm^3, and find that our data, after pressure correction, matches that of Ref. [151] well.

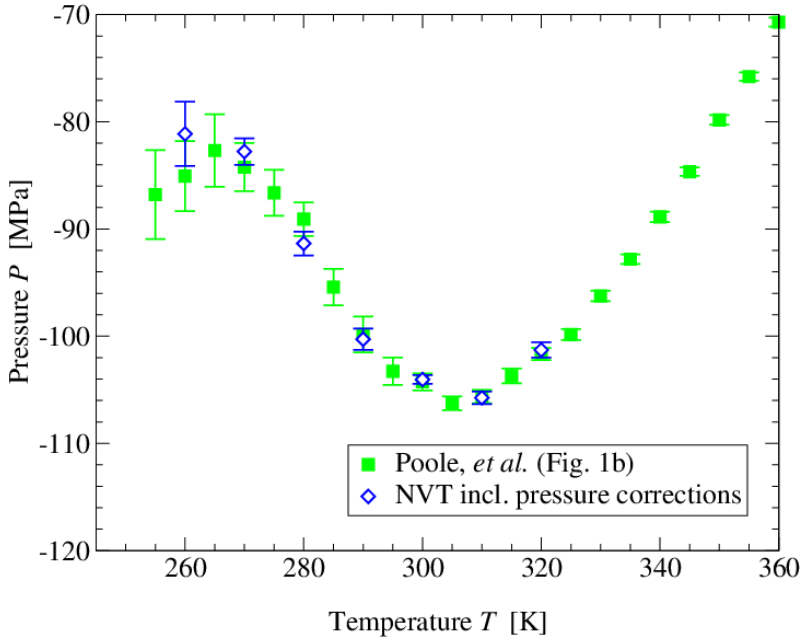

Figure 3.3: To validate our code, we compare our simulation results with those from Poole *et al.* [151] at density $\rho = 0.83$ g/cm^3 and for $N = 216$ molecules. We performed simulations in the NVT ensemble applying pressure corrections and find the same results as Ref. [151] within the error bars (standard error calculated from a set of 10 runs at each state point). At this density the pressure correction due to the LJ cutoff (proportional to ρ^2) is equal to -12.66 MPa. The variation of P with T along this isochore shows the occurrence of both a density maximum at 305 K and a density minimum near 265 K, as at these state points $(\partial\rho/\partial T)_P = -\rho K_T(\partial P/\partial T)_V = 0$ with $K_T > 0$ the isothermal compressibility.

For each of the simulations done in the NPT ensemble, we use the following protocol. We first create a box of N molecules at n different initial densities (with n up to 21) ranging from 0.85 to 1.05 g/cm^3. We then perform a 1 ns NVT simulation at $T = 300$ K. In this way we obtain n independent configurations all at $T = 300$ K in the prefixed range of densities. Next, we use these independent configurations as starting points for NPT simulations at $T = 265$ K and different pressures ranging from 190 to 240 MPa, and continue the simulation for an additional 1 ns. This results in n independent configurations at $T = 265$ K and the given pressure. For all pressures considered here, this will lead the system into the HDL phase. Finally

the system is quenched to the desired temperature at the given pressure, followed by 100–200 ns of equilibration time. In Sec. 3.5 it will be shown that this provides enough time for the system to reach equilibrium for the state points above the line marked with the label T_g in Fig. 3.1.

3.4 Intermediate scattering function

The intermediate scattering function $S(\mathbf{k}, t)$ plays an essential role in the analysis of liquid structure, since it is frequently measured in experiments as well as easily calculated from simulation data. It describes the time evolution of the spatial correlation at the wave vector $\mathbf{k}$, and can be used to distinguish between phases of different structure, such as LDL and HDL or crystal. It is defined as

$$S(\mathbf{k}, t) \equiv \frac{1}{N} \left\langle \sum_{\ell,m}^{N} e^{i\mathbf{k}\cdot[\mathbf{r}_\ell(t') - \mathbf{r}_m(t'+t)]} \right\rangle_{t'}$$

where $\langle ... \rangle_{t'}$ denotes averaging over simulation time t', and $\mathbf{r}_\ell(t')$ the position of particle ℓ at time t'. For simplicity we only apply the intermediate scattering function to the oxygen atoms, which we denote as $S_{OO}(k, t)$.

Since the system has periodic boundary conditions, the components of $\mathbf{k}$ have discrete values $2\pi n/L$, where L is the length of the simulation box and $n = 1, 2, 3, \ldots$. We define $S_{OO}(k, t) \equiv \langle S_{OO}(\mathbf{k}, t) \rangle_n$ where the average is taken over all vectors $\mathbf{k}$ with magnitude k belonging to the nth spherical bin $\pi(n - \frac{1}{2})/L \leq k < \pi(n + \frac{1}{2})/L$ for $n = 2, 3, \ldots, 300$. Similarly, we define the structure factor $S_{OO}(k) \equiv \langle S_{OO}(k, t) \rangle_t$ as the time-averaged intermediate scattering function, with (unless indicated otherwise) the average taken over the whole duration of the run.

We study $S_{OO}(k)$ above and below our estimate for the LLCP pressure. At $P = 210$ MPa $> P_C$ (Fig. 3.4a,b) we observe a discontinuous change in the first

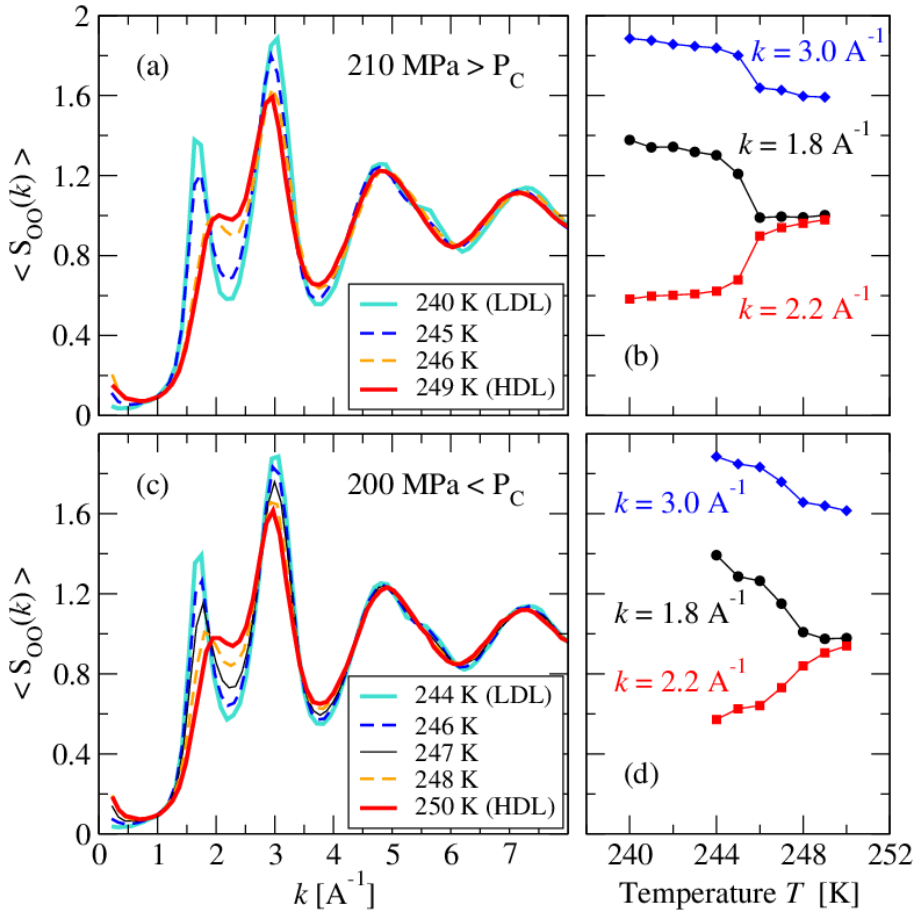

Figure 3.4: The structure factor $S_{OO}(k)$ for a range of temperatures at (a) 210 MPa and (c) 200 MPa for $N = 729$. (a) For $P > P_C$ the structure has a large change between $T = 245$ and 246 K, corresponding to the LDL-HDL first-order phase transition. (b) The value of S_{OO} for k corresponding to the first maximum, the first minimum and the second maximum as a function of T for $P = 210$ MPa as in panel (a). (c) For $P < P_C$ the structure changes in a way that is smoother than the case in panel (a), with the more evident change occurring between $T = 249$ and 250 K, corresponding to the crossing of the Widom line, as marked by the value of S_{OO} at first maxima and minima in panel (d).

two peaks of $S_{OO}(k)$ as T changes between 245 and 246 K, and a continuous change above and below this temperatures. This is the expected behavior for a first order phase transition occurring at 245 K$\lesssim T \lesssim$ 246 K and $P = 210$ MPa between two phases with different structure, consistent with our results in Fig. 3.1. The fact that for both phases $S_{OO}(k) \sim O(1)$ for all k shows that both phases are fluid. Indeed,

for a crystal-like configuration, with a long-range order, there would be at least one wave vector such that $S_{OO}(k) \sim O(N)$ [57]. Furthermore, the fact that at lower T the first peak increases and the other peaks only have minor changes indicates that the lower-T liquid has a smaller density than the higher-T liquid. Therefore, this result show a first-order phase transition between the LDL at lower-T and HDL at higher-T. This transition occurs at the same temperature at which we observe the phase flipping in density (Fig. 3.2) and corresponds to the yellow/green region at $P > P_C$ in Fig. 3.1.

The fact that the peaks of $S_{OO}(k)$ are sharper in LDL than HDL is an indication that the LDL phase is more structured. We can also observe that the major structural changes in $S_{OO}(k)$ between LDL and HDL are for $k \simeq 1.8$ and 2.8 Å^{-1}, corresponding to $r = 4\pi/k \simeq 7$ and 4.5 Å, respectively, i.e. the third and the second neighbor water molecules. This change in the structure is consistent with a marked shift inwards of the second shell of water with increased density, and almost no change in the first shell (at $k \simeq 4.6$ Å^{-1} and $r \simeq 2.75$ Å), as seen in structural experimental data for supercooled heavy water interpreted with Reverse Monte Carlo method [179]. These changes are visible also in the OO radial distribution function $g_{OO}(r)$.

For $P < P_C$ (Fig. 3.4c,d) by increasing T we observe that the first peak of $S_{OO}(k)$ merges with the second, transforming continuously into a shoulder (the same qualitative behavior can be observed for $g_{OO}(r)$). These quantities show us also that the lower-T structure is LDL-like, while the higher-T structure is HDL-like. However, the absence of any discontinuous change in the structure implies the absence of a first-order phase transition in the structure of the liquid. This is consistent with the occurrence of a LLCP at the end of the first-order phase transition somewhere between 200 and 210 MPa, at a temperature between 245 and

250 K. In Sec. 3.8 we shall apply a different method to locate the LLCP with more precision.

At $P < P_C$, in the one-phase region, we expect to find the Widom line emanating from the LLCP. The Widom line is by definition the locus of maxima of the correlation length, therefore, from general thermodynamic considerations [60] near the LLCP, it must be also the locus of maxima of the response functions [106]. In particular, it must be the locus where the isobaric heat capacity $C_P \equiv T(\partial S/\partial T)_P$, where S is the entropy of the system, has its maximum along a constant-P path. This maximum occurs where the entropy variation with T is a maximum, and is expected where the structural variation of the liquid is a maximum, i.e. where the derivatives of the values of $S_{OO}(k)$ (Fig. 3.4d) and $g_{OO}(r)$ with T are at a maximum. The interval of temperatures for each P where this occurs corresponds to the yellow/green region at $P < P_C$ in Fig. 3.1, indicated as the Widom line.

It is actually possible to follow the structural changes during the simulation. An example is given in Fig. 3.5 where we focus on a 30 ns time period of a simulation at 200 MPa and 248 K. We divide this time period into six 5 ns intervals and for each interval we calculate the intermediate scattering function, time-averaged over those 5 ns. We observe that the liquid is LDL-like for the first and third interval, having low density and LDL-like $S_{OO}(k)$ (first peak near 2 Å^{-1}, separated from the second). On the contrary, for the fifth and sixth interval the density is high and $S_{OO}(k)$ is HDL-like (the first peak is merely a shoulder of the second peak), indicating that the liquid is HDL-like. For the second and fourth interval, the liquid has an intermediate values of density and $S_{OO}(k)$, indicating that it is a mix of LDL-like and HDL-like structures.

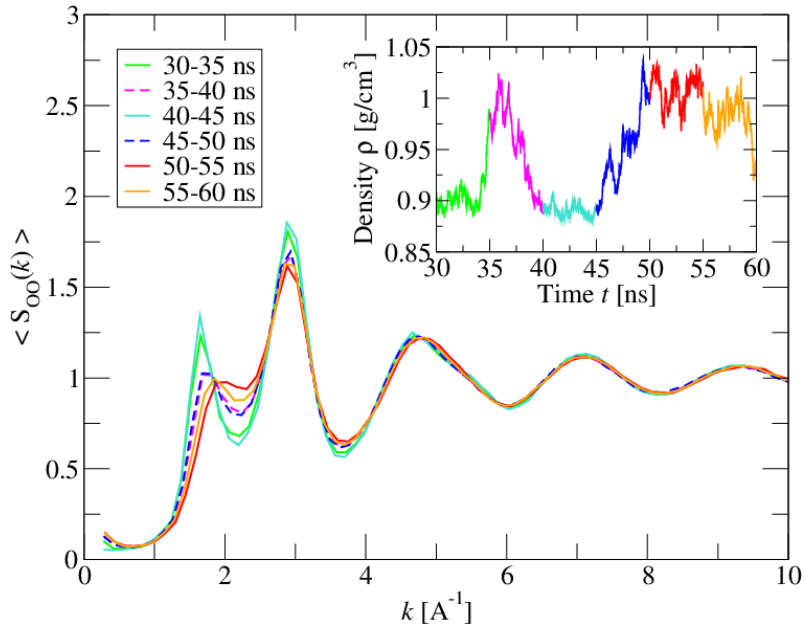

Figure 3.5: As the density changes from ρ(LDL) to ρ(HDL), also the structure changes. The inset shows how the density is changing with time for six consecutive time intervals of 10 ns, with the corresponding $S_{OO}(k)$ shown in the main plot ($N = 343$ at 200 MPa and 248 K).

3.5 Correlation time

Apart from its use in structure analysis, the intermediate scattering function $S_{OO}(k,t)$ can also be used to define a correlation time τ, i.e. the time it takes for a system to lose most of its memory about its initial configuration [190, 99].

In Fig. 3.6 we show how $S_{OO}(k,t)$ decays with time for a fixed value of k. Its decay is characterized by two relaxation times, the α-relaxation time τ_α and the β-relaxation time τ_β. On very short time scales, the molecules do not move around much and each molecule is essentially stuck in a cage formed by its neighbors. This is represented by the β-relaxation time τ_β which is on the order of picoseconds. On longer time scales, the molecule can escape from its cage and diffuse away from its initial position. The time τ_α is the relaxation time of this structural process.

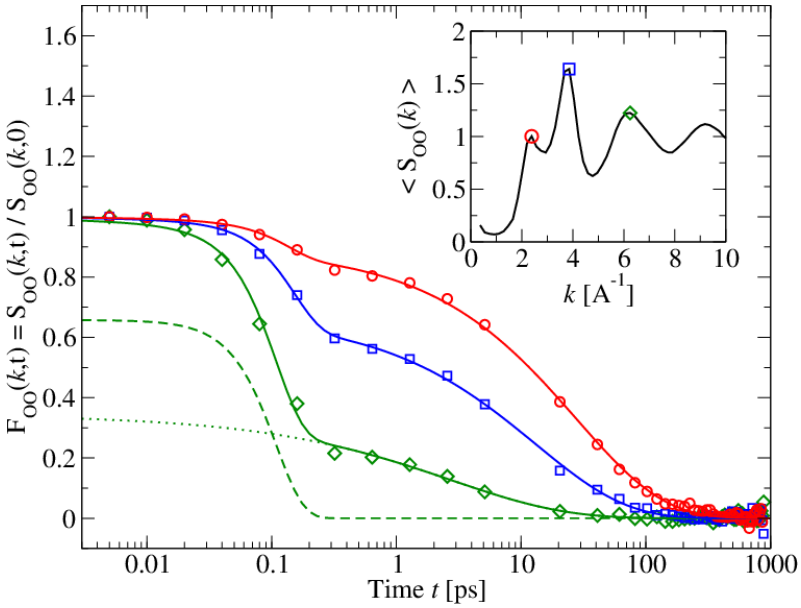

Figure 3.6: Decay of $S_{OO}(k,t)$ with time, for $P = 210$ MPa, $T = 250$ K and $N = 343$. Symbols indicate $F_{OO}(k_i,t)$ for three different values of k: the first maximum of $S_{OO}(k)$ at k_1 (red circles), the second maximum at k_2 (blue squares), and the third maximum k_3 (green diamonds). Solid lines are fits according to Eq. (3.5). The two components of Eq. (3.5) are explicitly shown for $F_{OO}(k_3,t)$: the green dashed line represents the β-relaxation and is given by $[1 - A(k)]\exp[-(t/\tau_\beta)^2]$, the green dotted line represents the α-relaxation and satisfies $A(k)\exp[-(t/\tau_\alpha)^b]$. The solid green line going through $F_{OO}(k_3,t)$ is the sum of both.

Mode-coupling theory of supercooled simple liquids predicts that [63]

$$\begin{aligned} F_{OO}(k,t) &\equiv S_{OO}(k,t)/S_{OO}(k,0) \\ &= [1 - A(k)]\, e^{-(t/\tau_\beta)^2} + A(k)\, e^{-(t/\tau_\alpha)^b} \end{aligned} \tag{3.5}$$

The factor $A(k)$ is the Debye-Waller factor arising from the cage effect, which is independent of the temperature and follows $A(k) = \exp(-a^2k^2/3)$ with a the radius of the cage. We are able to fit Eq. (3.5) remarkably well to all our data, as for example in Fig. 3.6.

Data in Fig. 3.6 was collected every 10 fs for simulations of 1 ns. This rate of

sampling results in a large amounts of data and is unfeasible for our runs up to 1000 ns. Therefore, for the 1000 ns runs we collect data at 10 ps intervals. At this rate of sampling it is no longer possible to estimate τ_β or the cage size a, but it is still possible to determine τ_α accurately, utilizing the fact that $S_{OO}(k,t)$ reaches a plateau near $t \approx \tau_\beta$. One can therefore define

$$C_{OO}(k,t) \equiv S_{OO}(k,t)/S_{OO}(k,\tau_\beta), \tag{3.6}$$

which is $S(k,t)$ normalized by its value at the plateau. A good estimate of τ_α is then the time for which $C_{OO}(k,\tau_\alpha) = 1/e \approx 0.37$.

From the shorter 1 ns runs (which were mostly done in the HDL regime) we find that the cage radius is $a = 0.35 \pm 0.09$ Å with a stretching exponent of $b = 0.63 \pm 0.09$. Both parameters a and b do not show a significant dependence on the state point within the studied range of temperatures and pressures. As shown in Fig. 3.6, different k result in slightly different values for τ_α. We use as the correlation time τ the largest value of τ_α which is usually found at $k = k_1$, the first maximum in $\langle S_{OO}(k) \rangle$ (inset Fig. 3.6). As is to be expected, the correlation time does not seem to depend on the box size. It does however depend strongly on the phase, which is evident from Fig. 3.7.

At high temperatures the system is in the HDL phase, and has a correlation time τ on the order of 10–100 ps. As we decrease the temperature at fixed pressure, the value of τ has a large increase when we cross the phase transition line or the Widom line, depending on if P is above or below P_C, respectively. Apparently, the LDL states evolve nearly four orders of magnitude slower than HDL states, with correlation times in the nanosecond range.

If we lower the temperature further, the correlation time slowly increases until

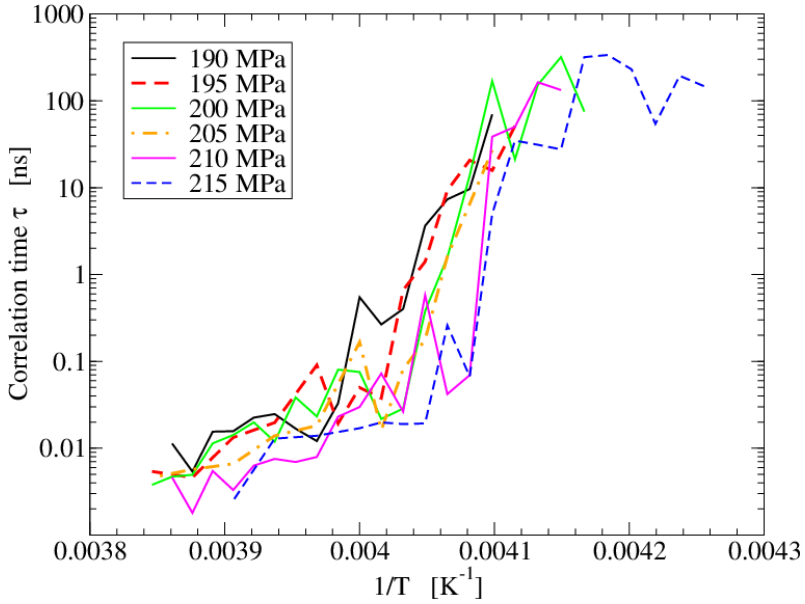

Figure 3.7: Arrhenius plot of the correlation time τ for different pressures. Errors on our estimates are of the order of the discontinuities along the curves. At high temperatures (the HDL regime) the correlation time is of the order of 10–100 ps, which jumps several orders up as we pass the phase transition line and enter the LDL regime. To obtain this plot, we dismissed the simulations that had a significant increase in τ because of crystal growth (see Sec. 3.7).

the system becomes a glass rather than a liquid, and we are no longer able to fully equilibrate the system. As we can only run simulations up to 1000 ns, we consider the state points with a correlation time above 100 ns to be beyond our reach. We therefore designate the effective glass transition temperature T_g as the temperature for which $\tau > 100$ ns (see Fig. 3.1).

3.6 Structural parameters

Apart from the intermediate scattering function, there are other ways to quantify the structure of a liquid. In this section we shall examine several structural parameters, and determine which of those are the most effective in distinguishing between LDL, HDL, and the crystal. Apart from considering several global parameters, we

shall mainly focus on local parameters which can be used to analyze the local environment of a molecule. In addition, we study here not only the parameters based on the nearest neighbors, but also those based on the next-nearest neighbors (the second coordination shell). Finally, we determine the best local parameter to use for identifying tiny crystals in the liquid, an important result that will be used in the next section.

The structural parameters are designed to distinguish between different phases by analyzing the geometrical structure. This is typically done by evaluating the spherical harmonics $Y_\ell^m(\varphi, \vartheta)$ for a particular set of neighboring atoms, with φ and ϑ the polar angles between each pair of oxygen atoms in that set. In this chapter we consider two different sets: we define the first coordination shell $n_1(i)$ to be the four nearest neighbors of molecule i, and define the second coordination shell $n_2(i)$ as the fifth to sixteenth nearest neighbors (the sixteenth nearest neighbors minus those in the first shell). For simplicity, we approximate the center of mass of a water molecule with the center of its oxygen atom.

Different values of ℓ are sensitive to different symmetries. The spherical harmonics with $\ell = 3$, for example, are sensitive to a diamond structure. Those with $\ell = 6$ are more sensitive to the hexagonal closest packing (hcp) structure. Since we expect the liquid and crystal structures to be hcp, diamond, or a mix of these, we focus primarily on $\ell = 3$ and $\ell = 6$.

3.6.1 Parameters q_3 and q_6

All parameters defined in this section are based on $q^{(s)}_{\ell,m}(i)$ which quantifies the local symmetry around molecule i. It is defined as

$$q^{(s)}_{\ell,m}(i) \equiv \frac{1}{N_s} \sum_{j \in n_s(i)} Y^m_\ell(\varphi_{ij}, \vartheta_{ij}) \quad -\ell \leq m \leq \ell \tag{3.7}$$

where ℓ and m are integers, $s = 1, 2$ indicates the shell we are considering, and with N_s the number of molecules within that shell (i.e. $N_1 \equiv 4$ for the first coordination shell, and $N_2 \equiv 12$ for the second). Y^m_ℓ is normalized according to $\int |Y^m_\ell|^2 \sin(\vartheta) \mathrm{d}\varphi \mathrm{d}\vartheta = 1$. We can consider $q^{(s)}_{\ell,m}(i)$ as a vector $\mathbf{q}^{(s)}_\ell(i)$ in a $(4\ell + 2)$-dimensional Euclidean space having components $\mathrm{Re}(q^{(s)}_{\ell,m}(i))$ and $\mathrm{Im}(q^{(s)}_{\ell,m}(i))$. This means that we can define an inner product

$$\mathbf{q}^{(s)}_\ell(i) \cdot \mathbf{q}^{(s)}_\ell(j) \equiv \sum_{m=-\ell}^{\ell} \left[\mathrm{Re}(q^{(s)}_{\ell,m}(i)) \, \mathrm{Re}(q^{(s)}_{\ell,m}(j)) + \mathrm{Im}(q^{(s)}_{\ell,m}(i)) \, \mathrm{Im}(q^{(s)}_{\ell,m}(j)) \right] \tag{3.8}$$

and a magnitude

$$q^{(s)}_\ell(i) \equiv \sqrt{\mathbf{q}^{(s)}_\ell(i) \cdot \mathbf{q}^{(s)}_\ell(i)} \tag{3.9}$$

The local parameter $q^{(s)}_\ell(i)$ is one way to distinguish between different structures, and can be used to label individual molecules as LDL-like or HDL-like. We can convert it into a global parameter by averaging over all molecules,

$$q^{(s)}_\ell \equiv \frac{1}{N} \sum_{i=1}^{N} q^{(s)}_\ell(i) \tag{3.10}$$

where N is the total number of molecules. In Fig. 3.8 we see that all global $q_\ell^{(s)}$ are sensitive to the difference between LDL and HDL, especially $q_3^{(1)}$ and $q_6^{(2)}$. We conclude that the structural difference is visible in both the first and second shell, and that LDL and HDL differ mostly in the amount of diamond structure of the first shell and the amount of hcp structure in the second shell. This is confirmed by the histograms in Fig. 3.9, in which the largest difference between LDL and HDL is seen in $q_3^{(1)}$ and, next, in $q_6^{(2)}$. The latter is the parameter that better discriminate with respect to the crystal structure.

3.6.2 Global parameters Q_3 and Q_6

An alternative approach, as used by Steinhardt *et al.* [191], is to first average $q_{\ell,m}^{(s)}(i)$ over all molecules, defining $Q_{\ell,m} \equiv \sum_{i=1}^{N} q_{\ell,m}^{(s)}(i)$, and then calculate the magnitude

$$Q_\ell^{(s)} \equiv \frac{1}{N}\left(\sum_{m=-\ell}^{\ell} Q_{\ell,m} Q_{\ell,m}^*\right)^{1/2}. \tag{3.11}$$

Our calculations show that the parameters $Q_3^{(s)}$ and $Q_6^{(s)}$, with $s = 1$, 2, are not efficient in discriminating between LDL and HDL (Fig. 3.8), although $Q_6 \equiv Q_6^{(1)}$ has been proposed recently as a good parameter to this goal [110] and consequently has been used by several authors [173, 112, 149]. In particular, we observe that there is not much correlation between the fluctuations of $Q_\ell^{(s)}$ and those of the density, except for $Q_3^{(1)}$.

However, we confirm that $Q_6^{(1)}$ and $Q_6^{(2)}$ are excellent parameter to distinguish between the liquids (LDL and HDL) and the crystal, with the value of $Q_6^{(s)}$ approximately 10 times larger for the crystal than it is for the liquids (Fig. 3.10). This large increase of $Q_6^{(s)}$ for crystal-like structures might be related to the few instances

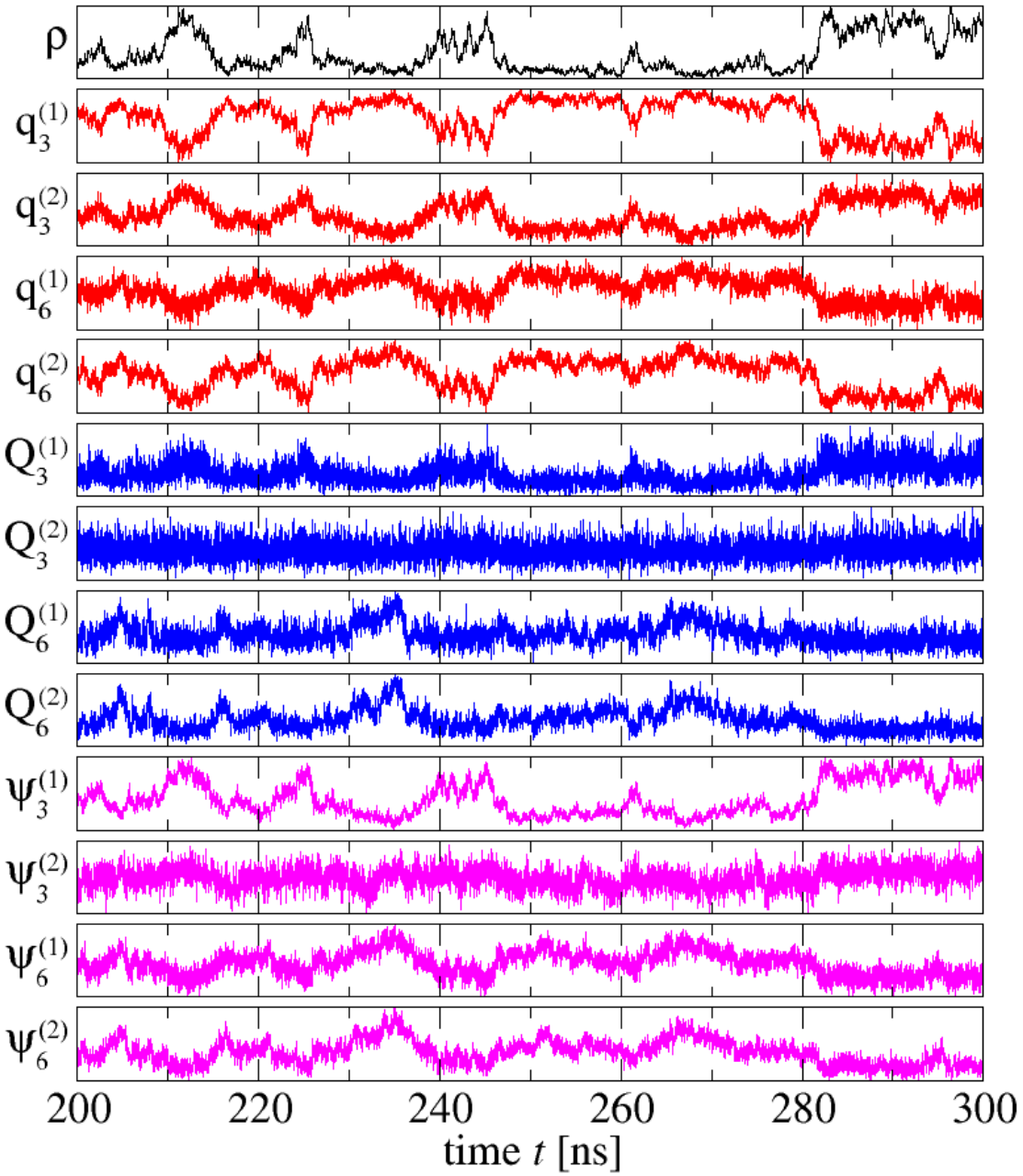

Figure 3.8: Fluctuations of the density and the global structural parameters as a function of time. The parameters are shown for one run using 343 molecules at 200 MPa and 248 K, the same as in Fig. 3.5. Parameters $q_3^{(1)}$, $q_6^{(2)}$, and $\psi_3^{(1)}$ (defined in the text) are as sensitive as ρ to the difference between LDL-like and HDL-like structures, while the others are more noisy, with $Q_3^{(2)}$ and $\psi_3^{(2)}$ being much less sensitive than all the others. $Q_6^{(s)}$ and $\psi_6^{(s)}$, for both $s = 1$ and 2, have similar behaviors that might be related to the temporary appearance of crystal-like structures.

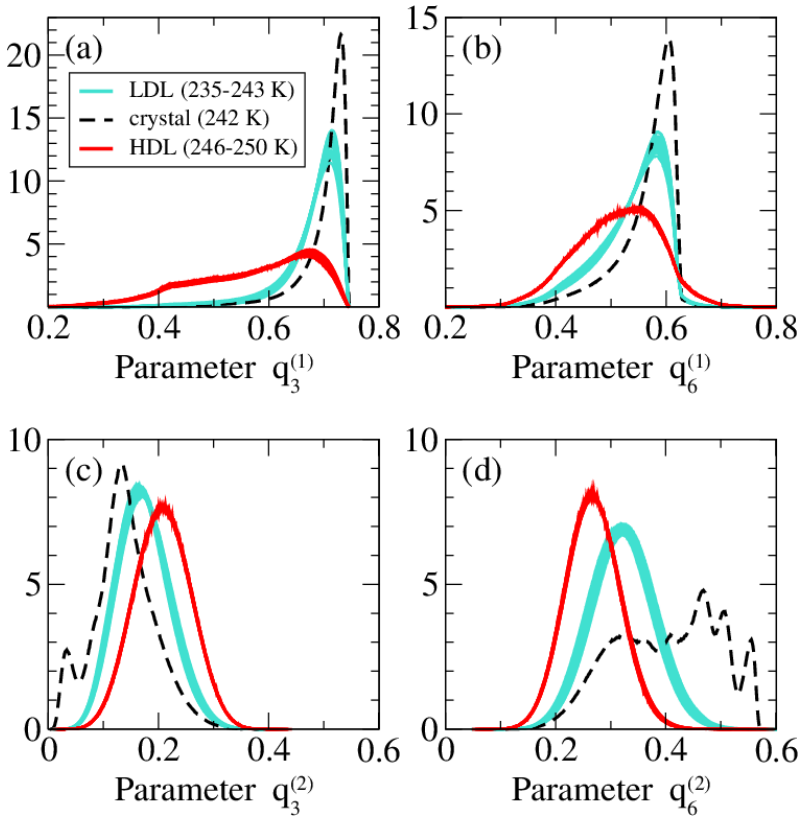

Figure 3.9: Histograms of $q_\ell^{(s)}$ for $\ell = 3, 6$ and coordination shells $s = 1, 2$ at 215 MPa with $N = 343$ molecules. The solid red (dark) curves correspond to HDL structures, and the solid blue (light) curves to LDL structures. The dashed black curve corresponds to the crystal structure found in run C described in Sec. 3.7. The parameter $q_3^{(1)}$ (a) discriminates better between HDL and LDL structures, while the parameter $q_6^{(2)}$ discriminates better between liquid-like and crystal-like structures. Parameters in (b) and (c) are much less sensitive to structural changes.

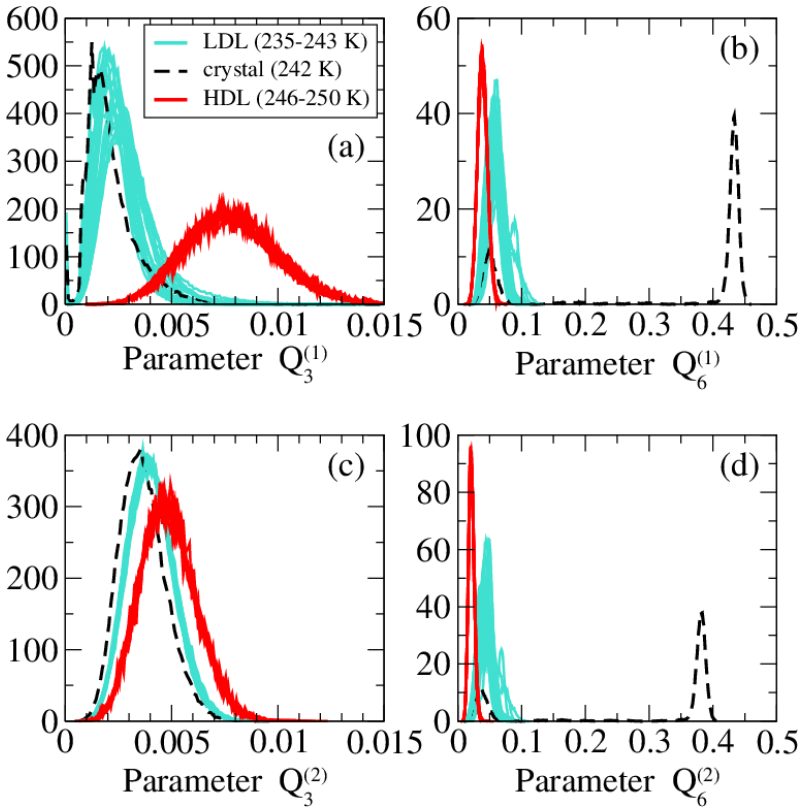

Figure 3.10: Histograms of $Q_\ell^{(s)}$ for $\ell = 3, 6$ and coordination shells $s = 1, 2$ at 215 MPa with $N = 343$ molecules. The symbols are as in Fig. 3.9. The parameter $Q_6^{(s)}$, for the first shell in (b) and the second in (d), shows a clear difference between the liquid-like structures and the crystal-like structure, but not between the two liquids. Note that scales on x-axis in panels (a) and (c) are one order of magnitude smaller than those in panels (b) and (d). As a consequence, $Q_3^{(s)}$, for the first shell in (a) and the second in (c), is much less sensitive to structural changes than $Q_6^{(s)}$.

in Fig. 3.8 where an increase in $Q_6^{(s)}$ corresponds to a decrease of density (such as within interval $t = 230$–237 ns), consistent with the observation that the crystal-like structures have a density comparable to the LDL structure and smaller than the HDL structure.

To confirm that LDL remains a liquid in the thermodynamic limit, we look at how Q_6 changes with the system size. For liquids Q_6 scales like $N^{-1/2}$ while for crystals the value Q_6 remains finite as $N \to \infty$. We find that the probability distribution functions of $Q_6 N^{1/2}$ for $N = 216$, 343, 512, and 729 overlap, which means that $Q_6 N^{1/2}$ is independent of the system size, therefore $Q_6 \sim N^{-1/2}$ (Fig. 3.11). We conclude that the metastable LDL is not transforming into the stable crystal in the thermodynamic limit. This implies that the LDL and the crystal phase are separated by a free-energy barrier that is higher than $k_B T$ at the temperatures we consider here, and that the system equilibrates to the stable (crystal) phase only on a time scale that is infinite with respect to our simulation time (1000 ns), as occur in experiments for metastable phases. Therefore, the LDL is a *bona fide* metastable state. Our conclusion is consistent with recent calculations by other authors [173, 112, 149].

3.6.3 Bond parameters d_3 and ψ_3

We define the bond order parameter $d_\ell^{(s)}$ similar to that defined by Ghiringhelli *et al.* in Ref. [64], where the quantity $d_3^{(1)}(i,j)$ characterizes the bond between molecules i and j, and is designed to distinguish between a fluid and a diamond structure. The local parameter $d_\ell^{(s)}(i,j)$ is defined as the cosine of the angle between the vectors

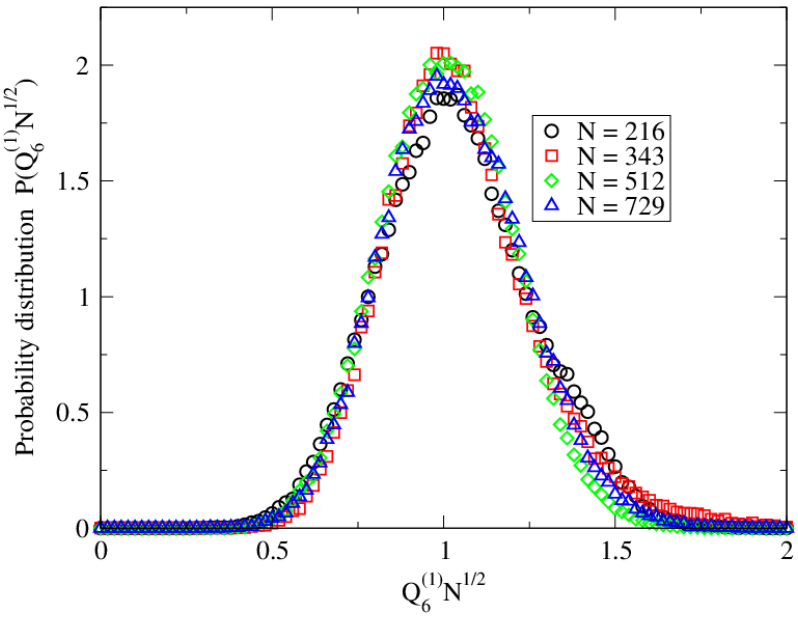

Figure 3.11: Finite size scaling of parameter Q_6 in the LDL phase (210 MPa, 243 K). The probability distribution function of $Q_6 N^{1/2}$ is independent of the system size N, which means LDL scales like a liquid in the thermodynamic limit: $Q_6 \sim N^{-1/2}$.

$\mathbf{q}_\ell^{(s)}(i)$ and $\mathbf{q}_\ell^{(s)}(j)$:

$$d_\ell^{(s)}(i,j) \equiv \frac{\mathbf{q}_\ell^{(s)}(i) \cdot \mathbf{q}_\ell^{(s)}(j)}{\left|\mathbf{q}_\ell^{(s)}(i)\right| \left|\mathbf{q}_\ell^{(s)}(j)\right|} \tag{3.12}$$

with the inner product and magnitude as defined in Eqs. (3.8) and (3.9).

A crystal with a perfect diamond structure has $d_3^{(1)}(i,j) = -1$ for all bonds. For a graphite crystal only the bonds within the same layer (three out of four) have $d_3^{(1)}(i,j) = -1$, while the bonds connecting atoms in different layers (one out of four) have $d_3^{(1)}(i,j) = -1/9$.

We find that the parameters $d_\ell^{(s)}$ for $\ell = 3$, 6 and $s = 1$, 2 do not distinguish well between the two different liquid-like structures, but that $d_3^{(1)}$ and $d_6^{(s)}$ for both $s = 1$ and 2 are suitable to discriminate between the crystal-like structure and the liquids (Fig. 3.12). In particular, for the crystal, most molecules have $d_3^{(1)} < -0.87$,

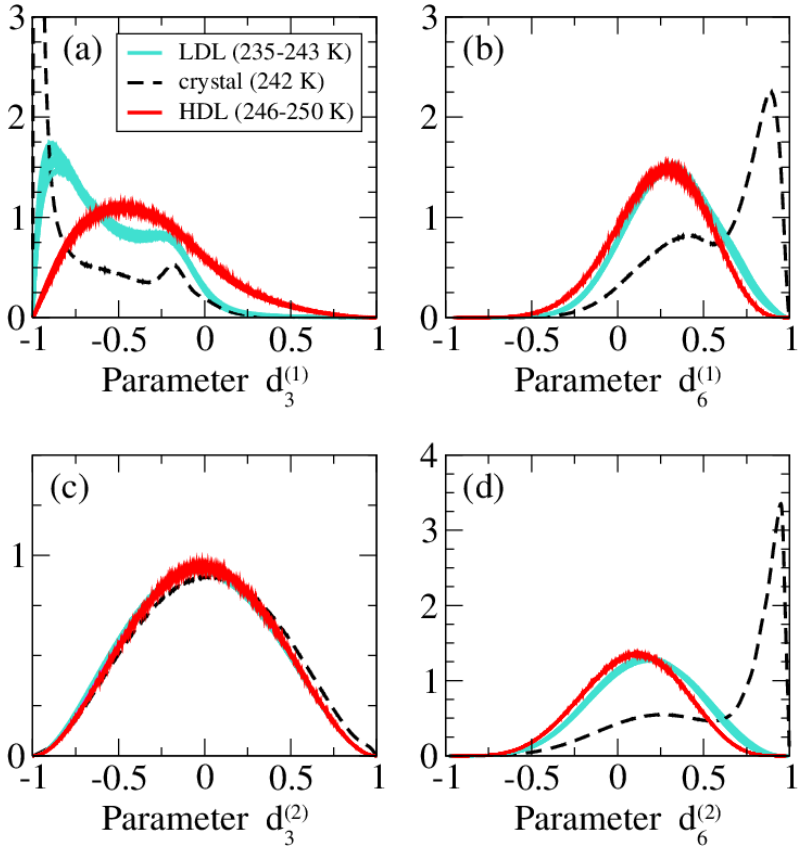

Figure 3.12: Histograms of $d_\ell^{(s)}$ for $\ell = 3, 6$ and coordination shells $s = 1, 2$ at 215 MPa with $N = 343$ molecules. The symbols are as in Fig. 3.9. Apart from $d_3^{(1)}$ in (a), these parameters do not distinguish well between the two different liquid-like structures, but $d_3^{(1)}$ and $d_6^{(s)}$ for the first shell (b) and the second (d) are suitable to distinguish between the crystal and the liquids. The parameter $d_3^{(2)}$ in (c) is remarkably the same for the three structures.

and we therefore consider a molecule to be part of a crystal if at least three out of its four bonds with its nearest neighbors have $d_3^{(1)} < -0.87$. This is the same cutoff used by Ghiringhelli *et al.* in [64].

The global parameter associated with $d_\ell^{(s)}(i,j)$ is defined as

$$\psi_\ell^{(s)} \equiv \frac{1}{N}\sum_{i=1}^{N} \psi_\ell^{(s)}(i) \tag{3.13}$$

where

$$\psi_\ell^{(s)}(i) \equiv \frac{1}{4}\sum_{j=1}^{4} d_\ell^{(s)}(i,j) \tag{3.14}$$

is the average of $d_\ell^{(s)}(i,j)$ over the first four nearest neighbors of the molecule i. We observe that each $\psi_\ell^{(s)}(i)$ has the same features of the corresponding $d_\ell^{(s)}(i,j)$, with $\psi_3^{(1)}(i)$ discriminating well between the crystal-like and the liquids-like structures (Fig. 3.13). We observe that $\psi_3^{(1)}$ discriminates well between LDL-like and HDL-like structures (Fig. 3.8), while $\psi_6^{(s)}$ for $s = 1$ and 2 might be able to emphasize the temporary appearance of crystal-like structures, as noted for $Q_6^{(s)}$.

In Fig. 3.14 we see that there is no significant difference between the low-T curves at $P = 240$ MPa, 215 MPa (Fig. 3.13a) and 195 MPa, and no significant difference between the high-T curves. We therefore conclude that at the Widom line the low density liquid (at low T) is LDL-like, and similarly that the high density liquid (at high T) is HDL-like.

From the figure we can also see that the difference between the LDL- and HDL-structure decreases when we decrease P, indicating that far from the LLPT the distinction between LDL-like and HDL-like disappears as is to be expected in the one-phase region.

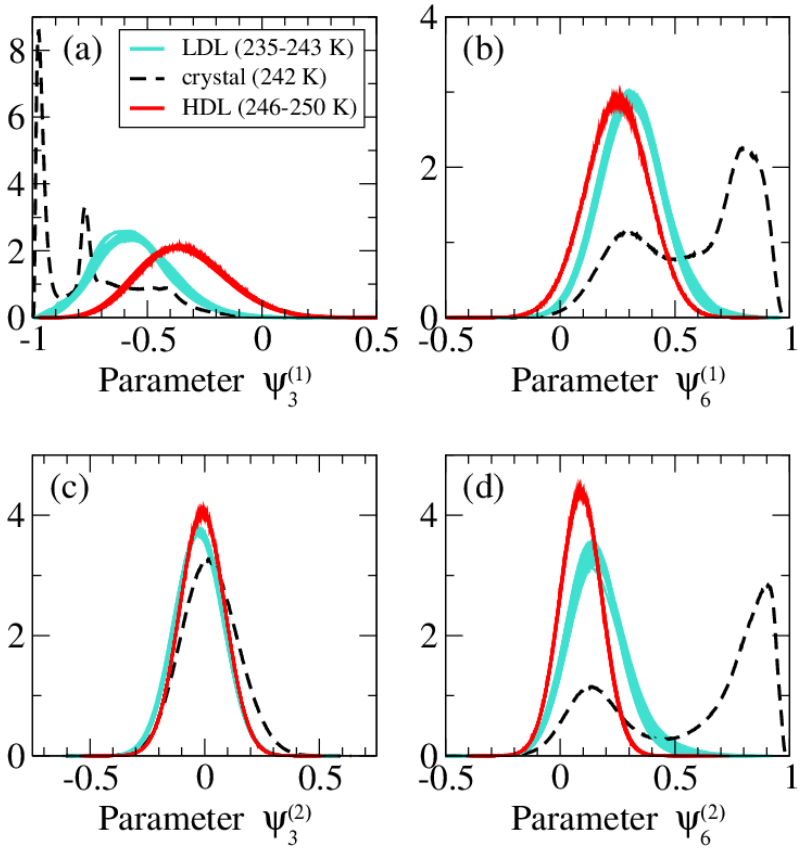

Figure 3.13: Histograms of $\psi_\ell^{(s)}$ for $\ell = 3, 6$ and coordination shells $s = 1, 2$ at 215 MPa with $N = 343$ molecules. The symbols are as in Fig. 3.9. Each $\psi_\ell^{(s)}(i)$ has similar features as the corresponding $d_\ell^{(s)}(i, j)$ in Fig. 3.12.

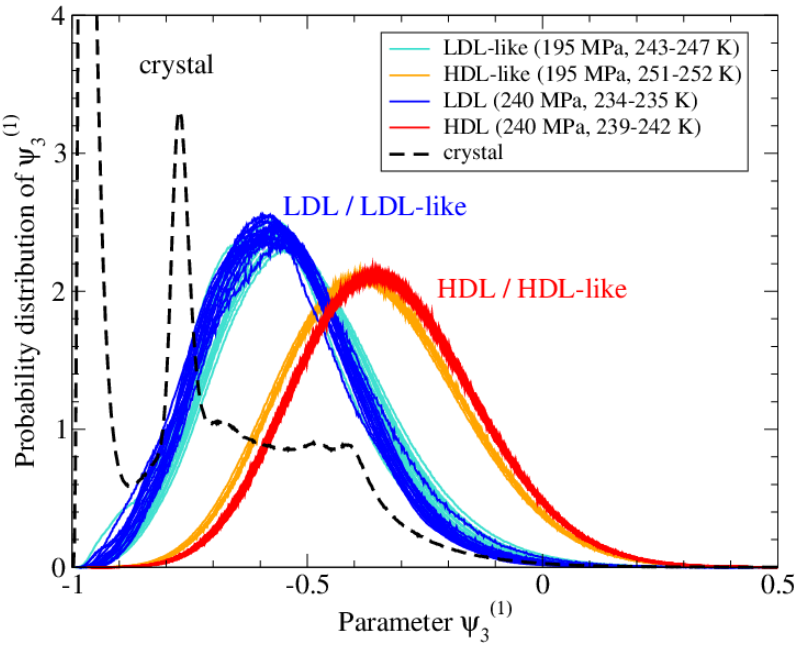

Figure 3.14: Probability distribution function of $\psi_3^{(1)}$ for both $P = 195$ MPa and 240 MPa, with $N = 343$ molecules (see Fig. 3.13a for $P = 215$ MPa). At the Widom line (195 MPa) the structure of the low-density liquid is similar to that of LDL at 240 MPa, and the structure of the high-density liquid near the Widom line is practically the same as HDL. This demonstrates that we the LDL-like and HDL-like phases are indeed structurally similar to LDL and HDL. Furthermore, the structural difference between the LDL-like and HDL-like phases becomes smaller as we move away from the phase transition line to lower and lower pressures.

3.7 Growth and melting of crystal nuclei

In a small percentage of our simulations, the system was found to spontaneously crystallize. These are interesting events because spontaneous crystallization of water in molecular dynamics is extremely rare; only recently Matsumoto *et al.* were the first to successfully simulate the freezing of water on a computer [119]. Crystallization events in supercooled ST2 water are particularly important to study, as it has been proposed that LDL is unstable with respect to crystallization [110, 111].

Following the discussion in Sec. 3.6, we define a crystal as a cluster of molecules which has three out of four bonds with $d_3^{(1)} < -0.87$ and belong to the first coordi-

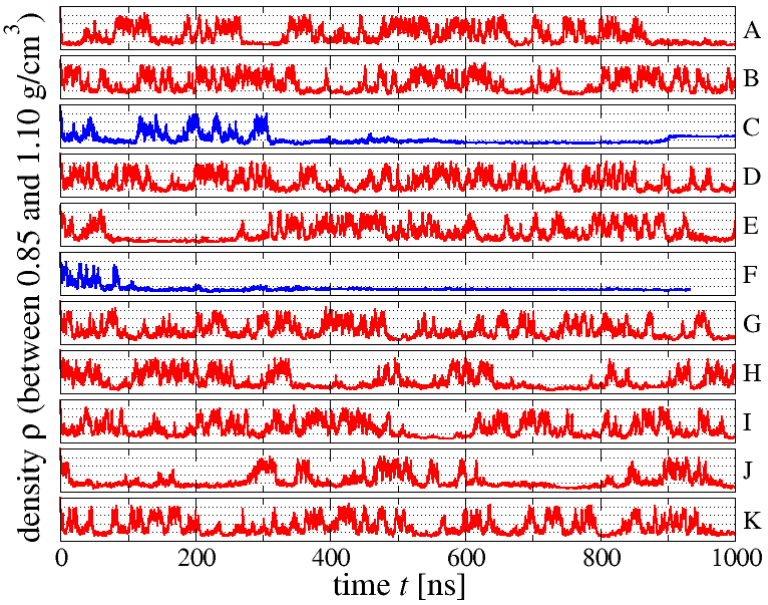

Figure 3.15: Density vs. time near the phase transition line at $P = 205$ MPa and $T = 246$ K for several different configurations of $N = 343$ molecules. This state point lies near the phase transition, and therefore phase flipping is seen to occur. Runs C and F (partially) crystallize and, at that moment, cease to phase flip and remain stable at a low density.

nation shell of each other. In this section we shall study the growth and melting of these crystal nuclei, and estimate the critical nucleus size needed to overcome the free energy barrier. The existence of this barrier allows us to conclude that LDL is in fact a *bona fide* metastable state with respect to the crystal.

In Fig. 3.15 we show the density evolution for 11 different configurations, each with 343 molecules and at 205 MPa and 246 K. Each of these runs started at a different initial density (between 0.85 and 0.95 g/cm^3) and was subsequently equilibrated to the final temperature and pressure using the procedure described in Sec. 3.3. Because this state point lies close to the LLPT, we see phase flipping in all of them. However, the two configurations C and F display a sudden jump to a stable low density plateau. This is a hallmark of crystallization. We confirm this by calculating the size of the largest crystal as a function of time (Fig. 3.16). During most runs the

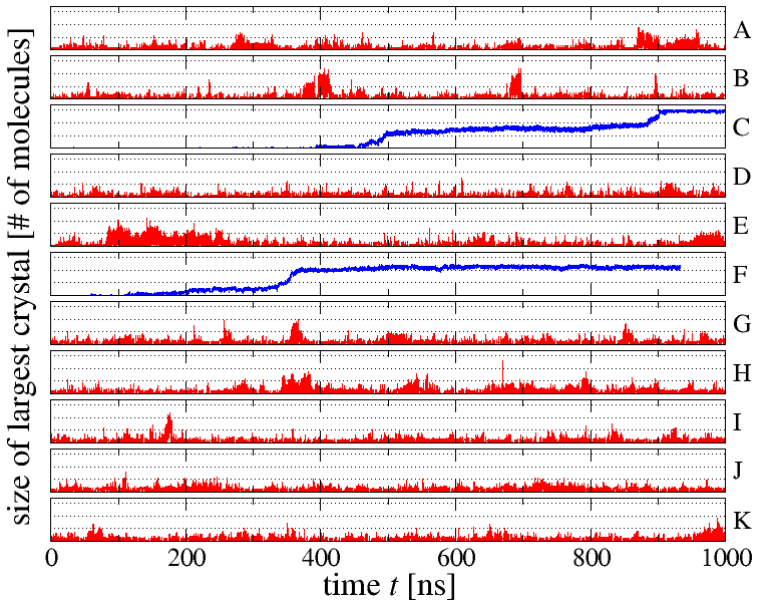

Figure 3.16: Evolution of crystal size with time for the same configurations as in Fig. 3.15. The y-axis goes from 0 to 34, except for configurations C and F which go up to 343. The system spontaneously crystallizes in both C and F, while the largest crystals in the remaining configurations never reach a size larger than 30 molecules.

largest crystal continuously grows and shrinks, but never reaches a size larger than 30 molecules. On the other hand, configurations C and F show a jump in crystal size exactly matching the jump in density. Run F ends up partially crystallized, while for C we find that over 90% of the box is crystallized in a diamond structure with a density of about 0.92 g/cm^3 (Fig. 3.17).

The correlation time increases dramatically if crystals appear with a size comparable to the system size, as is evident from Fig. 3.18. The correlation functions of C and F decay very slowly, leading to correlation times of 200–400 ns, while the other configurations have a correlation time of less than 4 ns.

For spontaneous crystallization to occur, a sufficiently large crystal nucleus needs to form within the liquid. According to classical nucleation theory, this nucleus needs to reach a minimum size to prevent it from melting. We observed in many

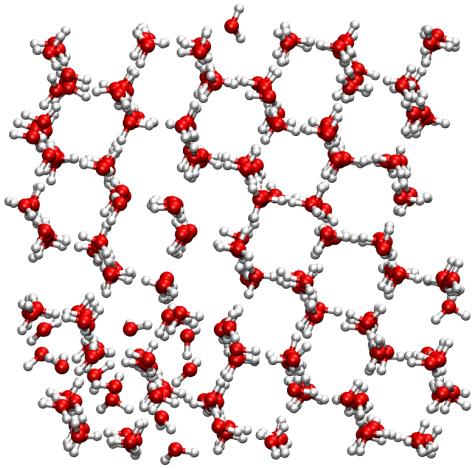

Figure 3.17: A snapshot (at $t = 1000$ ns) of the diamond cubic crystal produced by run C of Figs. 3.15 and 3.16. Shown here are all $N = 343$ molecules, with a small part still in the liquid state (bottom-left corner), and a crystal defect in the center. Note that the defect only affects the position of the hydrogen atoms, and not that of the oxygen.

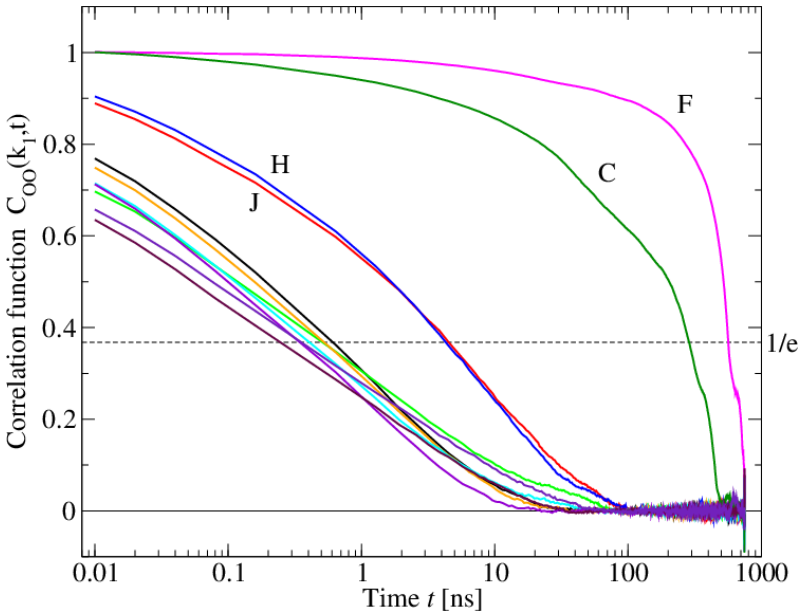

Figure 3.18: The correlation time increases dramatically if crystals of a size comparable to the system size appear (i.e. runs C and F of Figs. 3.15 and 3.16). The correlation time of two other runs (H and J) are slightly larger than average because these runs spend more time in the LDL phase (see Fig. 3.15).

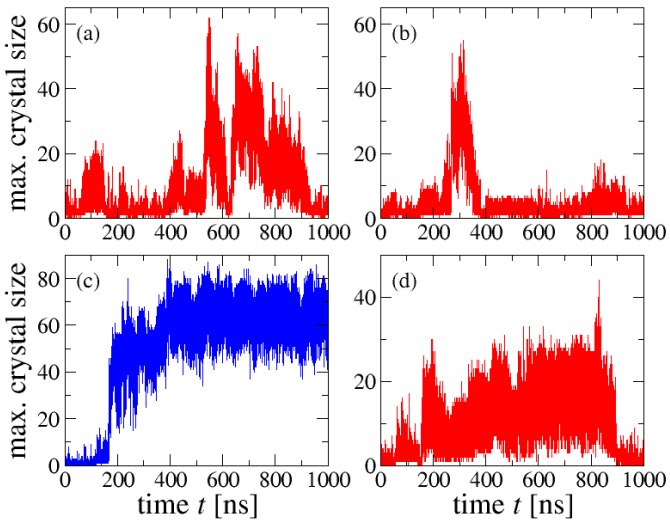

Figure 3.19: Growth and melting of crystal nuclei. (a) The largest nucleus that melted reached a size of 62 molecules during a simulation of 512 molecules at 210 MPa and 244 K. (b) The second-largest nucleus was 55 molecules during a simulation of 343 molecules at 210 MPa and 243 K. (c) A few runs lead to irreversible crystallization ($N = 216$ at 195 MPa and 245 K). (d) Some crystal nuclei survive for hundreds of nanoseconds ($N = 343$ at 195 MPa and 246 K) before disappearing.

simulations that a small nucleus grows and melts, and a few runs in which the nucleus grows further or remains stable. Therefore, we can make an estimate of the critical nucleus size.

The two largest crystals that formed and subsequently melted, both reached a size of about 50–60 molecules (Fig. 3.19a and 3.19b). The smallest crystal that formed and remained stable, had a size of about 50–80 molecules (Fig. 3.19c). We therefore conclude that the critical nucleus size is approximately 70 ± 10 molecules. A similar value of $\simeq 85$ molecules was found by Reinhardt and Doye [154] for ice nucleation in the monatomic water model [131].

For a more accurate estimate it is necessary to run longer simulations, as the crystal nuclei can survive for hundreds of nanoseconds (e.g., Fig. 3.19d in which a small crystal lasts for 700 ns).

3.8 Location of the critical point

In Sec. 3.4 we used the intermediate scattering function $S_{OO}(k)$ to estimate the position of the liquid-liquid critical point, and found it to lie near 200–210 MPa and 244–247 K. It is commonly believed that the LLCP falls in the same universality class as the three-dimensional Ising model [113]. At the critical point the order parameter distribution function (OPDF) of a system has the same bimodal shape as all other systems that belong to the same universality class. Therefore one can locate the LLCP accurately by fitting our data to the OPDF of the 3D Ising model, as was done in [96]. Based on our fit, we locate the LLCP to be at $P_C = 206 \pm 3$ MPa and $T_C = 246 \pm 1$ K.

To establish that the LLPT does not vanish in the thermodynamic limit $N \to \infty$, we consider the finite-size scaling of the Challa-Landau-Binder parameter [36, 54, 50, 53, 201, 202]. Near the critical point the density distribution function $\mathcal{D}(\rho)$ has a bimodal shape that can be approximated by the superposition of two Gaussians. The Challa-Landau-Binder parameter Π is a measure of the bimodality of $\mathcal{D}(\rho)$ and is defined as

$$\Pi \equiv 1 - \frac{\langle \rho^4 \rangle}{3\langle \rho^2 \rangle^2} \tag{3.15}$$

When there is only one phase, $\mathcal{D}(\rho)$ is unimodal and $\Pi = 2/3$. But in a two-phase region, with two phases that have different densities, the shape of $\mathcal{D}(\rho)$ is bimodal (Fig. 3.20) and $\Pi < 2/3$. For a finite system $\mathcal{D}(\rho)$ is always bimodal at both the Widom line and the LLPT, but in the thermodynamic limit there exists only one phase at the Widom line, while there remain two at the phase transition line. Therefore, $\Pi \to 2/3$ at the Widom line, while $\Pi < 2/3$ at the LLPT even

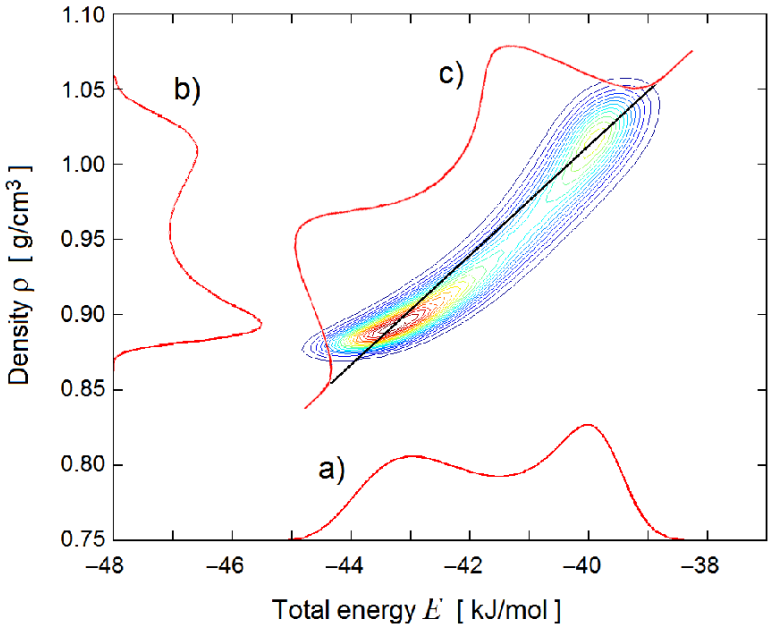

Figure 3.20: 2D histogram of the density and the total energy for a system at 247.5 K and 200 MPa (on the Widom line), obtained via histogram reweighting. The histogram of the energy (curve a) seems to indicate that the system is mostly in the LDL state, while the histogram of the density (curve b) indicates the HDL state is more predominant. For liquids the order parameter $M \equiv \rho + sE$ is actually a linear combination of the density ρ and the energy E (curve c), with $s = 0.0362$ (g/cm^3)/(kJ/mol). By fitting the OPDF (curve c) to the critical OPDF of the 3D Ising model, it is possible to accurately locate the critical point [96].

in the limit $N \to \infty$. Hence, the finite-size scaling of Π allows us to distinguish whether an isobar crosses the LLPT or the Widom line, and is yet another method of estimating the location of the critical point.

We study Π versus temperature T and system size N for different pressures, finding minima $\Pi_{\min}$ at a specific temperature for each pressure (Fig. 3.21). The finite-size dependence of $\Pi_{\min}(P)$ reveals if $P < P_C$ or $P > P_C$ (Fig. 3.22).

For $P < P_C$ the minimum $\Pi_{\min}$ approaches 2/3 linearly with $1/N$, while for

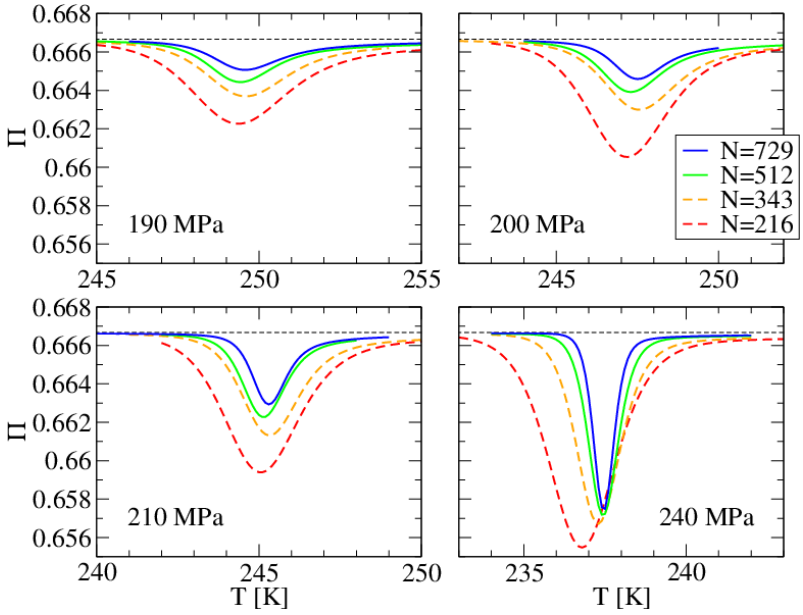

Figure 3.21: The Challa-Landau-Binder parameter Π as a function of temperature and system size N, for four different pressures. For finite system sizes Π shows a minimum at the LLPT and the Widom line, while $\Pi \approx 2/3$ (thin dashed line) at temperatures where $\mathcal{D}(\rho)$ is given by a single Gaussian. The finite-size scaling of the minimum of Π, indicates that the critical point exists in the thermodynamic limit (Fig. 3.22).

$P \leq P_C$ it approaches the limit [36]

$$\Pi_{\min} \to \frac{2}{3} - \frac{1}{3}\frac{(\rho_{\rm H}^2 - \rho_{\rm L}^2)^2}{(\rho_{\rm H}^2 + \rho_{\rm L}^2)^2}. \tag{3.16}$$

This limiting value is also approached linearly with $1/N$. Here $\rho_{\rm H} \equiv \rho_{\rm H}(P)$ and $\rho_{\rm L} \equiv \rho_{\rm L}(P)$ are the densities of the two phases LDL and HDL [50]. Above the critical pressure the limiting value of $\Pi_{\min}$ decreases as P increases, i.e. the two peaks of the bimodal $\mathcal{D}(\rho)$ move further apart. This happens because $\rho_{\rm H} - \rho_{\rm L}$ increases at coexistence as $(P - P_C)^\beta$ where $\beta \approx 0.3$ is the critical exponent of the 3D Ising universality class [76, 77].

From this analysis (Fig. 3.22) we conclude that our results agree with theory

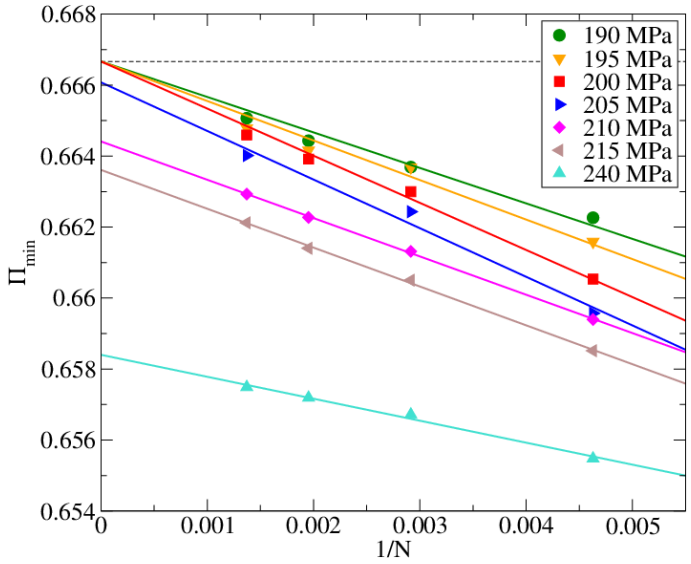

Figure 3.22: Minima of the Challa-Landau-Binder parameter Π as a function of system size N for different pressures. The minimum $\Pi_{\rm min}$ occurs at the pressures and temperatures of the LLPT and the Widom line, and is always less than 2/3 for a finite system because of the bimodality of the density histogram. As $N \to \infty$ the bimodality disappears in the one-phase region but remains at the LLPT, and therefore $\Pi_{\rm min} \to 2/3$ at the Widom line while $\Pi_{\rm min} < 2/3$ on the LLPT, even in the thermodynamic limit. We conclude that the critical point survives in the thermodynamic limit, and that it is located between $P = 200$ and 210 MPa (in agreement with the results found in Secs. 3.2 and 3.4).

and that the critical pressure $P_C \approx$ 190–210 MPa, in agreement with the estimate of Sec. 3.8. Furthermore, as Π remains less than 2/3 for $P > P_C$ even in the limit $N \to \infty$, we conclude that the LLPT does not vanish in the thermodynamic limit.

3.9 Conclusion

We performed molecular dynamic simulations in the NPT ensemble for ST2-RF water in the supercooled region of the phase diagram for different system sizes with simulation times of up to 1000 ns. Using several different techniques we confirmed the existence of two liquid phases, LDL and HDL, separated by a liquid-liquid phase transition line. Near the LLPT line the system continuously flips between the two

phases. Because of finite-size effects this phenomenon also occurs near the Widom line, but by fitting the order parameter distribution function to that of the 3D Ising model we were able to accurately determine the location of the liquid-liquid critical point (at $T_C = 246 \pm 1$ K, $P_C = 208 \pm 3$ MPa). These results agrees exactly with ($T_C = 246$ K, $P_C \approx 188$ MPa) as found by Poole *et al.* [151], with the discrepancy in pressure attributed to the LJ pressure correction of $\simeq -20$ MPa (see Sec. 3.3). Finite size scaling of the Challa-Landau-Binder parameter indicates that the critical point does not disappear in the thermodynamic limit.

Both phases have been confirmed to be *bona fide* metastable liquids that differ substantially in structural as well as dynamical properties. It is found that the LDL phase is a more "structured" liquid, and that it has a correlation time of almost four orders of magnitude larger than that of HDL, with LDL correlation time of the order of 100–1000 ns. We show that Q_6 structural parameter is not able to discriminate between HDL and LDL, but can discriminate well between liquids and crystal. Finite size scaling of the Q_6 parameter confirms that LDL scales as a liquid and not as a crystal.

The different structures of LDL and HDL are better discriminated by structural parameters like $q_3^{(1)}$ and $q_6^{(2)}$. These parameters show that LDL and HDL differ mostly in the amount of diamond structure of the first shell and the amount of hcp structure in the second shell.

For small box sizes ($N = 343$) there were a few simulation runs that resulted in spontaneous crystallization, always within the LDL region of the phase diagram. Further analysis revealed that during all simulations small crystals grow and melt within the liquid, a clear indication that LDL is metastable with respect to the crystal. From the few crystallization events that occurred, we were able to conclude that the critical nucleus size is approximately 70 ± 10 molecules.

CHAPTER 4: Search for the liquid-liquid transition in models of silica

> *We have found it of paramount importance that in order to progress, we must recognize our ignorance and leave room for doubt. Scientific knowledge is a body of statements of varying degrees of certainty—some most unsure, some nearly sure, but none absolutely certain.*
>
> – Richard. P. Feynman, in *The Value of Science*

4.1 Introduction

Previous research has indicated the possible existence of a liquid-liquid critical point (LLCP) in liquid silica [160]. As this point is located near or even below the glass transition, molecular dynamics simulations have thus far failed to accurately locate and characterize it. In this chapter we look at two different silica models, the BKS model (considered to be one of the most accurate descriptions of experimental silica currently available) and the WAC model (believed to have a LLCP that is more accessible), and perform a more detailed analysis of the phase diagram at lower temperatures than was simulated before.

Liquid SiO_2 is the archetypal glassformer, and the extreme "strong" member of the "strong-fragile" liquid spectrum (see Fig. 1.2). Silica is to geochemistry what water is to biochemistry [9]. Furthermore, like water, it is complex and incompletely understood. The glass transition of tetrahedral systems like water and silica are very different from "normal" glassforming liquids (Fig. 4.1). Both substances are characterized by a heat capacity behavior quite atypical of normal glassformers, namely a tiny increase at T_g and an increasing value as T increases above T_g [175, 8]. This is in contrast with the normal large increase at T_g, and decrease as T rises

above it for molecular liquids. Therefore the strong liquid behavior of silica might be a consequence of the same factors that lead water itself to behave as a "strong" liquid near its glass transition temperature. Since some theories predict a liquid-liquid critical point (LLCP) in water, it makes sense to investigate the possibility of a LLCP in liquid silica.

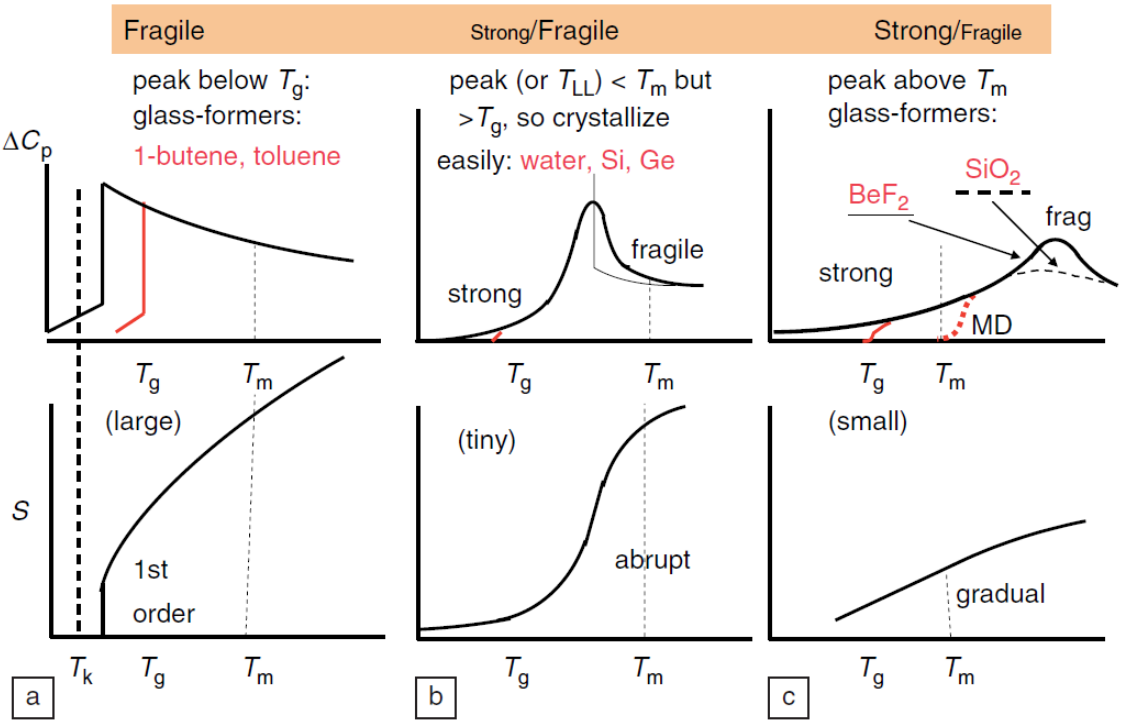

Figure 4.1: Even though the fragility of a glass-forming liquid is usually defined via its dynamic properties (see Fig. 1.2), the behavior of the heat capacity (a thermodynamic quantity) is also different for fragile and strong glass-formers. (a) Fragile liquids such as molecular liquids and metallic glass-formers show a sharp drop in the excess heat capacity ΔC_P, which is related to a first-order transition in the excess entropy S. (b) For tetrahedral liquids (such as water, Si, and Ge) this transition in entropy is no longer a first-order transition. It is still quite abrupt, however: the heat capacity shows a large maximum separating a region with strong behavior (low T) from a region with fragile behavior (high T). (c) This transition is even more gradual for liquids such as SiO_2 and BeF_2 (figure taken from [8]).

4.2 Models of liquid silica

There are several models for silica. One of the simplest models is the WAC model introduced by L. V. Woodcock, C. A. Angell, and P. Cheeseman [218]. The model is sometimes also known as the Transferrable Ion Model (TRIM), as its potential is quite general and can also be used to model other ionic liquids [70]. In the WAC model, the material simply consists of a 1:2 mixture of Si^{+4} and O^{-2} ions, without any explicit bonds. Apart from the electrostatic force, the ions also interact with each other via an exponential term, which is the repulsive part of the Buckingham potential (representing the interpenetration of the closed electron shells [28]):

$$U_{\mathrm{WAC}}(r_{ij}) \equiv \frac{1}{4\pi\varepsilon_0}\frac{z_i z_j e^2}{r_{ij}} + a_{ij}\left(1 + \frac{z_i}{n_i} + \frac{z_j}{n_j}\right)\exp\left[B_{ij}(\sigma_i + \sigma_j - r_{ij})\right] \tag{4.1}$$

Here the subscripts $i, j \in$ Si,O indicate the species of the two ions involved, z_i the charge of each ion ($z_{\mathrm{Si}} = +4$, $z_{\mathrm{O}} = -2$), $n_{\mathrm{Si}} = n_{\mathrm{O}} = 8$ the number of outer shell electrons, and σ_i the size of each ion ($\sigma_{\mathrm{Si}} = 0.1310$ nm, $\sigma_{\mathrm{O}} = 0.1420$ nm). For WAC silica the parameters a_{ij} and b_{ij} are the same for all pairs: $a_{ij} = 0.19 \times 10^{-19}$ J/ion ≈ 11.44 kJ/mol and $B_{ij} = 34.48$ nm^{-1} [70]. The potential can also be written as

$$U_{\mathrm{WAC}}(r_{ij}) = \frac{1}{4\pi\varepsilon_0}\frac{q_i q_j}{r_{ij}} + A_{ij}\exp(-B_{ij}r_{ij}) \tag{4.2}$$

with $A_{\mathrm{SiSi}} = 1.917\,991\,469 \times 10^5$ kJ/mol, $A_{\mathrm{SiO}} = 1.751\,644\,217 \times 10^5$ kJ/mol, and $A_{\mathrm{OO}} = 1.023\,823\,519 \times 10^5$ kJ/mol.

The second model that we consider in this chapter is BKS. Currently one of the most popular models, the BKS model was introduced by B. W. H. van Beest, G. J. Kramer, and R. A. van Santen [17], and is very similar to WAC. Again, silica is modeled as a simple 1:2 mixture of Si- and O-ions, and with no explicit bonds.

To produce results that better match experiments and *ab initio* simulations, and to be able to effectively represent screening effects, the charges in BKS are not integer values of e but are instead given by $q_{\mathrm{Si}} = +2.4e$ and $q_{\mathrm{O}} = -1.2e$. Apart from the charges having different values, the BKS potential also differs from WAC because it includes the attractive r^{-6} term of the Buckingham potential:

$$U_{\mathrm{BKS}}(r_{ij}) \equiv \frac{1}{4\pi\varepsilon_0}\frac{q_i q_j}{r_{ij}} + A_{ij}\exp(-B_{ij}r_{ij}) - C_{ij}r_{ij}^{-6} \tag{4.3}$$

There is no Buckingham interaction between two Si-ions (only electrostatic), i.e. $A_{\mathrm{SiSi}} = B_{\mathrm{SiSi}} = C_{\mathrm{SiSi}} = 0$. The parameters for the Si-O pair are $A_{\mathrm{SiO}} \equiv 18\,003.7572$ eV, $B_{\mathrm{SiO}} \equiv 4.87318$ Å^{-1}, and $C_{\mathrm{SiO}} \equiv 133.5381$ eV Å^6. For the O-O interaction, the numbers are $A_{\mathrm{OO}} \equiv 1388.7730$ eV, $B_{\mathrm{OO}} \equiv 2.76$ Å^{-1}, and $C_{\mathrm{OO}} \equiv 175$ eV Å^6.

Although the BKS model has been quite successful in simulations of quartz and amorphous silica, at temperatures above $\sim$ 5000K two ions can come very close, causing problems. As $r \to \infty$ the BKS potential diverges to $-\infty$ and the two ions fuse together—a non-physical phenomenon that is an artifact of the model. One way to solve this issue is by including an additional repulsive term at very small r, e.g., by adding a r^{-30} term [160]. When such a large power is used, however, a small time step is required to prevent large forces, which leads to much slower simulations. Because of this, we instead adjust the BKS potential at small r by adding a second-degree polynomial for $r \leq r_{\mathrm{s}}$. Here r_{s} is the point at which the original BKS force has an inflection, i.e., where $d^2F_{\mathrm{BKS}}/dr^2 = -d^3U_{\mathrm{BKS}}/dr^3 = 0$. We choose the coefficients of the polynomial such that the new potential $U(r)$ has no inflection at $r = r_{\mathrm{s}}$. Adding the polynomial still leads to $U(r) \to -\infty$ when $r \to 0$, but increases the height of the energy barrier sufficiently to allow us to simulate the high temperatures we wish to explore. Choosing a short-range correction to BKS

	Si-O	O-O	units
a_{ij}	$2.678\,430\,850\times10^{5}$	$9.208\,901\,230\times10^{4}$	$\mathrm{kJ/mol\,nm^2}$
b_{ij}	$-7.343\,377\,221\times10^{4}$	$-4.873\,373\,066\times10^{4}$	$\mathrm{kJ/mol\,nm}$
c_{ij}	$2.353\,960\,789\times10^{3}$	$7.337\,042\,047\times10^{3}$	kJ/mol
A_{ij}	$1.737\,098\,076\times10^{6}$	$1.339\,961\,920\times10^{5}$	kJ/mol
B_{ij}	48.7318	27.6	$\mathrm{nm^{-1}}$
C_{ij}	$1.288\,446\,484\times10^{-2}$	$1.688\,492\,907\times10^{-2}$	$\mathrm{nm^6\,kJ/mol}$
$U_{\mathrm{c},ij}$	$-0.465\,464\,470$	$-0.575\,753\,031$	kJ/mol
r_s	0.139 018 528	0.195 499 453	nm
r_c	0.55	0.55	nm

Table 4.1: Parameters of the modified BKS potential of Eq. (4.4). Because Si-Si only has the (repulsive) Coulomb interaction, all parameters are zero for Si-Si. One mol here indicates one mol of ions, not one mol of SiO_2 molecules.

has been found to have little effect on the simulation results, and merely prevents the ions from fusing.

To further speed up the simulations, we modify the BKS potential as described by K. Vollmayr, W. Kob, and K. Binder in Ref. [212], and truncate and shift the potential at $r_\mathrm{c} = 0.55$ nm. Although this truncation leads to a shift in pressure, it otherwise produces approximately the same results [212]. In conclusion, the modified BKS potential we use is given by

$$U'_\mathrm{BKS}(r_{ij}) = \frac{1}{4\pi\varepsilon_0}\frac{q_i q_j}{r_{ij}} + \begin{cases} a_{ij}r_{ij}^2 + b_{ij}r_{ij} + c_{ij} - \frac{1}{4\pi\varepsilon_0}\frac{q_i q_j}{r_{ij}} & (r_{ij} < r_\mathrm{s}) \\ A_{ij}\exp(-B_{ij}r_{ij}) - C_{ij}r_{ij}^{-6} - U_{\mathrm{c},ij} & (r_\mathrm{s} < r_{ij} < r_\mathrm{c}) \\ 0 & (r_{ij} > r_\mathrm{c}), \end{cases} \tag{4.4}$$

with the parameter values for $ij = \mathrm{SiO}$ and $ij = \mathrm{OO}$ listed in Table 4.1. For the Si-Si interaction the potential is $U'_\mathrm{BKS}(r_\mathrm{SiSi}) = \frac{1}{4\pi\varepsilon_0}q_\mathrm{Si}^2/r_{ij}$ and does not involve any cutoffs, apart from the real-space cutoff of the Ewald sum.

All simulations are done using Gromacs 4.6.1 [74], with $N = 1500$ ions, using the

Ewald sum (PME) for electrostatics, and the v-rescale thermostat [32] to keep the temperature constant. Most simulations are done in the constant-volume/constant-temperature (NVT) ensemble. For the few constant-pressure (NPT) simulations we use the Parrinello-Rahman barostat. For most of the simulations we use a time step of 1 fs, but at very low temperatures we increase the time step to 4 fs to speed up the simulations to approximately 250 ns/day using 16 threads on a machine with four 12-core AMD Opteron 2.4 GHz CPUs. We carefully check the temperatures below which the 4 fs time step gives the same results as the 1 fs time step and do not include any 4 fs data that lead to noticeable differences in pressure, energy, or diffusion.

As a measure of the equilibration time, we define τ as the time at which $\sqrt{\langle r_{\mathrm{O}}(t)^2 \rangle} =$ 0.56 nm, i.e., the average time it requires for an O ion to move twice its diameter of 0.28 nm. Most simulations run for over $10\,\tau$, well beyond the time necessary for the system to reach equilibrium. For the range of temperatures and pressures considered here, the root mean squared displacement of the O ion is roughly 1.1–1.6 times that of the Si ion, this factor being the largest at low temperatures and low pressures.

An important structural feature is the coordination number of Si by O, since a tetrahedral network is defined by 4-coordination of the network centers. We calculate the Si coordination number by the usual method, integrating the Si-O radial distribution function up to the first minimum. For both models, and at all state points considered here (below 10 GPa), the coordination number lies between 4.0 and 4.9. The coordination number is the largest at high densities, and levels off to 4 when the density is decreased and the pressure becomes zero or negative.

4.3 Isochores of BKS and WAC silica

The most direct method of locating a critical point is to calculate the pressure P as a function of temperature T along different isochores. For fixed particle number N, constant volume V is also constant density. In a PT-diagram the isochores cross within the coexistence region and at the critical point. At those state points (at a given P and T) the system is a combination of two different phases with different densities. One can also locate a critical point by plotting the isotherms in a PV-diagram in order to determine the region in which the slope of the isotherms becomes zero (critical point) or negative (coexistence region). Because it is easier to determine whether two lines are crossing than whether a curve is flat, we study the isochores. Figure 4.2 shows the PT-diagrams with the isochores of BKS and WAC.

Both diagrams are qualitatively similar. There is a clear density anomaly to the left of the temperature of maximum density (TMD), and if we shift the temperature scale for BKS by approximately +4000 K, then the BKS isochores match those of WAC reasonably well. At very low P and high T the liquid phase is bounded by the liquid-gas (or liquid-vacuum) spinodal, and lowering P below the spinodal leads to spontaneous bubble formation. At very low T the diffusion coefficient drops rapidly and the liquid becomes a glass. Because the time it takes to equilibrate the system is inversely proportional to the rate of diffusion, simulations require too much time once the oxygen diffusion D_{O} drops below $\sim 10^{-8}$ cm^2/s, which is where the isochores stop in Fig. 4.2. For both models this limit is reached at a higher temperature for low P than for high P. This is caused by the diffusion anomaly (an increase in P leads to an *increase* in diffusion), which is present in both BKS and WAC models.

No crystallization was observed, unless the pressure was raised to values far

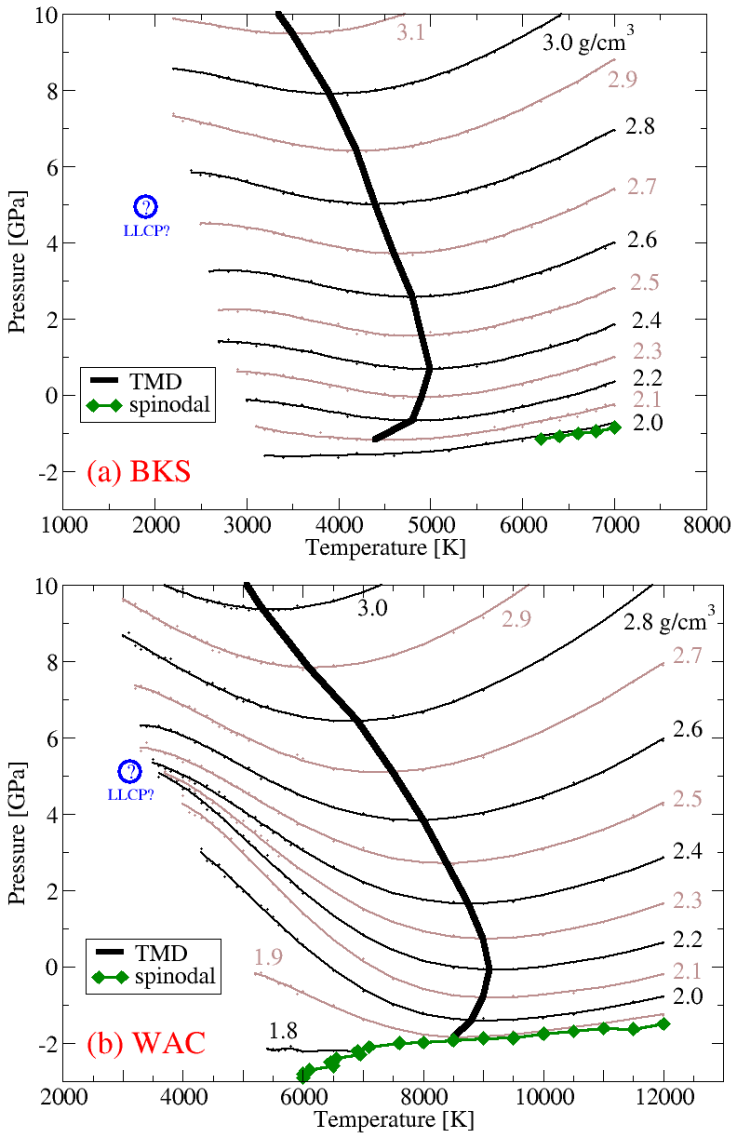

Figure 4.2: Isochores of liquid BKS silica (panel a) and liquid WAC silica (panel b). Thin black/brown lines are the isochores, the temperature of maximum density (TMD) is indicated by a thick black line, and green diamonds indicate part of the liquid-vacuum spinodal. Blue question marks indicate the approximate locations where a LLCP has been predicted by previous studies [160, 10]. The location of a LLCP can be identified by where the isochores cross. It seems a LLCP in BKS is unlikely, as the isochores do not approach each other. The isochores in WAC do approach each other, and might converge at the predicted point. However, at low temperatures the isochores near 2.3 g/cm^3 obtain a negative curvature. If this curvature becomes more negative as T goes down, then it is possible that the isochores will not cross below 3500 K. We conclude that for the temperatures currently accessible, the isochores alone are insufficient to demonstrate a LLCP in WAC.

outside the range of our detailed studies (e.g., above 40 GPa the WAC liquid spontaneously crystallizes into an 8-coordinated crystal). Normally, crystallization is readily detected by a rapid drift of the energy to lower values. However, when the diffusivity is very low (as in the present system, in the domain of greatest interest) the situation is different and crystal growth can be unobservably slow. More direct tests are then needed. In the present case we have sought information on crystal growth and melting by creating a crystal front (half simulation box of the liquid interfacing with half box of the topologically closest crystal) and have watched the crystal front receding at high temperature. However, the attempt to determine melting point by lowering the temperature and observing reversal of the interface motion, was unsuccessful because the growth rate became unobservably small (observed over microseconds) before any reversal was seen. We conclude that, since this crystal front was put in by hand, the possibility of crystallization by *spontaneous* nucleation (always the slowest step) followed by crystal growth, is undetectably small.

Based on the fitting and extrapolation of data, previous studies have predicted a liquid-liquid critical point (LLCP) in both WAC and BKS [160]. With the increase in computing power, and using the techniques to speed up the simulations discussed in Sec. 4.2, we are able to obtain data at lower temperatures than was previously possible. Our results for BKS (Fig. 4.2a) show that for $T > 2500$ K the isochores are nearly parallel, and therefore a LLCP in BKS is very unlikely. On the other hand, the isochores of the WAC model (Fig. 4.2b) show a more interesting behavior in that they clearly approach one another at low T in the vicinity of $P \approx 5$ GPa.

If we only consider the WAC isochores above 4000 K, then extrapolation would predict that the isochores cross around 3500 K and 5 GPa. However, below 4000 K we see that the isochores are starting to display a negative curvature in the PT-

plane. This signals an approach to a density minimum, which is the low-T boundary of the density anomaly region. The negative curvature makes it hard to perform an extrapolation that convincingly shows that the isochores cross at lower T. We can therefore only conclude that (for the temperatures currently accessible) the behavior of the isochores is insufficient to prove or disprove the existence of a LLCP in WAC.

4.4 Response functions of BKS and WAC silica

Upon approaching a critical point, the response functions diverge. Although true divergence occurs only in the thermodynamic limit $N \to \infty$, a large maximum should still be visible in response functions such as the isothermal compressibility K_T and the isobaric heat capacity C_P even when the box size is relatively small. Calculations using the Ising model and finite size scaling techniques applied to simulation results have shown that (for sufficiently large boxes) the location of the critical point is very close to where both K_T and C_P reach their global maximum [97, 106]. If a LLCP truly exists in WAC, then the PT-diagrams of C_P and K_T should show a large C_P maximum close to where K_T has a maximum—exactly where the isochores come together and where the LLCP has been predicted to be.

In order to construct isobaric response functions from a large set of constant-volume (NVT) data, some type of fit or interpolation is needed. For example, to calculate $C_P = (\partial H/\partial T)_P$ we consider the enthalpy H as a function of both P and T and fit the data $[P, T, H]$ with a smooth 3-dimensional surface $H(P, T)$. Abrupt changes in $H(P, T)$ lead to large spikes in its derivative $\partial H/\partial T$, and thus the $H(P, T)$ surface must be smooth if we are to obtain a meaningful C_P. Fitting a surface rather than a curve has the additional advantage that more data is taken into account, resulting in better statistics. An alternative approach is to calculate

C_P via fluctuations in H, but it has been shown [106] that first fitting $H(T)$ and then taking a derivative leads to cleaner results. It is of course easier to calculate C_P by doing constant-pressure (NPT) simulations instead, but then one would have the same problem with calculating C_V. We conclude that we can easily calculate all response functions if we apply a smooth surface fit $f(x, y)$ to a set of 3-dimensional points $z_k(x_k, y_k)$.

Fitting a surface to a set of points means striking a balance between the "smoothness" of the fit and the fitting error induced. One measure of smoothness is the Laplacian $\nabla^2 f$, since a small Laplacian means little change in the slope of $f(x, y)$, and thus a smoother function. Hence, to obtain a smooth surface fit $f(x, y)$ through the data points $z_k(x_k, y_k)$ with $k = 1, 2, \ldots, N$, we minimize

$$J = \sum_{k=1}^{N} w_k \left[f(x_k, y_k) - z_k \right]^2 + \iint \left| \nabla^2 f(x, y) \right|^2 dx\, dy. \tag{4.5}$$

The weights w_k provide the balance between the smoothness and the fitting error. If we set w_k too low, we obtain a very smooth fitting function $f(x, y)$ that poorly represents the data. If we set w_k too high, the function $f(x, y)$ will go through all the data points but will show large variations. Because large variations in the surface lead to even larger variations in the derivatives, the $H(P, T)$ surface must be very smooth when we calculate the C_P. Fortunately, introducing small fitting errors does not cause problems, because the simulation data already suffers from small statistical errors. If the underlying response function is in fact smooth, then it is possible to use the fitting errors to partially cancel the statistical errors.

Minimization of the functional J in Eq. 4.5 is not a new concept. For example, the CSAPS function in MATLAB applies a similar minimization scheme to calculate a cubic smoothing spline. As opposed to this MATLAB function, we do not impose

the constraint that $f(x, y)$ is a tensor product spline, but instead represent $f(x, y)$ by a set of 100×100 points (x_i, y_j, f_{ij}) placed on a regular grid (x_i, y_j). Bilinear interpolation is used to estimate the value of $f(x, y)$ between these grid points, and the derivatives and the Laplacian are calculated using finite (central) differences. To compensate for the reduced number of data points near the edges of the domain, we recommend that higher-order differences near the edges be used.

Figure 4.3 shows four response functions for WAC: (a) the isothermal compressibility K_T, (b) the isobaric heat capacity C_P, (c) the isobaric thermal expansivity α_P, and (d) the isochoric heat capacity C_V. These have been obtained using NVT simulations together with the smooth surface technique described above. To check the results generated by this technique, we determine whether the response functions satisfy the thermodynamic relation $VT\alpha_P^2/K_T + C_V - C_P = 0$. Because of statistical errors in the data we find slight deviations from zero, but these are less than 1 J/(mol K) in magnitude.

The compressibility K_T in Fig. 4.3a shows a clear global maximum near $P \approx 5$ GPa and $T \approx 4000$ K, because this is where the isochores in Fig. 4.2b are the closest together in terms of pressure. It is quite likely that below 4000 K this maximum increases further. If WAC has a LLCP then C_P should also have a maximum in that vicinity. However, Fig. 4.3b shows that this is not the case. There is clear global C_P maximum, but it is located near $P \approx 1$ GPa and $T \approx 6000$ K, which is far from the global K_T maximum. Therefore, based on the response functions, we conclude that WAC does not have a LLCP.

The isobaric thermal expansivity α_P (Fig. 4.3c) has a global minimum between the global maxima of C_P and K_T (Figs. 4.3a,b). This should come as no surprise, since $C_P \propto \langle(\Delta S)^2\rangle$ arises from fluctuations in entropy and $K_T \propto \langle(\Delta V)^2\rangle$ from volume fluctuations, while the expansivity $\alpha_P \propto \langle \Delta S \Delta V \rangle$ arises from a combination

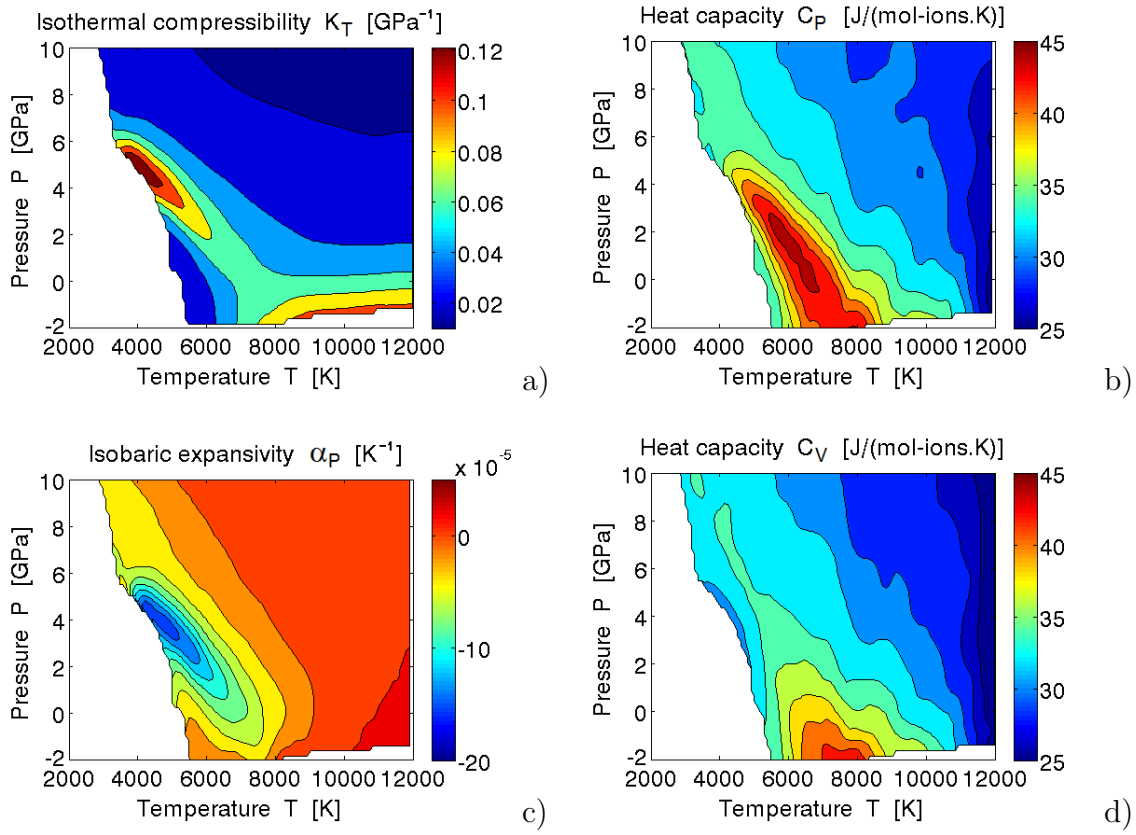

Figure 4.3: Response functions of WAC, from Ref. [105]. (a) The isothermal compressibility K_T is consistent with a LLCP near 5 GPa, 4000 K because near that point K_T has a global maximum. (b) The isobaric heat capacity C_P, however, has a global maximum around 1 GPa and 6000 K, far away from where K_T has its global maximum. This is inconsistent with the LLCP hypothesis. (c) The isobaric thermal expansivity α_P has its global minimum in between the global maxima of K_T and C_P. The contour line where $\alpha_P = 0$ corresponds to the location of the TMD. (d) The isochoric heat capacity C_V has its global maximum the furthest away from the global K_T maximum.

of both. Even though the global maxima occur at different places, the slopes dP/dT of the loci of local maxima are the same, so it seems likely they have a common origin. Because the system is not quite critical, the enthalpy fluctuations that determine the heat capacity can be statistically independent of the density fluctuations.

The variation of the heat capacity with temperature at constant pressure is shown over the temperature range in which the system remains in equilibrium, in Fig. 4.4. Figure 4.4b is basically a series of cross-sections of Fig. 4.3b. We note first that at moderately high pressures, 8 GPa, there is no difference between the WAC and BKS models. In each case the heat capacity reaches about 35 J/(K mol) before the diffusion becomes too slow that we can no longer equilibrate. This is 1.4 times the vibrational heat capacity of $3R \approx 25$ J/(K mol), as is typical of moderately fragile inorganic liquids (e.g. anorthite, $ZnCl_2$) right before ergodicity is broken [6, 71]. However, at pressures between zero and 5 GPa, a major difference is seen between the models.

Near the TMD we have $C_P \approx C_V$ (because the expansivity is very small) so we can compare data with C_V from Scheidler *et al.* [169] for the case of BKS at $P = 0$. The agreement is quantitative, up to the point where the earlier study was cut off. Our data confirms the existence of a peak in the equilibrium heat capacity—an unusual behavior that was not presented in Ref. [169] but had been noted in the earlier study of Saika-Voivod *et al.* [159] and was emphasized in Ref. [10].

Although BKS is far from having a critical point, the existence of this C_V maximum reveals the tendency of this system—which accords well with many aspects of experimental silica—to develop the same anomalous entropy fluctuations, and an analog of the Widom line made famous by water models.

For the WAC model (which approaches criticality much more closely than BKS does, as we have already seen in Fig. 4.2), this heat capacity peak becomes much

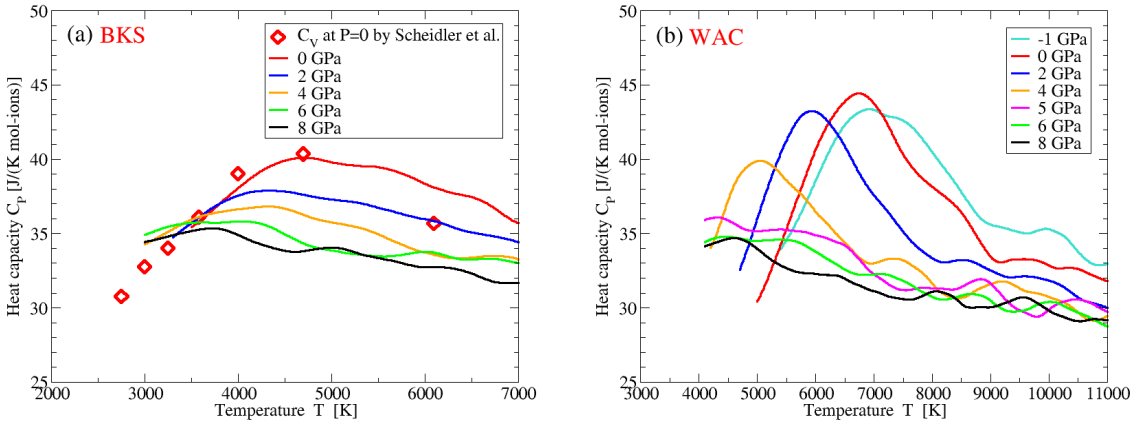

Figure 4.4: Comparison of the heat capacities of BKS (panel a) and WAC (panel b), obtained by calculating the smoothing spline of $H(T)$ at constant P, followed by taking its derivative (a slightly different method than was used in Fig. 4.3b). At 8 GPa there is no significant difference between the WAC and BKS models, but below 5 GPa WAC has a large maximum in the range 5000–8000 K (also clearly visible in Fig. 4.3b). In panel b we have included C_V data of Scheidler *et al.* [169] (red diamonds), which shows a maximum around 4500 K. Near the TMD (around 5000 K for $P = 0$) the expansivity is small, which means that $C_V \approx C_P$, in agreement with our results. For BKS this maximum is less clear in C_P, though still visible. Because of small fluctuations in the data, it is difficult to obtain a fit of $H(T)$ that produces a perfect estimate of $C_P = dH/dT$, leading to artificial oscillations in C_P. A larger data set would reduce this artifact. In addition, the smoothing spline method assumes zero curvature at the end-points of the data, and this leads to artifacts at very low T and very high T. For clarity, we have removed the parts of the curves below the temperature at which C_P starts to bend toward a constant a C_P value.

more prominent, reminiscent of the behavior of the Jagla model near its critical point. C_P reaches a value almost twice that of the vibrational component; behavior unseen in any previous inorganic system except for BeF_2 which is a WAC silica analog [71].

4.5 Tetrahedrality and bond angle stiffness

We find no LLCP in either model within the accessible temperature range, although it is closely approached in the case of the WAC potential near 4000 K and 5 GPa.

The isochores of BKS, which are the most direct indicators of criticality in a physical system, fail to converge into a critical point. In the case of WAC we cannot conclude anything from the isochores, but an analysis of the global extrema of the response functions indicates that there is no LLCP in WAC because the global C_P maximum and the global K_T maximum are significantly separated in the PT-plane.

Liquid silica forms a tetrahedral network of bonds, and below we will show that the lack of a LLCP is related to the openness of this network structure, which in turn is related to the stiffness of the inter-tetrahedral bond angles. In addition we will argue that criticality in WAC could be achieved with an adaptation of the pair potential.

The occurrence of a LLCP requires two competing liquid structures that can be in a (meta-stable) equilibrium with each other. In the case of a tetrahedral network-forming liquid the two relevant structures are usually: (i) a high-density collapsed structure that is highly diffusive, and (ii) a low-density open network structure that is more rigid, i.e., one that is still a liquid but less diffusive and more structured. Because the high-density structure occupies a smaller volume but has higher entropy (more disorder), the competition between these two structures is accompanied by a region with a density anomaly: $\alpha_P \propto \langle \Delta S \Delta V \rangle < 0$.

The high-density structure is very stable and is the dominant structure at high temperatures, but the low-density structure requires a more delicate balance of forces in order to be stable. If the bonds in the liquid are too flexible, the liquid collapses into the high-density structure. On the other hand, if the bonds are too rigid the liquid can no longer flow and becomes a glass.

There are several studies that address this situation. The 2006 study of Molinero *et al.* [132] shows how reducing the three-body repulsion parameter λ in the Stillinger-Weber potential [196] (which controls the bond angle stiffness) causes the

first order liquid-liquid phase transition of silicon ($\lambda = 21$) to disappear at $P = 0$ when $\lambda < 20.25$ (see Fig. 4.5). This transition occurs between a low-density liquid and a high-density liquid, where both liquids are metastable with respect to the diamond cubic (dc) crystal. Crystallization to the dc crystal always occurs from the low-density liquid. When $\lambda > 21.5$ crystallization happens so fast that it is no longer possible to accurately determine the temperature T_{LL} at which the phase transition occurs for $P = 0$.

Simulations of the Stillinger-Weber model indicate that the LLCP for $\lambda = 21$ is located at -0.60 GPa and 1120 K [208]. Since each value of λ defines a unique system with a unique critical pressure, the vanishing of the liquid-liquid transition at $\lambda < 20.25$ implies that this is the λ value for which the LLCP is at $P = 0$. Isochore-crossing studies conducted elsewhere [89] show that this is indeed the case, with $T_c \approx 700$ K for $P_c = 0$. It is clear that decreasing λ means decreasing the tetrahedrality and increasing density. When $\lambda < 20.25$ the LLCP shifts to positive pressures, and therefore the phase transition line can no longer be seen in Fig. 4.5, as it only considers $P = 0$. We thus lack the information to determine exactly for which λ there is no LLCP at *any* pressure, but it is certain that this happens at some value $\lambda > 0$, since in the most extreme case of $\lambda = 0$ we are left with a simple Lennard-Jones-like model that has no LLCP.

That weakening the tetrahedrality (i.e., making the tetrahedral bonds more flexible) leads to the removal of a LLCP, was also shown in 2012 by Tu and co-authors using a different monatomic model [207]. The Hamiltonian of this model includes a term that lowers the energy when particles are aligned along near-tetrahedral angles and thus favors a diamond cubic ground state. The study of Ref. [207] considers two versions: one that allows broad flexibility of the inter-tetrahedral bond angles (leading to weak tetrahedrality), and another in which the bond angle is more constrained

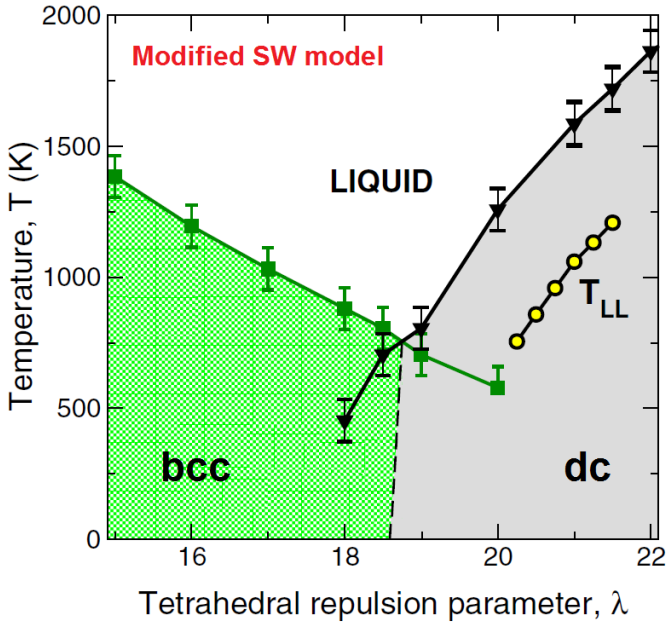

Figure 4.5: Phase diagram of the modified Stillinger-Weber potential in terms of the tetrahedral repulsion parameter λ and temperature T, at zero pressure (figure adapted from [132]). The black triangles indicate the melting line of the diamond cubic (dc) crystal, while the green squares denote the melting line of the bcc crystal. The dashed line separates the dc and bcc regions. Yellow circles indicate the transition temperature T_{LL} at which the liquid-liquid phase transition line crosses the $P = 0$ isobar for that particular value of λ. Silicon is represented by $\lambda = 21$ and has a liquid-liquid critical point at -0.60 GPa [208], and therefore all LLCPs for $\lambda > 20.25$ lie at negative pressures (there is a LLCP for each value of λ). For $\lambda < 20.25$ the LLCPs are at positive pressures and therefore the phase transition line can no longer be seen in this diagram. When λ is large the system easily crystallizes, and therefore the phase transition line at $P = 0$ can no longer be accurately located when $\lambda > 21.5$.

(giving rise to strong tetrahedrality).

The behavior for strong tetrahedrality is shown in Fig. 4.6, and we see that the isochores converge into a critical point. If the tetrahedrality is weakened slightly, then the isochores separate, the LLCP disappears, and the diagram starts to resemble that of Fig. 4.2b for WAC. It should be mentioned that a separation of the global C_P and K_T maxima also occurs in the weak tetrahedrality version (as is the case for WAC), while the C_P and K_T maxima are close together and near the LLCP in the strong version of the model.

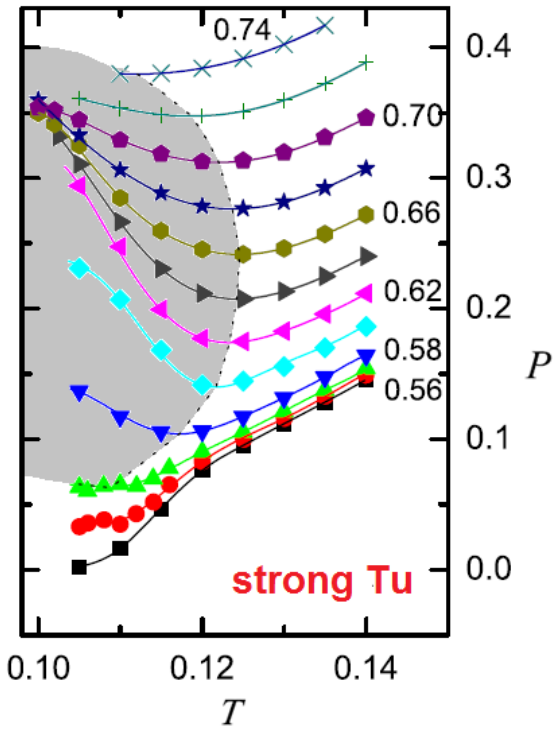

Figure 4.6: Isochores of the Tu model for the strong tetrahedrality version, which has a LLCP (figure adapted from Ref. [207]). Gray area indicates the density anomaly region. By reducing the tetrahedrality, the Tu model can be smoothly changed into the weak tetrahedrality version, which does not have a LLCP. The isochores of WAC (Fig. 4.2b) show no LLCP but closely resembles that of the strong Tu model. We can interpret this as that WAC is *close* to having a LLCP, but not close enough. If we were to enhance the tetrahedrality of WAC, it is likely a LLCP would appear.

Finally we should consider the simulations done on "patchy" colloids by Sciortino and coworkers. Using the Kern-Frenkel (KF) model [95] (which consists of particles with tetrahedrally arranged sticky points), these authors demonstrated that the colloids developed tetrahedral network topologies, with each particle being surrounded by four others—which is not itself surprising. More interesting was the finding that, when the effective sizes of the patches were varied, conditions could be found in which not only were the relaxation kinetics strictly Arrhenius in form, but also the amorphous state became the free energy ground state of the system, over a wide range of densities [178]. This corresponds to a more dramatic stabilization of the amorphous state than the kinetic stability observed in our work. It signifies an absolute stability against crystallization on any time scale, i.e., the system has become an "ideal glassformer" [90].

Studies with the KF model have also demonstrated that highly directional bonds are needed to observe spontaneous crystallization in tetrahedral interacting particles [155], in agreement with the results found by Molinero *et al.* using the Stillinger-Weber family of potentials. Since the KF colloids can be used to describe different tetrahedral models, they promote our understanding of tetrahedral liquids such as ST2 and mW water, Stilling-Weber silicon, and BKS silica. Surprisingly, there exists a mapping from these models to the KF model, using only a single parameter: the patch width [161]. The patch width is related to the flexibility of the bonds between the particles, and it is therefore likely that spontaneous crystallization and the existence of a LLCP are related to bond angle flexibility.

All of these studies show that the occurrence of a LLCP becomes less likely when the parameters controlling tetrahedrality are weakened. Unfortunately, the BKS and WAC models do not have an explicit parameter that controls tetrahedrality, such as the parameter λ in the Stillinger-Weber model. In this model there is a

direct relation between the value of λ and the tetrahedrality of the liquid measured by the orientational order parameter q as defined by Errington and Debenedetti [48]. This parameter is constructed such that its average value $\langle q \rangle$ will equal zero if all atoms are randomly distributed within the liquid, while $q = 1$ for each atom within a perfect tetrahedral network (such as in a cubic diamond lattice). For silica the situation is more complicated. It is not immediately clear how to define the tetrahedrality of a system that consists of two types of atoms. One way would be to find for each Si atom its four nearest neighboring Si atoms and compute $\langle q \rangle$ for this subset of atoms. However, this measure would completely ignore the positions of the O atoms which form ionic bridges between the Si atoms. Since the O-Si-O bond angle deviates very little from the perfect tetrahedral angle of 109° [212], it makes sense to focus on the inter-tetrahedral Si-O-Si bond angle instead. It is commonly agreed that structures such as diamond cubic have maximum tetrahedrality, and for silica this corresponds to a system where all Si-O-Si bond angles are equal to 180° (such as β-cristobalite). How much the inter-tetrahedral Si-O-Si bond angles differ from 180° can thus be employed as a measure of the tetrahedrality, and we have therefore calculated this bond angle distribution for both BKS and WAC. The location of the maximum in the Si-O-Si bond angle distribution (i.e., the most probable angle) is a parameter that one could use to quantify the tetrahedrality. If we denote the most probable angle at the lowest accessible temperature (T_g) as $\theta_{\max}$, then the tetrahedrality parameter t can be defined as $t \equiv \theta_{\max}/180°$, where $0 < t < 1$. Since the "openness" of the structure will increase with the average Si-O-Si angle, one could also define the tetrahedrality using the volume ratio, i.e., $t \equiv V^*/V_{\mathrm{dc}}$, which would require much less effort to calculate. Here V_{dc} is the volume of the perfect diamond cubic and V^* is the system volume at some corresponding state, for instance at the TMD (which is less arbitrary than T_g).

Let us consider the angular relations and the mechanical forces that determine them in more detail. In terms of the familiar ball-and-stick model, the Si-O-Si bond could be represented by two sticks connected at the oxygen atom, with a spring in between the sticks. This spring constrains the bond angle to some preferred bond angle θ_0, while the value of its spring constant k_2 (the *stiffness*) dictates how flexible the bond angle is. From the bond angle probability distribution $\mathcal{P}(\theta)$, it is possible to estimate the values of the preferred bond angle θ_0 and the bond angle stiffness k_2.

To extract the Si-O-Si bond angles from the data, we consider each O ion together with its two nearest Si neighbors and calculate the angle between the two Si-O bonds. In Fig. 4.7 we show the resulting probability distributions $\mathcal{P}(\theta)$ of the Si-O-Si angle θ for BKS and WAC at zero pressure. These curves have been measured before in previous studies [212, 72] but with less detail. As the temperature decreases, the width of the distribution decreases and the maximum shifts toward 180°. This implies that the liquid becomes more structured and stiffer. This is to be expected, since at a high temperatures there are more thermal fluctuations and therefore $\mathcal{P}(\theta)$ has a broader distribution.

Plotting $\mathcal{P}(\theta)$ may not be the best way of presenting the bond angle distribution, as this distribution is biased toward 90° angles. This is particularly clear from the distribution of the vapor (the thin black line in Fig. 4.7a). The ions in the vapor have no preferred position with respect to their neighbors, yet $\mathcal{P}(\theta)$ is not uniform but proportional to $\sin\theta$. This is related to the fact that the infinitesimal area element of the unit sphere is $dA = \sin\theta\, d\theta\, d\phi$ rather than $d\theta\, d\phi$. As $\theta \to 180°$ the area element dA approaches zero, and therefore $\mathcal{P}(\theta) = 0$ at $\theta = 180°$. Instead of $\mathcal{P}(\theta)$ it is better to consider the probability distribution $\mathcal{P}(\cos\theta) = \mathcal{P}(\theta)/\sin\theta$, as is shown in the insets of Fig. 4.7. The $\mathcal{P}(\cos\theta)$ distribution of the vapor is a

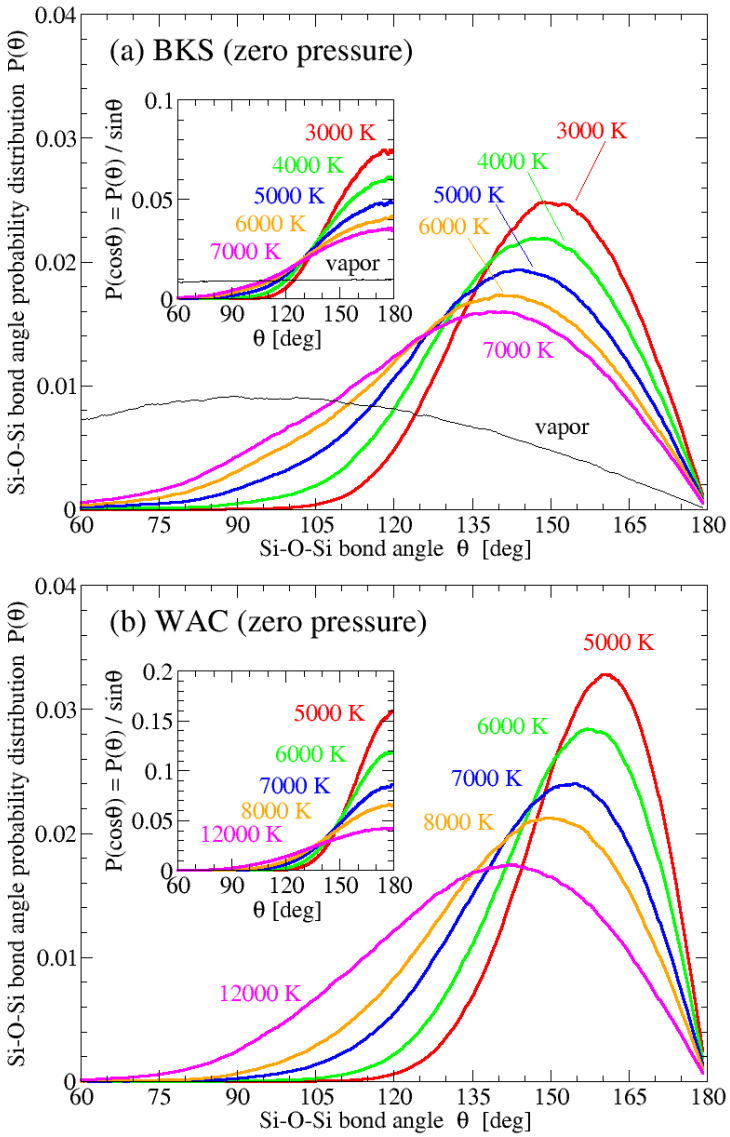

Figure 4.7: Probability distribution of the Si-O-Si bond angle $\mathcal{P}(\theta)$ in liquid silica for (a) the BKS model and (b) the WAC model. As T goes down, the most probable angle moves closer to 180° while simultaneously the width of the distribution decreases. The first phenomenon causes the liquid to expand upon cooling, while a reduction in width means that the bonds become stiffer, which leads to a decrease in diffusion. Both phenomena are related (see below) and are much stronger for WAC than for BKS. Instead of $\mathcal{P}(\theta)$ it is better to consider $\mathcal{P}(\cos\theta) = \mathcal{P}(\theta)/\sin\theta$, since a completely random distribution such as in the vapor has $\mathcal{P}(\theta) \propto \sin\theta$ while $\mathcal{P}(\cos\theta)$ is uniform (see inset of panel a). For both models and all temperatures $\mathcal{P}(\cos\theta)$ resembles a normal distribution with mean 180°. This indicates that the preferred angle is in fact 180°, and that the width of $\mathcal{P}(\cos\theta)$ determines both the location of the peak in $\mathcal{P}(\theta)$ as well as its width.

uniform distribution (inset of Fig. 4.7a). For the liquid, the distribution $\mathcal{P}(\cos\theta)$ is approximately a normal distribution with its mean at $\theta_0 = 180°$. Evidently the most probable inter-tetrahedral angle (the location of the $\mathcal{P}(\theta)$-peak) is purely an effect of the width of this normal distribution combined with the fact that $dA \propto \sin\theta$.

It is possible to interpret the bond angle distribution in terms of an effective potential $U_{\text{eff}}(\theta)$, assuming that $\mathcal{P}(\cos\theta) \propto \exp[-U_{\text{eff}}(\theta)/k_BT]$. When the effective potential is harmonic, i.e. $U_{\text{eff}} = \frac{1}{2}k_2(\theta - \theta_0)^2$, the resulting probability distribution is a normal distribution with mean θ_0 and a width that depends on temperature T and stiffness k_2. In general the effective potential will not be perfectly harmonic and includes anharmonic terms. Because $\cos\theta$ is an even function about $\theta = 180°$, it is required that $\mathcal{P}(\cos\theta)$ is as well, and therefore also $U_{\text{eff}}(\theta)$. Consequently, the leading-order anharmonic term in $U_{\text{eff}}(\theta)$ is of the fourth order. The Si-O-Si bond angle distribution can thus be described by

$$\mathcal{P}(\theta) = A \sin\theta \exp[-U_{\text{eff}}(\theta)/k_BT] \tag{4.6}$$

with U_{eff} a Taylor series about the mean angle $\theta_0 = 180°$,

$$U_{\text{eff}}(\theta) = \frac{1}{2}k_2(\theta - \theta_0)^2 + \frac{1}{4!}k_4(\theta - \theta_0)^4 + \ldots \tag{4.7}$$

Here A is a temperature-dependent normalization constant that ensures that the total probability $\int \mathcal{P}(\theta)\, d\theta = \int \mathcal{P}(\cos\theta)\, d\cos\theta$ is equal to one, and k_B is the Boltzmann constant.

The probability distributions of Fig. 4.7 can be fitted quite well with Eqs. 4.6 and 4.7, even when the sixth power and higher-order terms are ignored. The resulting values for the stiffness k_2 are shown in Fig. 4.8. It is immediately clear that WAC is

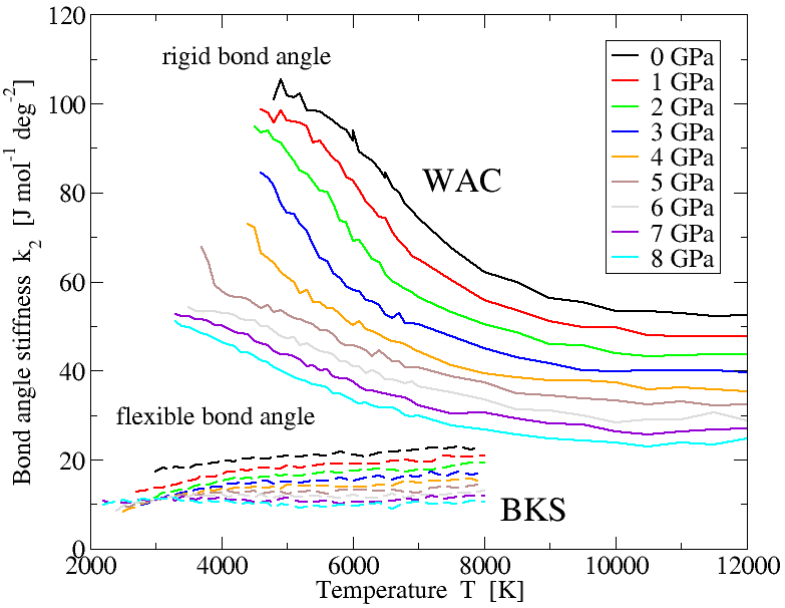

Figure 4.8: Stiffness of the Si-O-Si bond angle for both WAC (solid lines, top) and BKS (dashed lines, bottom). For both models the stiffness k_2 goes down with increasing pressure. It is clear that BKS has more flexible bonds (small k_2), and that WAC is more rigid (large k_2) and therefore "more tetrahedral". In addition WAC shows a transition at low T for $P \leq 5$ GPa to a state with an even higher stiffness.

far more rigid than BKS. For BKS the stiffness does not vary much with temperature, while increasing the pressure makes the bonds slightly less stiff. The same is true for WAC at high T, but below 5 GPa the stiffness shows an increase when the liquid is cooled. This increase is exactly where C_P has its maximum in Fig. 4.3b, and thus we may argue that the increase in C_P is due to a structural change, namely the stiffening of the tetrahedral network.

From the isochores in Fig. 4.2b it is clear that WAC is very close to having a LLCP. If we compare the results of previous studies done on tetrahedral liquids [132, 207] with our results for BKS and WAC, then we see that the tetrahedrality of BKS is far too small (i.e., the inter-tetrahedral bond angles are not sufficiently stiff) to have a LLCP, and that WAC is close, but not close enough. However, it might be possible

to make a small change to the WAC potential to enhance its tetrahedrality. One simple way to achieve this would be to add a repulsive term similar to the three-body interaction of the Stillinger-Weber model. This term should penalize any Si-O-Si configuration with an angle less than 180° with a repulsive energy determined by the intensity parameter λ and the size of the deviation. The λ value associated with this interaction should be carefully chosen; if λ is too small no LLCP will arise, while applying a λ that is too large will likely lead to crystallization into a diamond (β-cristobalite) structure. It would be interesting to see at what value of k_2 this criticality is introduced, and if this value is the same across other tetrahedral models as well, but this is beyond the scope of the present project.

The results presented here are also relevant to the possible existence of a LLCP in different water models, and highlight the importance of a thorough analysis of the O-H-O bond angle distribution. Such an analysis, possibly with the use of a bond angle stiffness parameter such as k_2, might be able to predict if a particular water model will have a LLCP. Unfortunately, to the best of our knowledge, it is currently not possible to measure these angles directly in experiments, as significant help from computer simulations is required to obtain the angular structure of liquid water [176, 180].

4.6 Conclusion

Although it has been suggested, based on a combination of simulation and theoretical considerations [160], that both BKS and WAC have LLCPs at temperatures beyond the accessible simulation range, our study suggests that neither BKS nor WAC can reach a critical point. We have compared our results to those of other tetrahedral models [132, 207], analyzed the bond angle distributions, and conclude

that the lack of a LLCP in both BKS and WAC is due to a lack of stiffness in the inter-tetrahedral Si-O-Si bond angles. WAC is close to criticality, but BKS shows little sign of a LLCP, and since the latter is considered to be the more realistic model for experimental silica, we expect that no LLCP occurs in real silica either.

However, this does not mean that manifestations of criticality can never be observed. As Chatterjee and Debenedetti [40] have shown theoretically, even a weak tendency toward criticality (as in BKS) can be amplified into a liquid-liquid phase separation in a binary system. Indeed this notion has been exploited elsewhere [12] to interpret the (much-studied [37, 38, 39, 61, 47, 66, 133] but incompletely understood) splitting out of an almost pure SiO_2 phase from such simple systems as the Na_2O-SiO_2 and Li_2O-SiO_2 binary glasses during supercooling.

CHAPTER 5: Conclusions and outlook

In this thesis we have considered several liquid anomalies, the relationships between them, as well as the phenomenon of liquid-liquid phase transitions that in some cases ends in a liquid-liquid critical point. Of particular interest is liquid water, H_2O. Apart from being fundamentally important in many fields such as biology, chemistry, and physics, this tiny molecule gives rise to a complex liquid with many properties that are remarkably different from those of simple liquids. In the first chapter we have presented a small subset of water-like anomalies which were subsequently investigated in detail in the second chapter using simple models.

The density anomaly (a region where the liquid *expands* upon cooling, i.e. where $\alpha_P = \frac{1}{V}(\partial V/\partial T)_P < 0$) can be attributed to the existence of two competing length scales. Sometimes these length scales are explicit, as in simple potentials such as the hard-core linear ramp model (HCLR) or the Jagla potential. But in more realistic atomic liquids these length scales are often more abstract, although the length scales can still be observed in terms of the structure of the liquid, and can therefore be studied with the radial distribution function $g(r)$ or the structure factor $S(k)$. For these liquids the two competing length scales are expressed in the form of two structures: an expanded structure characterized by large open spaces between the particles, and a collapsed structure in which the particles are spaced more closely. In the case of water these two competing structures are caused by hydrogen bonding. When two water molecules form a hydrogen bond, their energy is reduced but at the expense of an increase in volume. Alternatively, two molecules can choose to be closer together, but this would require them to occupy a higher energy state. The competition arises from the fact that the liquid tries to minimize the Gibbs energy $G = E + PV - TS$, and thus (assuming the entropy is comparable for both

structures), both states have approximately the same Gibbs energy.

The notion of two competing length scales also explains the diffusion anomaly (i.e. an increase of pressure leads to an *increase* in diffusion). One way to look at this is with the Maxwell relation $\partial V/\partial T = -\partial S/\partial P$. When there is a density anomaly ($\partial V/\partial T < 0$) then $\partial S/\partial P > 0$ which means that an increase in pressure leads to an increase of the entropy. An increase in entropy means more disorder, and thus an increase in diffusion.

Using similar arguments, we explained in Chapters 1 and 2 how the melting line can have a negative slope, as does the hexagonal ice melting line in water. In particular, when it is known that the crystal has a lower density than the liquid, then the Clapeyron relation $dP/dT = \Delta S/\Delta V$ (Eq. 1.8) demands that the melting line will have a negative slope. The liquid is always more disordered than the crystal (so $\Delta S \equiv S_{\text{liquid}} - S_{\text{crystal}} > 0$ always), and therefore when $\Delta V \equiv V_{\text{liquid}} - V_{\text{crystal}} < 0$ we find that the slope of the melting line is negative: $dP/dT < 0$.

The existence of an expanded structure that can collapse is responsible for the compressibility anomaly (K_T goes down upon heating, i.e. the liquid becomes more stiff). As the cut-ramp potential of Sec. 2.4.3 made clear, the two length scales do not need to compete in order to have a compressibility anomaly, and in this regard the compressibility anomaly is different from the other water-like anomalies.

When a liquid has two competing length scales (or equivalently, two competing structures) then it is sometimes possible to have those structures form two separate phases. The result is the emergence of a phase transition between two liquids, a low-density liquid (LDL) and a high-density liquid (HDL), with possibly a liquid-liquid critical point (LLCP). This is most evident in the Jagla potential (Sec. 2.3), which displays both a LLCP and water-like anomalies. The potential has two competing length scales (causing the anomalies), and an attractive tail which induces the criti-

cal point. Without the attractive tail LDL droplets cannot coalesce with other LDL droplets (and similarly for HDL with HDL), resulting in a mixture of locally-LDL and locally-HDL, but without a phase transition. However, even if a liquid has a LLCP, this does not necessarily mean there are anomalies. The existence of two length scales is a necessity for the phase transition, but in order to have anomalies, these are required to *compete*. One example of such a model is the square shoulder potential (Sec. 2.5).

It can be quite difficult to prove the existence of a LLCP, as was made clear in Chapter 3 for ST2 water. Several techniques, however, are available to confirm the presence of a LLCP. First of all, it is important to identify and quantify the difference in structure between LDL and HDL, using e.g. the radial distribution function $g(r)$ or the structure factor $S(k)$. Secondly, one must show that the two liquids are indeed metastable with respect to the stable crystalline state, as was done in Sec. 3.7 where we considered the growth and subsequent melting of crystal nuclei. Lastly, because liquid-liquid critical points belongs to the same universality class as the 3D Ising model, it is possible to directly compare the order parameter distribution function of the liquid with that of the 3D Ising model (Sec. 3.8). This, together with finite size scaling of the Challa-Landau-Binder parameter, provides a powerful technique to demonstrate the existence of a LLCP and allows for an accurate estimate of its location.

As was made clear in Chapter 4, it is often easier to rule out the existence of a LLCP than prove its existence. Since the isochores must cross at the critical point, if they fail to do so, this is a clear indicator that no LLCP exists. With this method a LLCP is immediately ruled out for BKS silica (considered to be an accurate model for real SiO_2). In addition to the isochores, also an analysis of response function maxima can be employed. At a critical point all response functions diverge, which is

visible as large maxima in finite systems. The compressibility K_T acquires its largest maximum exactly where the isochores come closest together, with a diverging K_T being equivalent to a crossing of the isochores. It is important to check that other response functions, such as the isobaric heat capacity C_P, acquire their maximum at the same state point. In the WAC silica model, for example, both response functions displayed large maxima, but at different pressures—indicating that WAC does not have a LLCP although it comes closer to having one than BKS does.

Since BKS is very far from having a LLCP, and WAC very close, these two systems together provide insight to what dictates whether a liquid has a LLCP or not. In Chapter 4 we compared both silica models with several other tetrahedral models, and concluded that "tetrahedrality" is the dominant quantity to consider. Liquids with weak tetrahedrality tend to behave like a normal liquid, but as one increases the tetrahedral structure of the liquid a LLCP might arise. If the tetrahedrality is increased too much, at low T the liquid becomes unstable with respect to the diamond cubic lattice (the perfect tetrahedral structure) and crystallization will occur before a liquid-liquid transition can be witnessed.

There exist several different parameters to quantify the amount of tetrahedrality, depending on the liquid and the model. One promising parameter might be the "bond angle stiffness" k_2, introduced in Chapter 4 based on the O-Si-O bond angles. More flexible bond angles seem to be correlated to the lack of a critical point, and therefore this flexibility might be able to predict the existence of a LLCP, even at temperatures far higher than the critical temperature T_c. Considering this, it makes sense for liquid silica not to have a LLCP, as the tetrahedral bonds in silica are a lot more flexible than for instance the hydrogen bonds in water.

Future work could focus on the development of new models with an adjustable tetrahedrality, similar to the Stillinger-Weber family of models investigated by Mo-

linero *et al.* [132] (see Sec. 4.5). This should make it possible to confirm that the tetrahedrality is the main predictor for the existence of a LLCP, as well as determine which tetrahedrality parameter is the most suitable to use for this prediction.

BIBLIOGRAPHY

[1] S. Aasland and P. F. McMillan, *Nature (London)* **369**, 633 (1994).

[2] J. L. F. Abascal and C. Vega, *Journal of Chemical Physics* **133**, 234502 (2010).

[3] J. L. F. Abascal and C. Vega, *Journal of Chemical Physics* **134**, 186101 (2011).

[4] M. P. Allen and D. J. Tildesley, *Computer Simulation of Liquids*, Oxford Science Publications, 1987.

[5] P. W. Anderson, *Science* **267**, 1610 (1995).

[6] C. A. Angell, *Journal of Non-Crystalline Solids* **73**, 1 (1985).

[7] C. A. Angell, *Journal of Physics: Condensed Matter* **12**, 6463 (2000).

[8] C. A. Angell, *MRS bulletin / Materials Research Society* **33**, 544 (2008).

[9] C. A. Angell, P. A. Cheeseman, and S. Tamaddon, *Science* **218**, 885 (1982).

[10] C. A. Angell and M. Hemmati, "Glass Transitions and Critical Points in Orientationally Disordered Crystals and Structural Glassformers: ("Strong" Liquids are More Interesting Than We Thought)", in: *4th International Symposium on Slow Dynamics in Complex Systems*, ed. by M. Tokuyama and I. Oppenheim, vol. 1518, AIP Conf. Proc., Dec. 2013, p. 9.

[11] C. A. Angell, K. L. Ngai, G. B. McKenna, P. F. McMillan, and S. W. Martin, *Journal of Applied Physics* **88**, 3113 (2000).

[12] C. A. Angell, P. H. Poole, and M. Hemmati, "A New Interpretation of Liquid-Liquid Unmixing in Classical Alkali Silicate Glasses", in: *Proceedings of 12th East European Glass Conference (Varna, Bulgaria)*, ed. by B. Samunova and Y. Demetriew, Sept. 1996, pp. 100–109.

[13] C. A. Angell, J. Shuppert, and J. C. Tucker, *Journal of Physical Chemistry* **77**, 3092 (1973).

[14] C. A. Angell, W. J. Sichina, and M. Oguni, *Journal of Physical Chemistry* **86**, 998 (1982).

[15] G. G. N. Angilella, F. E. Leys, N. H. March, and R. Pucci, *Physics and Chemistry of Liquids* **41**, 211 (2003).

[16] N. M. Barraz, E. Salcedo, and M. C. Barbosa, *Journal of Chemical Physics* **131**, 094504 (2009).

[17] B. W. H. van Beest, G. J. Kramer, and R. A. van Santen, *Physical Review Letters* **64**, 1955 (1990).

[18] H. J. C. Berendsen, J. P. M. Postma, W. F. van Gunsteren, A. DiNola, and J. R. Haak, *Journal of Chemical Physics* **81**, 3684 (1984).

[19] M. H. Bhat, V. Molinero, E. Soignard, V. C. Solomon, S. Sastry, J. L. Yarger, and C. A. Angell, *Nature (London)* **448**, 787 (2007).

[20] V. Bianco and G. Franzese, *arXiv:cond-mat.soft* 1212.2847 (2012).

[21] V. Bianco, S. Iskrov, and G. Franzese, *Journal of Biological Physics* **38**, 27 (2012).

[22] B. Boates and S. A. Bonev, *Physical Review Letters* **102**, 015701 (2009).

[23] S. A. Bonev, E. Schwegler, T. Ogitsu, and G. Galli, *Nature (London)* **431**, 669 (2004).

[24] L. Bosio, S.-H. Chen, and J. Teixeira, *Physical Review A* **27**, 1468 (1983).

[25] A. Botti, F. Bruni, A. Isopo, M. A. Ricci, and A. K. Soper, *Journal of Chemical Physics* **117**, 6196 (2002).

[26] V. V. Brazhkin, R. N. Voloshin, S. V. Popova, and A. G. Umnov, *Journal of Physics: Condensed Matter* **4**, 1419 (1992).

[27] P. Brüggeller and E. Mayer, *Nature (London)* **288**, 569 (1980).

[28] R. A. Buckingham, *Proceedings of the Royal Society A* **168**, 264 (1938).

[29] S. V. Buldyrev, G. Franzese, N. Giovambattista, G. Malescio, M. R. Sadr-Lahijany, A. Scala, A. Skibinsky, and H. E. Stanley, *Physica A* **304**, 23 (2002).

[30] S. V. Buldyrev and H. E. Stanley, *Physica A* **330**, 124 (2003).

[31] E. F. Burton and W. F. Oliver, *Proceedings of the Royal Society A* **153**, 166 (1935).

[32] G. Bussi, D. Donadio, and M. Parrinello, *Journal of Chemical Physics* **126**, 014101 (2007).

[33] P. J. Camp, *Physical Review E* **68**, 061506 (2003).

[34] P. J. Camp, *Physical Review E* **71**, 031507 (2005).

[35] M. Canpolat, F. W. Starr, M. R. Sadr-Lahijany, A. Scala, O. Mishima, S. Havlin, and H. E. Stanley, *Chemical Physics Letters* **294**, 9 (1998).

[36] M. S. S. Challa, D. P. Landau, and K. Binder, *Physical Review B* **34**, 1841 (1986).

[37] R. J. Charles, *Journal of the American Ceramic Society* **49**, 55 (1966).

[38] R. J. Charles, *Journal of the American Ceramic Society* **50**, 631 (1967).

[39] R. J. Charles, *Physics and Chemistry of Glasses* **10**, 169 (1969).

[40] S. Chatterjee and P. G. Debenedetti, *Journal of Chemical Physics* **124**, 154503 (2006).

[41] C. H. Cho, S. Singh, and G. W. Robinson, *Physical Review Letters* **76**, 1651 (1996).

[42] C. H. Cho, S. Singh, and G. W. Robinson, *Faraday Discussions – Royal Society of Chemistry* **103**, 19 (1996).

[43] D. Corradini, M. Rovere, and P. Gallo, *Journal of Chemical Physics* **132**, 134508 (2010).

[44] P. G. Debenedetti, V. S. Raghavan, and S. S. Borick, *Journal of Physical Chemistry* **95**, 4540 (1991).

[45] P. G. Debenedetti and H. E. Stanley, *Physics Today* **56**, 40 (2003).

[46] P. G. Debenedetti and F. H. Stillinger, *Nature (London)* **410**, 259 (2001).

[47] R. H. Doremus, *Glass Science*, Wiley, New York, 1973.

[48] J. R. Errington and P. G. Debenedetti, *Nature (London)* **409**, 318 (2001).

[49] G. Franzese, K. Stokely, X. Q. Chu, P. Kumar, M. G. Mazza, S. H. Chen, and H. E. Stanley, *Journal of Physics: Condensed Matter* **20**, 494210 (2008).

[50] G. Franzese, *Physical Review E* **61**, 6383 (2000).

[51] G. Franzese, *Journal of Molecular Liquids* **136**, 267 (2007).

[52] G. Franzese, V. Bianco, and S. Iskrov, *Food Biophysics* **6**, 186 (2011).

[53] G. Franzese, V. Cataudella, S. E. Korshunov, and R. Fazio, *Physical Review B* **62**, R9287 (2000).

[54] G. Franzese and A. Coniglio, *Physical Review E* **58**, 2753 (1998).

[55] G. Franzese, A. Hernando-Martínez, P. Kumar, M. G. Mazza, K. Stokely, E. G. Strekalova, F. de los Santos, and H. E. Stanley, *Journal of Physics: Condensed Matter* **22**, 284103 (2010).

[56] G. Franzese, G. Malescio, A. Skibinsky, S. V. Buldyrev, and H. E. Stanley, *Nature (London)* **409**, 692 (2001).

[57] G. Franzese, G. Malescio, A. Skibinsky, S. V. Buldyrev, and H. E. Stanley, *Physical Review E* **66**, 051206 (2002).

[58] G. Franzese, M. I. Marqués, and H. E. Stanley, *Physical Review E* **67**, 011103 (2003).

[59] G. Franzese and F. de los Santos, *Journal of Physics: Condensed Matter* **21**, 504107 (2009).

[60] G. Franzese and H. E. Stanley, *Journal of Physics: Condensed Matter* **19**, 205126 (2007).

[61] F. Y. Galakhov and B. G. Varshal, "Causes of phase separation in simple silicate systems", in: *Phase-Separation Phenomena in Glasses*, ed. by E. A. Porai-Koshits, vol. 8, The Structure of Glass, Consultants Bureau, New York, 1973, pp. 7–11.

[62] P. Gallo and F. Sciortino, *Physical Review Letters* **109**, 177801 (2012).

[63] P. Gallo, F. Sciortino, P. Tartaglia, and S.-H. Chen, *Physical Review Letters* **76**, 2730 (1996).

[64] L. M. Ghiringhelli, C. Valeriani, J. H. Los, E. J. Meijer, A. Fasolino, and D. Frenkel, *Molecular Physics* **106**, 2011 (2008).

[65] H. M. Gibson and N. B. Wilding, *Physical Review E* **73**, 061507 (2006).

[66] W. Haller, D. H. Blackburn, and J. H. Simmons, *Journal of the American Ceramic Society* **57**, 120 (1974).

[67] S. Harrington, P. H. Poole, F. Sciortino, and H. E. Stanley, *Journal of Chemical Physics* **107**, 7443 (1997).

[68] K. R. Harris and P. J. Newitt, *Journal of Chemical & Engineering Data* **42**, 346 (1997).

[69] W. M. Haynes, T. J. Bruno, and D. R. Lide, eds., *CRC Handbook of Chemistry and Physics (Internet Version 2014)*, 94th ed., CRC Press: Boca Raton, FL, 2014.

[70] M. Hemmati and C. A. Angell, *Journal of Non-Crystalline Solids* **217**, 236 (1997).

[71] M. Hemmati, C. T. Moynihan, and C. A. Angell, *Journal of Chemical Physics* **115**, 6663 (2001).

[72] M. Hemmatti and C. A. Angell, "Comparison of Pair Potential Models for the Simulation of Liquid SiO2: Thermodynamic, Angular-Distribution, and Diffusional Properties", in: *Physics Meets Mineralogy: Condensed Matter Physics in the Geosciences*, ed. by H. Aoki, Y. Syono, and R. J. Hemley, Cambridge University Press, Cambridge, England, 2000, chap. 6.1, pp. 325–339.

[73] P. C. Hemmer and G. Stell, *Physical Review Letters* **24**, 1284 (1970).

[74] B. Hess, C. Kutzner, D. van der Spoel, and E. Lindahl, *Journal of Chemical Theory and Computation* **4**, 435 (2008).

[75] D. Hohl and R. O. Jones, *Physical Review B* **50**, 17047 (1994).

[76] V. Holten, C. E. Bertrand, M. A. Anisimov, and J. V. Sengers, *Journal of Chemical Physics* **136**, 094507 (2012).

[77] V. Holten, J. Kalová, M. A. Anisimov, and J. V. Sengers, *International Journal of Thermophysics* **33**, 758 (2012).

[78] V. Holten, D. T. Limmer, V. Molinero, and M. A. Anisimov, *Journal of Chemical Physics* **138**, 174501 (2013).

[79] G. W. Hoover and F. H. Ree, *Journal of Chemical Physics* **49**, 3609 (1968).

[80] H. W. Horn, W. C. Swope, J. W. Pitera, J. D. Madura, T. J. Dick, G. L. Hura, and T. Head-Gordon, *Journal of Chemical Physics* **120**, 9665 (2004).

[81] C. W. Hsu, J. Largo, F. Sciortino, and F. W. Starr, *The Proceedings of the National Academy of Sciences of the United States of America* **105**, 13711 (2008).

[82] C. W. Hsu and F. W. Starr, *Physical Review E* **79**, 041502 (2009).

[83] C. Huang, T. M. Weiss, D. Nordlund, K. T. Wikfeldt, L. G. M. Pettersson, and A. Nilsson, *Journal of Chemical Physics* **133**, 134504 (2010).

[84] C. Huang, K. T. Wikfeldt, T. Tokushima, D. Nordlund, Y. Harada, U. Bergmann, M. Niebuhr, T. M. Weiss, Y. Horikawa, M. Leetmaa, M. P. Ljungberg, O. Takahashi, A. Lenz, L. Ojamäe, A. P. Lyubartsev, S. Shin, L. G. M. Pettersson, and A. Nilsson, *The Proceedings of the National Academy of Sciences of the United States of America* **106**, 15214 (2009).

[85] E. A. Jagla, *Physical Review E* **58**, 1478 (1998).

[86] E. A. Jagla, *Journal of Chemical Physics* **111**, 8980 (1999).

[87] E. A. Jagla, *Physical Review E* **63**, 061501 (2001).

[88] E. A. Jagla, *Physical Review E* **63**, 061509 (2001).

[89] V. Kapko, private communication, 2013.

[90] V. Kapko, Z. Zhao, D. V. Matyushov, and C. A. Angell, *Journal of Chemical Physics* **138**, 12A549 (2013).

[91] Y. Katayama, *Journal of Synchrotron Radiation* **8**, 182 (2001).

[92] Y. Katayama, *Journal of Non-Crystalline Solids* **312**, 8 (2002).

[93] Y. Katayama, Y. Inamura, T. Mizutani, M. Yamakata, W. Utsumi, and O. Shimomura, *Science* **306**, 848 (2004).

[94] Y. Katayama, T. Mizutani, W. Utsumi, O. Shimomura, M. Yamakata, and K.-I. Funakoshi, *Nature (London)* **403**, 170 (2000).

[95] N. Kern and D. Frenkel, *Journal of Chemical Physics* **118**, 9882 (2003).

[96] T. A. Kesselring, G. Franzese, S. V. Buldyrev, H. J. Herrmann, and H. E. Stanley, *Science Reports* **2**, 474 (2012).

[97] T. A. Kesselring, E. Lascaris, G. Franzese, S. V. Buldyrev, H. J. Herrmann, and H. E. Stanley, *Journal of Chemical Physics* **138**, 244506 (2013).

[98] P. Kumar, S. V. Buldyrev, F. Sciortino, E. Zaccarelli, and H. E. Stanley, *Physical Review E* **72**, 021501 (2005).

[99] P. Kumar, G. Franzese, S. V. Buldyrev, and H. E. Stanley, *Physical Review E* **73**, 041505 (2006).

[100] P. Kumar, G. Franzese, and H. E. Stanley, *Journal of Physics: Condensed Matter* **20**, 244114 (2008).

[101] P. Kumar, G. Franzese, and H. E. Stanley, *Physical Review Letters* **100**, 105701 (2008).

[102] P. Kumar and H. E. Stanley, *Journal of Physical Chemistry B* **115**, 14269 (2011).

[103] R. Kurita and H. Tanaka, *Science* **306**, 845 (2004).

[104] R. Kurita and H. Tanaka, *Journal of Physics: Condensed Matter* **17**, L293 (2005).

[105] E. Lascaris, M. Hemmati, S. V. Buldyrev, H. E. Stanley, and C. A. Angell, *Journal of Chemical Physics* **140**, 224502 (2014).

[106] E. Lascaris, T. A. Kesselring, G. Franzese, S. V. Buldyrev, H. J. Herrmann, and H. E. Stanley, "Response Functions near the Liquid-Liquid Critical Point of ST2 Water", in: *4th International Symposium on Slow Dynamics in Complex Systems*, ed. by M. Tokuyama and I. Oppenheimer, vol. 1518, AIP Conf. Proc., Dec. 2013, pp. 520–526.

[107] E. Lascaris, G. Malescio, S. V. Buldyrev, and H. E. Stanley, *Physical Review E* **81**, 031201 (2010).

[108] C. N. Likos, *Physics Reports* **348**, 267 (2001).

[109] C. N. Likos, M. Watzlawek, and H. Löwen, *Physical Review E* **58**, 3135 (1998).

[110] D. T. Limmer and D. Chandler, *Journal of Chemical Physics* **135**, 134503 (2011).

[111] D. T. Limmer and D. Chandler, *Journal of Chemical Physics* **138**, 214504 (2013).

[112] Y. Liu, J. C. Palmer, A. Z. Panagiotopoulos, and P. G. Debenedetti, *Journal of Chemical Physics* **137**, 214505 (2012).

[113] Y. Liu, A. Z. Panagiotopoulos, and P. G. Debenedetti, *Journal of Chemical Physics* **131**, 104508 (2009).

[114] Y. Liu, A. Z. Panagiotopoulos, and P. G. Debenedetti, *Journal of Chemical Physics* **132**, 144107 (2010).

[115] T. Loerting and N. Giovambattista, *Journal of Physics: Condensed Matter* **18**, R919 (2006).

[116] P. A. Madden and M. Wilson, *Journal of Physics: Condensed Matter* **12**, A95 (2000).

[117] F. Mallamace, M. Broccio, C. Corsaro, A. Faraone, D. Majolino, V. Valentina, L. Liu, C.-Y. Mou, and S.-H. Chen, *The Proceedings of the National Academy of Sciences of the United States of America* **104**, 424 (2007).

[118] F. Mallamace, C. Corsaro, and H. E. Stanley, *Science Reports* **2**, 993 (2012).

[119] M. Matsumoto, S. Saito, and I. Ohmine, *Nature (London)* **416**, 409 (2002).

[120] M. G. Mazza, K. Stokely, S. E. Pagnotta, F. Bruni, H. E. Stanley, and G. Franzese, *The Proceedings of the National Academy of Sciences of the United States of America* **108**, 19873 (2011).

[121] M. G. Mazza, K. Stokely, H. E. Stanley, and G. Franzese, *Journal of Chemical Physics* **137**, 204502 (2012).

[122] M. G. Mazza, K. Stokely, E. G. Strekalova, H. E. Stanley, and G. Franzese, *Computer Physics Communications* **180**, 497 (2009).

[123] P. F. McMillan, *Journal of Materials Chemistry* **14**, 1506 (2004).

[124] P. F. McMillan, M. Wilson, D. Daisenberger, and D. Machon, *Nature Materials* **4**, 680 (2005).

[125] C. Meade, R. J. Hemley, and H. K. Mao, *Physical Review Letters* **69**, 1387 (1992).

[126] O. Mishima, *Journal of Chemical Physics* **100**, 5910 (1994).

[127] O. Mishima, L. D. Calvert, and E. Whalley, *Nature (London)* **310**, 393 (1984).

[128] O. Mishima, L. D. Calvert, and E. Whalley, *Nature (London)* **314**, 76 (1985).

[129] O. Mishima and H. E. Stanley, *Nature (London)* **392**, 164 (1998).

[130] O. Mishima and H. E. Stanley, *Nature (London)* **396**, 329 (1998).

[131] V. Molinero and E. B. Moore, *Journal of Physical Chemistry B* **113**, 4008 (2009).

[132] V. Molinero, S. Sastry, and C. A. Angell, *Physical Review Letters* **97**, 075701 (2006).

[133] M. Morishita, A. Navrotsky, and M. C. Wilding, *Journal of the American Ceramic Society* **87**, 1550 (2004).

[134] T. Morishita, *Physical Review Letters* **93**, 055503 (2004).

[135] P. A. Netz, S. V. Buldyrev, M. C. Barbosa, and H. E. Stanley, *Physical Review E* **73**, 061504 (2006).

[136] A. Nilsson, private communication, 2012.

[137] A. Nilsson and L. G. M. Pettersson, *Chemical Physics* **389**, 1 (2011).

[138] S. Nosé, *Journal of Chemical Physics* **81**, 511 (1984).

[139] S. Nosé, *Progress of Theoretical Physics Supplement* **103**, 1 (1991).

[140] D. S. Olander and S. A. Rice, *The Proceedings of the National Academy of Sciences of the United States of America* **69**, 98 (1972).

[141] A. B. de Oliveira, G. Franzese, P. A. Netz, and M. C. Barbosa, *Journal of Chemical Physics* **128**, 064901 (2008).

[142] A. B. de Oliveira, P. A. Netz, and M. C. Barbosa, *EPL (Europhysics Letters)* **85**, 36001 (2009).

[143] D. Paschek, *Physical Review Letters* **94**, 217802 (2005).

[144] D. Paschek, A. Rüppert, and A. Geiger, *ChemPhysChem* **9**, 2737 (2008).

[145] A. Penny, E. Lozowski, T. Forest, C. Fong, S. Maw, P. Montgomery, and N. Sinha, "Speedskate ice friction: review and numerical model - FAST 1.0", in: *Proceedings of the 11th International Conference on the Physics and Chemistry of Ice*, ed. by W. F. Kuhs, vol. 311, Royal Society of Chemistry, 1997, pp. 248–256.

[146] O. Pfaffenzeller and D. Hohl, *Journal of Physics: Condensed Matter* **9**, 11023 (1997).

[147] A. Pietropaolo, R. Senesi, C. Andreani, A. Botti, M. A. Ricci, and F. Bruni, *Physical Review Letters* **100**, 127802 (2008).

[148] P. H. Poole, S. R. Becker, F. Sciortino, and F. W. Starr, *Journal of Physical Chemistry B* **115**, 14176 (2011).

[149] P. H. Poole, R. K. Bowles, I. Saika-Voivod, and F. Sciortino, *Journal of Chemical Physics* **138**, 034505 (2013).

[150] P. H. Poole, M. Hemmati, and C. A. Angell, *Physical Review Letters* **79**, 2281 (1997).

[151] P. H. Poole, I. Saika-Voivod, and F. Sciortino, *Journal of Physics: Condensed Matter* **17**, L431 (2005).

[152] P. H. Poole, F. Sciortino, U. Essmann, and H. E. Stanley, *Nature (London)* **360**, 324 (1992).

[153] E. Rapaport, *Journal of Chemical Physics* **48**, 1433 (1968).

[154] A. Reinhardt and J. P. K. Doye, *Journal of Chemical Physics* **136**, 054501 (2012).

[155] F. Romano, E. Sanz, and F. Sciortino, *Journal of Chemical Physics* **134**, 174502 (2011).

[156] J.-P. Ryckaert, G. Ciccotti, and H. J. C. Berendsen, *Journal of Computational Physics* **23**, 327 (1977).

[157] M. R. Sadr-Lahijany, A. Scala, S. V. Buldyrev, and H. E. Stanley, *Physical Review Letters* **81**, 4895 (1998).

[158] M. R. Sadr-Lahijany, A. Scala, S. V. Buldyrev, and H. E. Stanley, *Physical Review E* **60**, 6714 (1999).

[159] I. Saika-Voivod, P. H. Poole, and F. Sciortino, *Nature (London)* **412**, 514 (2001).

[160] I. Saika-Voivod, F. Sciortino, and P. H. Poole, *Physical Review E* **63**, 011202 (2000).

[161] I. Saika-Voivod, F. Smallenburg, and F. Sciortino, *Journal of Chemical Physics* **139**, 234901 (2013).

[162] A. M. Saitta and F. Datchi, *Physical Review E* **67**, 020201(R) (2003).

[163] F. de los Santos and G. Franzese, *Journal of Physical Chemistry B* **115**, 14311 (2011).

[164] F. de los Santos and G. Franzese, *Physical Review E* **85**, 010602 (2012).

[165] S. Sastry, *Nature (London)* **409**, 164 (2001).

[166] S. Sastry and C. A. Angell, *Nature Materials* **2**, 739 (2003).

[167] S. Sastry, P. G. Debenedetti, F. Sciortino, and H. E. Stanley, *Physical Review E* **53**, 6144 (1996).

[168] S. Scandolo, *The Proceedings of the National Academy of Sciences of the United States of America* **100**, 3051 (2003).

[169] P. Scheidler, W. Kob, A. Latz, J. Horbach, and K. Binder, *Physical Review B* **63**, 104204 (2001).

[170] E. Schwegler, G. Galli, and F. Gygi, *Physical Review Letters* **84**, 2429 (2000).

[171] F. Sciortino, *Journal of Physics: Condensed Matter* **17**, V7 (2005).

[172] F. Sciortino, P. H. Poole, H. E. Stanley, and S. Havlin, *Physical Review Letters* **64**, 1686 (1990).

[173] F. Sciortino, I. Saika-Voivod, and P. H. Poole, *Physical Chemistry Chemical Physics* **13**, 19759 (2011).

[174] J. Senker and E. Rössler, *Chemical Geology* **174**, 143 (2001).

[175] A. Sepúlveda, E. Leon-Gutierrez, M. Gonzalez-Silveira, C. Rodriguez-Tinoco, M. T. Clavaguera-Mora, and J. Rodriguez-Viejo, *Journal of Chemical Physics* **137**, 244506 (2012).

[176] K. A. Sharp and J. M. Vanderkooi, *Accounts of Chemical Research* **43**, 231 (2010).

[177] H. W. Sheng, H. Z. Liu, Y. Q. Cheng, J. Wen, P. L. Lee, W. K. Luo, S. D. Shastri, and E. Ma, *Nature Materials* **6**, 192 (2007).

[178] F. Smallenburg and F. Sciortino, *Nature Physics* **9**, 554 (2013).

[179] A. K. Soper, *Chemical Physics* **258**, 121 (2000).

[180] A. K. Soper and M. A. Ricci, *Physical Review Letters* **84**, 2881 (2000).

[181] R. J. Speedy, *Journal of Physical Chemistry* **86**, 3002 (1982).

[182] R. J. Speedy, *Journal of Physical Chemistry* **86**, 982 (1982).

[183] R. J. Speedy and C. A. Angell, *Journal of Chemical Physics* **65**, 851 (1976).

[184] H. E. Stanley, P. Kumar, G. Franzese, L. Xu, Z. Yan, M. G. Mazza, S. V. Buldyrev, S.-H. Chen, and F. Mallamace, *European Physical Journal Special Topics* **161**, 1 (2008).

[185] H. E. Stanley, S. V. Buldyrev, G. Franzese, P. Kumar, F. Mallamace, M. G. Mazza, K. Stokely, and L. Xu, *Journal of Physics: Condensed Matter* **22**, 284101 (2010).

[186] H. E. Stanley, S. V. Buldyrev, P. Kumar, F. Mallamace, M. G. Mazza, K. Stokely, L. Xu, and G. Franzese, *Journal of Non-Crystalline Solids* **357**, 629 (2011).

[187] H. E. Stanley, P. Kumar, S. Han, M. G. Mazza, K. Stokely, S. V. Buldyrev, G. Franzese, F. Mallamace, and L. Xu, *Journal of Physics: Condensed Matter* **21**, 504105 (2009).

[188] F. W. Starr, J. K. Nielsen, and H. E. Stanley, *Physical Review Letters* **82**, 2294 (1999).

[189] F. W. Starr and F. Sciortino, *Journal of Physics: Condensed Matter* **18**, L347 (2006).

[190] F. W. Starr, F. Sciortino, and H. E. Stanley, *Physical Review E* **60**, 6757 (1999).

[191] P. J. Steinhardt, D. R. Nelson, and M. Ronchetti, *Physical Review B* **28**, 784 (1983).

[192] O. Steinhauser, *Molecular Physics* **45**, 335 (1982).

[193] G. Stell and P. C. Hemmer, *Journal of Chemical Physics* **56**, 4274 (1972).

[194] F. H. Stillinger and A. Rahman, *Journal of Chemical Physics* **60**, 1545 (1974).

[195] F. H. Stillinger and D. K. Stillinger, *Physica A* **244**, 358 (1997).

[196] F. H. Stillinger and T. A. Weber, *Physical Review B* **31**, 5262 (1985).

[197] K. Stokely, M. G. Mazza, H. E. Stanley, and G. Franzese, *The Proceedings of the National Academy of Sciences of the United States of America* **107**, 1301 (2010).

[198] T. Strässle, A. M. Saitta, Y. le Godec, G. Hamel, S. Klotz, J. S. Loveday, and R. J. Nelmes, *Physical Review Letters* **96**, 067801 (2006).

[199] E. G. Strekalova, D. Corradini, M. G. Mazza, S. V. Buldyrev, P. Gallo, G. Franzese, and H. E. Stanley, *Journal of Biological Physics* **38**, 97 (2012).

[200] E. G. Strekalova, J. Luo, H. E. Stanley, G. Franzese, and S. V. Buldyrev, *Physical Review Letters* **109**, 105701 (2012).

[201] E. G. Strekalova, M. G. Mazza, H. E. Stanley, and G. Franzese, *Physical Review Letters* **106**, 145701 (2011).

[202] E. G. Strekalova, M. G. Mazza, H. E. Stanley, and G. Franzese, *Journal of Physics: Condensed Matter* **24**, 064111 (2012).

[203] H. Tanaka, R. Kurita, and H. Mataki, *Physical Review Letters* **92**, 025701 (2004).

[204] *The physics hypertextbook*, http://physics.info/.

[205] T. Tokushima, Y. Harada, O. Takahashi, Y. Senba, H. Ohashi, L. G. M. Pettersson, A. Nilsson, and S. Shin, *Chemical Physics Letters* **460**, 387 (2008).

[206] J. S. Tse and D. D. Klug, *Physical Review B* **59**, 34 (1999).

[207] Y. Tu, S. V. Buldyrev, Z. Liu, H. Fang, and H. E. Stanley, *EPL (Europhysics Letters)* **97**, 56005 (2012).

[208] V. V. Vasisht, S. Saw, and S. Sastry, *Nature Physics* **7**, 549 (2011).

[209] E. Velasco, L. Mederos, G. Navascues, P. C. Hemmer, and G. Stell, *Physical Review Letters* **85**, 122 (2000).

[210] P. Vilaseca and G. Franzese, *Journal of Chemical Physics* **133**, 084507 (2010).

[211] P. Vilaseca and G. Franzese, *Journal of Non-Crystalline Solids* **357**, 419 (2011).

[212] K. Vollmayr, W. Kob, and K. Binder, *Physical Review B* **54**, 15808 (1996).

[213] *Water Structure and Science*, http://www.lsbu.ac.uk/water/, maintained by Martin Chaplin (London South Bank University).

[214] K. T. Wikfeldt, A. Nilsson, and L. G. M. Pettersson, *Physical Chemistry Chemical Physics* **13**, 19918 (2011).

[215] M. C. Wilding, M. Wilson, and P. F. McMillan, *Chemical Society Reviews* **35**, 964 (2006).

[216] N. B. Wilding and J. E. Magee, *Physical Review E* **66**, 031509 (2002).

[217] M. Wilson and P. F. McMillan, *Physical Review B* **69**, 054206 (2004).

[218] L. V. Woodcock, C. A. Angell, and P. Cheeseman, *Journal of Chemical Physics* **65**, 1565 (1976).

[219] L. Xu, S. V. Buldyrev, C. A. Angell, and H. E. Stanley, *Physical Review E* **74**, 031108 (2006).

[220] L. Xu, S. V. Buldyrev, N. Giovambattista, C. A. Angell, and H. E. Stanley, *Journal of Chemical Physics* **130**, 054505 (2009).

[221] L. Xu, N. Giovambattista, S. V. Buldyrev, P. G. Debenedetti, and H. E. Stanley, *Journal of Chemical Physics* **134**, 064507 (2011).

[222] L. Xu, P. Kumar, S. V. Buldyrev, S.-H. Chen, P. H. Poole, F. Sciortino, and H. E. Stanley, *The Proceedings of the National Academy of Sciences of the United States of America* **102**, 16558 (2005).

[223] L. Xu, F. Mallamace, Z. Yan, F. W. Starr, S. V. Buldyrev, and H. E. Stanley, *Nature Physics* **5**, 565 (2009).

[224] M. Yamada, S. Mossa, H. E. Stanley, and F. Sciortino, *Physical Review Letters* **88**, 195701 (2002).

[225] Z. Yan, S. V. Buldyrev, N. Giovambattista, P. G. Debenedetti, and H. E. Stanley, *Physical Review E* **73**, 051204 (2006).

[226] Z. Yan, S. V. Buldyrev, N. Giovambattista, and H. E. Stanley, *Physical Review Letters* **95**, 130604 (2005).

[227] Z. Yan, S. V. Buldyrev, P. Kumar, N. Giovambattista, P. G. Debenedetti, and H. E. Stanley, *Physical Review E* **76**, 051201 (2007).

[228] Z. Yan, S. V. Buldyrev, P. Kumar, N. Giovambattista, and H. E. Stanley, *Physical Review E* **77**, 042201 (2008).

[229] D. A. Young and B. J. Alder, *Physical Review Letters* **38**, 1213 (1977).

[230] Y. Zhang, A. Faraone, W. A. Kamitakahara, K.-H. Liu, C.-Y. Mou, J. B. Leão, S. Chang, and S.-H. Chen, *The Proceedings of the National Academy of Sciences of the United States of America* **108**, 12206 (2011).

CURRICULUM VITAE

ERIK LASCARIS

CONTACT

Department of Physics, Boston University — Office: 617-353-3891

590 Commonwealth Avenue — Fax: 617-353-9393

Boston, MA 02215, USA — E-mail: erikl@bu.edu

EDUCATION

- 2014, Ph.D. in Physics, Boston University, Boston, MA 02215, USA

  Advisor: H. Eugene Stanley

  Thesis: *Liquid-liquid phase transitions and water-like anomalies in liquids*

- 2006, M.A. in Applied Physics (*Cum Laude*), Twente University, Enschede, The Netherlands

  Advisor: Eric Laenen

  Thesis: *The influence of several Standard Model extensions on the production of single top quarks in hadron collisions*

LIST OF PUBLICATIONS

- E. Lascaris, M. Hemmati, S. V. Buldyrev, H. E. Stanley, and C. A. Angell, *Search for a liquid-liquid critical point in models of silica*, J. of Chem. Phys. **140**, 224502 (2014)

- J. Luo, L. Xu, E. Lascaris, H. E. Stanley, and S. V. Buldyrev, *Behavior of the Widom Line in Critical Phenomena*, Phys. Rev. Lett. **112**, 135701 (2014)

- T. A. Kesselring, E. Lascaris, G. Franzese, S. V. Buldyrev, H. J. Herrmann, and H. E. Stanley, *Finite-size scaling investigation of the liquid-liquid critical point in ST2 water and its stability with respect to crystallization*, J. of Chem. Phys. **138**, 244506 (2013)

- E. Lascaris, T. A. Kesselring, G. Franzese, S. V. Buldyrev, H. J. Herrmann, and H. E. Stanley, *Response functions near the liquid-liquid critical point of ST2 Water*, in Slow Dynamics in Complex Systems, edited by M. Tokuyama, AIP Conference Proceedings **1518**, 520–526 (2013)

- E. Lascaris, G. Malescio, S. V. Buldyrev, and H. E. Stanley, *Cluster formation, waterlike anomalies, and re-entrant melting for a family of bounded repulsive interaction potentials*, Phys. Rev. E **81**, 031201 (2010)

RESEARCH EXPERIENCE

- 2010 – Present: System administrator at the Center for Polymer Studies, Boston University, Boston MA, USA

- Dec. 2008 – Sep. 2014: Research assistant studying liquid water and its anomalies at Boston University, Boston MA, USA

- Sep. 2005 – Aug. 2006: Intership at National Institute for Nuclear Physics and High Energy Physics (NIKHEF), Amsterdam, The Netherlands

TEACHING EXPERIENCE

- Jan. 2009 – Present: Navy ROTC physics/math tutor, Boston University, Boston MA, USA. Unit representing Boston University, Boston College, and Northeastern University

- Sep. 2006 – Dec. 2008: Teaching Fellow at Boston University, Boston MA, USA. Teaching several courses, including General Physics I, General Physics II, and Quantum Mechanics I

TALKS

- Jun. 2013: *Phase flipping and crystallization in the ST2 water model*, CMCSN water meeting at UC Davis
- Mar. 2012: *Time fluctuations in density and dielectric constant of low and high density water*, American Physical Society (APS) March meeting at Boston MA
- Jan. 2012: *Phase flipping in ST2 water near its hypothesized liquid-liquid critical point*, Mini Stat Mech meeting at UC Berkeley

HONORS AND AWARDS

- 2010: Chair's Book award for excellence in teaching (Boston University)
- 2004: CERN summer student (CERN)